A Study of Charm Quark Production in Beauty Quark Decays with the OPAL Detector at LEP

by

David Waller B.Sc., M.Sc.

A thesis submitted to the
Faculty of Graduate Studies and Research
in partial fulfillment of the requirements
for the degree of
Doctor of Philosophy

Ottawa-Carleton Institute for Physics
Department of Physics, Carleton University
Ottawa, Ontario, Canada
January, 2003

©copyright
2003, David Waller

National Library of Canada
Acquisitions and Bibliographic Services
395 Wellington Street
Ottawa ON K1A 0N4
Canada

Bibliothèque nationale du Canada
Acquisitions et services bibliographiques
395, rue Wellington
Ottawa ON K1A 0N4
Canada

Your file Votre référence

Our file Notre référence

The author has granted a non-exclusive licence allowing the National Library of Canada to reproduce, loan, distribute or sell copies of this thesis in microform, paper or electronic formats.

The author retains ownership of the copyright in this thesis. Neither the thesis nor substantial extracts from it may be printed or otherwise reproduced without the author's permission.

L'auteur a accordé une licence non exclusive permettant à la Bibliothèque nationale du Canada de reproduire, prêter, distribuer ou vendre des copies de cette thèse sous la forme de microfiche/film, de reproduction sur papier ou sur format électronique.

L'auteur conserve la propriété du droit d'auteur qui protège cette thèse. Ni la thèse ni des extraits substantiels de celle-ci ne doivent être imprimés ou autrement reproduits sans son autorisation.

0-612-79467-9

Canada

The undersigned hereby recommend to
the Faculty of Graduate Studies and Research
acceptance of the thesis,

A Study of Charm Quark Production in Beauty Quark Decays with the OPAL detector at LEP

submitted by
David Waller, B.Sc., M.Sc.

in partial fulfilment of the requirements
for the degree of Doctor of Philosophy

Pat Kalyniak
Chair, Department of Physics

Thesis Supervisor

W Trischuk
External Examiner

Carleton University

Date: January 20, 2003

Abstract

The production of charm quarks in beauty quark decays has been studied with the OPAL detector at the Large Electron Positron collider near Geneva, Switzerland. The branching ratio Br(b $\rightarrow$ D$\bar{\text{D}}$X) has been measured using hadronic Z^0 decays collected between 1993 and 1995. Here b refers to the admixture of weakly decaying hadrons containing a b quark that are produced in electron-positron annihilations at a centre of mass energy equal to the mass of the Z^0 boson. The impact parameter significance of tracks in tagged b-jets is used to differentiate b $\rightarrow$ D$\bar{\text{D}}$X decays from other decays. The result is

$$\text{Br}(\text{b} \rightarrow \text{D}\bar{\text{D}}\text{X}) = (10.0 \pm 3.2(stat.)^{+2.4}_{-2.9}(syst.\ det.)^{+10.4}_{-9.0}(syst.\ phys.))\%.$$

where *syst. det.* is the systematic uncertainty due to the modelling of the detector, and *syst. phys.* is the systematic uncertainty due to the modelling of the underlying particle physics. Using this result, the average number of charm and anti-charm quarks produced in a beauty quark decay, n_c, is found to be $1.12^{+0.11}_{-0.10}$.

Acknowledgments

High energy physics experiments are BIG science and big science requires hundreds (if not thousands) of people to work together. Without the superb work of countless physicists, engineers, and technicians, LEP, OPAL and this thesis would never have been possible. My hat is off to all the people at CERN and around the world who contributed to building and operating the fantastic machines and detector that produced the data studied in this thesis.

Thanks to the generous financial support of the Carleton-OPAL group, I was very fortunate to have the opportunity to spend time at CERN, learning about and working at OPAL. It was a privilege to do physics with and learn from the best in the world.

Thank you to my supervisor, Dean Karlen, for guiding me in my research. I could not have had a better teacher to help me learn how to do a physics analysis and how to think critically. His role in my physics education has been paramount.

The rest of the OPAL faculty at Carleton (Bob Carnegie, Richard Hemingway, Gerald Oakham, Penny Estabrooks, Hans Mes, Alain Bellerive, Madhu Dixit) also were great during my time here as a graduate student. Their doors were always open and they were always enthusiastic about talking physics (or anything else!) when I came knocking. A special thanks goes to Richard Hemingway for his unbridled enthusiasm whenever I visited his office to chat.

Thanks to Mike Donkers for being such a good office neighbour, friend and colleague during these past many years. I am forever grateful for his answering all my LaTeX, PAW, UNIX, FORTRAN, and ROPE questions. Carleton post-docs John White and Tom Junk deserve much credit for their help. John and I started working on this analysis together, and he and his wife, Maicci, were superior guides to life at CERN. Tom's expertise in tracking and b physics was extremely helpful for this analysis. Richard Hawkings and Pauline Gagnon were also great at answering all

my b physics emails and convening OPAL's Heavy Flavour working group. I am also grateful for the fine job that the computing staffs at Carleton and CERN have done in providing stable systems on which this analysis was performed.

All the above people and many more who I did not have space to name, have made working on OPAL (at Carleton and at CERN) a truly memorable experience.

I would also like to thank my parents for encouraging my physics endeavours. They fostered my love of learning and taught me to pursue my dreams. Completing this thesis in the fantastic field of particle physics was definitely one of those.

Last, but certainly not least, my deepest gratitude to my wife, Pam, for her support, love and encouragement, day in and day out. In Ottawa, Ornex and Gex, she was with me every step of the way. Thank you.

Contents

Abstract iii

Acknowledgments iv

1 Introduction 1

2 The Standard Model and Heavy Quark Physics 4

2.1 Standard Model 4

2.1.1 Constituents of matter 4

2.1.2 Fundamental Interactions 6

2.2 Heavy quark physics 17

2.2.1 Production and detection of heavy quarks 17

2.2.2 Heavy Quark Effective Theory 19

2.2.3 Charm counting and Br(b $\rightarrow$ D$\bar{\text{D}}$X) 21

3 The LEP Collider and the OPAL Detector 25

3.1 The LEP Collider 25

3.1.1 Production of e^+ and e^- 26

3.1.2 Acceleration of e^+ and e^- 26

3.1.3 Collision of e^+ and e^- 29

3.2 The OPAL Detector 31

3.2.1 Charged particle tracking system 33

3.2.2 Magnet 41

3.2.3 Time of flight detectors 41

3.2.4 Electromagnetic calorimetry 42

3.2.5 Hadronic calorimetry 44

3.2.6 Muon detectors 45

3.2.7 Forward detectors 46
3.2.8 Trigger, data acquisition and data recording 46

4 Data Samples and Monte Carlo Simulation 50
4.1 Data collected by OPAL 50
4.2 Simulated data 51
4.2.1 Simulation of hadronic Z^0 decays 53

5 Analysis Method 57
5.1 Joint probability 57
5.2 S resolution function determination 61
5.3 Tuning of d_0 and σ_{d_0} 66
5.4 Fitting procedure 76
5.4.1 Potential bias in fit 83
5.5 Event, jet and track selection 86
5.5.1 Event selection 86
5.5.2 Jet selection 89
5.5.3 Track selection 91

6 Results 94
6.1 Results for each year 94
6.2 Cross check: analysis with simulated "pseudo-data" 95
6.3 Combination of $Br(b \rightarrow D\bar{D}X)$ results 103
6.4 n_c result 104

7 Systematic Uncertainties 105
7.1 Determination of systematic uncertainties 105
7.2 Statistical uncertainty in estimates of systematic uncertainty 108
7.3 Detector modelling 110
7.3.1 d_0 modelling 110
7.3.2 σ_{d_0} modelling 111
7.3.3 Track selection efficiency 111
7.3.4 Combination of detector systematic uncertainties 113
7.4 Particle physics modelling 113
7.4.1 b quark fragmentation 113

7.4.2 Multiplicity of charged particles from fragmentation 115
7.4.3 Momentum spectrum of D hadrons in b hadron decays 116
7.4.4 Charm and beauty hadron lifetimes 118
7.4.5 Fractions of b hadron species 118
7.4.6 Gluon splitting to $b\bar{b}$ or $c\bar{c}$ pairs 119
7.4.7 Charged particle multiplicity of D decays 119
7.4.8 Neutral pion multiplicity of D decays 120
7.4.9 Neutral kaon production in D decays 121
7.4.10 Charged particle multiplicity of b decays 121
7.4.11 Fractions of D hadrons in single and double charm b decays . 122
7.4.12 Background fractions 124

8 Discussion **126**
8.1 Comparison to previous measurements 126
8.2 Uncertainty due to $< N_{ch} >_{frag}$ 127

9 Conclusions **129**
9.1 Br(b $\rightarrow$ D$\bar{\text{D}}$X) Measurement 129
9.2 n_c Measurement 129
9.3 Comparison to theory 130
9.4 Future prospects 131

A OPAL coordinate system and track parameters **134**

Bibliography **146**

List of Figures

2.1 Weak neutral current vertex. 10
2.2 Weak charged current interaction 12
2.3 Hadronic cross-section for electron-positron annihilation near the Z^0 resonance. 15
2.4 Strong interaction vertex: quark coupling to a gluon 16
2.5 Feynman diagrams of weak decays of b hadrons. 20

3.1 Schematic view of the accelerator complex at CERN. 27
3.2 Schematic view of the OPAL detector. 32
3.3 Picture of the OPAL silicon vertex detector. 36
3.4 Particle identification using dE/dx and momentum. 40
3.5 Reconstruction of hadronic Z^0 decay in OPAL 49

4.1 Simulation of hadronic Z^0 decay by JETSET 54

5.1 Three different topologies of B decays 58
5.2 Calculation of track p_i 60
5.3 S distributions from Monte Carlo for SI-$r\phi$=SI-z=2 tracks originating at decay points of b and daughter D hadrons 65
5.4 Comparison of $|d_0|$ and σ_{d_0} distributions of SI-$r\phi$=SI-z=2 backward tracks for 1994 *default* MC and data 67
5.5 Comparison of $|d_0|$ and σ_{d_0} distributions of SI-$r\phi$=SI-z=2 backward tracks for *tuned* MC and data 68
5.6 Pull distributions and data/MC ratios for $|d_0|$ of backward tracks (default MC) 69
5.7 Pull distributions and data/MC ratios for $|d_0|$ of backward tracks (tuned MC) 70

5.8 Pull distributions and data/MC ratios for σ_{d_0} of backward tracks (default MC) . . . 73
5.9 Pull distributions and data/MC ratios for σ_{d_0} of backward tracks (tuned MC) . . . 74
5.10 Impact parameter significance distributions for SI-$r\phi$=SI-z=2 backward tracks . . . 75
5.11 Signal (b hadron decay) $-\ln(P_j)$ distributions from 1994 MC . . . 77
5.12 Background (no b hadron decay) $-\ln(P_j)$ distributions from 1994 MC 78
5.13 Comparison of $-\ln(P_j)$ distributions with different mean charged particle multiplicities from fragmentation . . . 80
5.14 $|\cos(\theta_T)|$ and thrust distributions of events in the data . . . 87
5.15 b-tagging variable for jets initiated by different flavour quarks in simulated and data hadronic Z^0 decays . . . 90
5.16 Track cuts used for analysis . . . 92

6.1 Fits of MC PDFs to data for 1993 for each track multiplicity bin . . . 96
6.2 Residuals for fits of MC $-\ln(P_j)$ PDFs to 1993 data. . . . 97
6.3 Fits of MC PDFs to data for 1994 for each track multiplicity . . . 98
6.4 Residuals for fits of MC $-\ln(P_j)$ PDFs to 1994 data. . . . 99
6.5 Fits of MC PDFs to data for 1995 for each track multiplicity . . . 100
6.6 Residuals for fits of MC $-\ln(P_j)$ PDFs to 1995 data. . . . 101
6.7 Combined result for Br(b $\rightarrow$ D$\bar{\text{D}}$X) . . . 103

7.1 Visualization of statistical noise in systematic error estimates . . . 109
7.2 The most recent CLEO $< x_{\text{b}\rightarrow\text{D}} >$ data fitted by both a gaussian and a Peterson fragmentation function . . . 117

9.1 Comparison of measured n_c and Br(b $\rightarrow \ell\nu$X) to theory . . . 132

A.1 The OPAL coordinate system. . . . 135
A.2 Definition of track parameters in OPAL. . . . 136

List of Tables

2.1 Matter particles in the Standard Model 7
2.2 Force carrying particles in the Standard Model 8
2.3 Weak neutral current coupling coefficients, c_V^f and c_A^f 11

4.1 Year-by-year breakdown of hadronic events in the data and the MC . 51

5.1 S resolution function characteristics 62
5.2 Fraction of non-fragmentation backward tracks passing track selection cuts with and without anti-heavy flavour tag on opposite jet 63
5.3 Cuts for "quality" tracks 64
5.4 Best d_0 and σ_{d_0} scale factors for single SI-$r\phi$=SI-z=2 backwards tracks over wide range of d_0 and σ_{d_0} 71
5.5 Details of $-\ln(P_j)$ binning for fits 82
5.6 Origin of tracks passing track selection cuts 91

6.1 Results of $-\ln(P_j)$ fits for each year of data-taking 95

7.1 Summary of systematic errors for Br(b $\rightarrow$ D$\bar{\text{D}}$X) for 1994 (part 1) . . 106
7.2 Summary of systematic errors for Br(b $\rightarrow$ D$\bar{\text{D}}$X) for 1994 (part 2) . . 107
7.3 Fractions of tracks passing selection cuts (excluding silicon vertex detector hit requirement) that have two SI-$r\phi$ and two SI-z hits . . . 112
7.4 Values and uncertainties for f_{D_i} 124

Chapter 1

Introduction

The concept of quarks was hypothesized independently by George Zweig [1, 2] and Murray Gell-Mann [3] in 1964. The belief in quarks as real, physical particles did not become widespread until some years later however. Indeed, even Gell-Mann was reluctant to refer to them as physical particles for several years; it seems that Gell-Mann thought of quarks as a mathematical bookkeeping device for understanding the properties of many subatomic particles [4]. Genuine acceptance of the reality of quarks did not occur until the early 1970's, after electron-proton scattering experiments at the Stanford Linear Accelerator Centre (SLAC) [5, 6] indicated that protons were composed of more fundamental particles: quarks. Zweig's and Gell-Mann's original ideas about quarks proposed three types (or flavours) of quarks that are now called "up", "down" and "strange". These three quarks were sufficient to explain the properties of most of the subatomic particles that had been discovered in the 1950's, 60's and early 70's.

It did not take long however, for the number of known quarks to increase. The J/ψ particle that was discovered in 1974 by experimental groups at SLAC [7] and Brookhaven National Laboratory [8] in New York was interpreted as being composed

of a charm quark and an anti-charm quark. Next, the Υ particle discovered at Fermilab [9] near Chicago in 1977 was believed to be composed of a beauty quark and an anti-beauty quark (beauty quarks are also called bottom quarks; this authour prefers the more attractive moniker). There was a long wait until the next quark was discovered, but in 1995, experimentalists at Fermilab discovered the sixth quark [10, 11]: top (or truth as it is sometimes referred to). No more quarks have been discovered to date and, for aesthetic reasons to be described in chapter 2, physicists believe that the top quark was the last quark left to be discovered.

Even if there are no new quarks to discover, there is still much work to do to understand how the known quarks behave. Quarks are notoriously difficult to study as they never appear in isolation. For reasons described in chapter 2, quarks are found only in composite objects called hadrons. Discerning the behaviour of quarks from the behaviour of hadrons is not always straightforward.

When hadrons containing beauty quarks decay, they almost always decay to hadrons containing charm quarks. This thesis studies the inclusive production of charmed hadrons in beauty hadron decays. In particular, the goal of this thesis is to measure how often a beauty hadron decays to two charmed hadrons: $\mathrm{Br}(\mathrm{b} \to \mathrm{D}\bar{\mathrm{D}}\mathrm{X})$. From this measurement, one can calculate the average number of charmed quarks produced in the decay of a beauty quark: n_c. Determining $\mathrm{Br}(\mathrm{b} \to \mathrm{D}\bar{\mathrm{D}}\mathrm{X})$ and n_c experimentally provides a test of our theoretical understanding of how heavy quarks and hadrons behave.

Chapter 2 of this thesis reviews the constituents of matter and the interactions between them, as described by the Standard Model of particle physics. Some details of the physics of beauty quarks are also discussed. Chapter 3 provides an overview of the particle accelerators and detector which produced the data used for this thesis. A description of the real and simulated data sets is given in chapter 4. The method

used to measure $Br(b \rightarrow D\bar{D}X)$ is outlined in chapter 5. Following that, the results of this analysis are presented in chapter 6. A detailed discussion of the systematic uncertainties of $Br(b \rightarrow D\bar{D}X)$ is provided in chapter 7, and in the final two chapters, a discussion about the results and the conclusions of this thesis are presented.

Chapter 2

The Standard Model and Heavy Quark Physics

2.1 Standard Model

The widely accepted and thoroughly tested model that has successfully described the physics of elementary particles for over 30 years is the Standard Model of particle physics (or Standard Model for short) [12–16]. This model describes the weak, electromagnetic and strong interactions between the known elementary particles[1]. A brief description of the Standard Model is given in the following two sections. Section 2.1.1 provides a summary of the elementary constituents of matter; section 2.1.2 describes the forces between these particles.

2.1.1 Constituents of matter

In the Standard Model, all the elementary constituents of matter are spin 1/2 particles. These fermions are divided into the leptons and the quarks. Quarks undergo

[1] In most particle physics interactions, gravity is too weak a force to be of interest.

strong interactions while leptons do not. As mentioned in the introductory chapter, quarks can exist only in composite particles: hadrons. The two types of hadrons are mesons (bound states of a quark and an anti-quark[2]) and baryons (bound states of three quarks, or three anti-quarks for anti-baryons). The quarks come in two types: "up-type" and "down-type". The up-type quarks (up, charm, top) have an electric charge that is $+2/3$ the charge of an electron (q_e), and the down-type quarks (down, strange, beauty) possess $-q_e/3$ electric charge. The quarks can be arranged into three doublets so that the two lightest types (or "flavours") of quarks, up (u) and down (d), are paired together; charm (c) and strange (s) are paired together; and, the two heaviest flavours, top (t) and beauty (b), are paired together.

$$\begin{pmatrix} u \\ d \end{pmatrix} \begin{pmatrix} c \\ s \end{pmatrix} \begin{pmatrix} t \\ b \end{pmatrix} \tag{2.1}$$

The leptons also can be divided into two types: electrically charged and neutral. From lightest to heaviest, the electrically charged leptons are the electron (e^-), the muon (μ^-), and the tau (τ^-). All the charged leptons behave the same way, except the heavier μ^- and τ^- are unstable and decay via the weak force. The electrically neutral leptons are the neutrinos, ν. The neutrinos experience the weak force only. Each neutrino belongs to a doublet with a corresponding charged lepton. The three

[2]An anti-quark is the anti-matter version of a quark. In the Standard Model, every matter particle has an anti-particle "twin" whose internal quantum numbers have signs that are opposite those of the particle. The process of changing a particle's internal quantum numbers to transform it into an anti-particle is called charge conjugation. In this thesis, discussions about any particle process apply also to the charge conjugated process, unless stated otherwise.

neutrinos are named after their charged partners in the doublets: ν_e, ν_μ, ν_τ.

$$\begin{pmatrix} e^- \\ \nu_e \end{pmatrix} \begin{pmatrix} \mu^- \\ \nu_\mu \end{pmatrix} \begin{pmatrix} \tau^- \\ \nu_\tau \end{pmatrix} \tag{2.2}$$

The Standard Model has the peculiar feature that the matter particles are divided into three "generations". The first generation includes the lightest lepton and quark doublets. The second and third generations include the "mid-weight" and heaviest lepton and quark doublets, respectively. The second and third generations are near copies of the first generation; the heavier masses and short lifetimes of the second and third generations differentiate them from the first generation. There is currently no experimental evidence for quarks or leptons beyond the third generation. The aesthetic appeal of an equal number of generations of leptons and quarks leads physicists to believe that there are no heavier leptons or quarks. If a fourth generation quark exists, its mass must be at least 199 GeV/c^2 [17]. If a fourth generation charged lepton exists, its mass must be at least 94 GeV/c^2 [18]. Measurements at LEP of the width of the Z^0 resonance show that there are only three generations of light neutrinos [19]. If a stable fourth generation neutrino exists, the neutrino mass must be at least 45.0 GeV/c^2 [20]. A brief summary of the properties of the matter particles in the Standard Model is given in table 2.1.

2.1.2 Fundamental Interactions

In the Standard Model, the description of the fundamental forces is provided by two separate theories: the electroweak theory of Glashow, Salam and Weinberg [12–14], and Quantum Chromodynamics (QCD) [15, 16]. The electroweak theory describes and unifies the electromagnetic and weak forces. QCD describes the strong force. In

particle	mass (GeV/c^2)	lifetime (s)	electric charge (q_e)
u	$\sim$0.003	∞	2/3
c	1.2$\pm$0.2	$\sim 3 \times 10^{-13}$	2/3
t	174.3$\pm$5.1	$\sim 5 \times 10^{-25}$	2/3
d	$\sim$0.007	∞	-1/3
s	$\sim$0.100	$\sim 9 \times 10^{-11}$	-1/3
b	4.25$\pm$0.25	$\sim 1.5 \times 10^{-12}$	-1/3
e^-	5.11×10^{-4}	∞	-1
μ^-	0.106	2.2×10^{-6}	-1
τ^-	1.777	2.9×10^{-13}	-1
ν_e	$< 3 \times 10^{-9}$	∞	0
ν_μ	$< 1.9 \times 10^{-4}$	∞	0
ν_τ	$< 1.82 \times 10^{-2}$	∞	0

Table 2.1: The quarks and leptons of the Standard Model. The "lifetimes" of the quarks refer to the typical lifetimes of weakly decaying hadrons in which the noted quark is the heaviest quark. The upper limits for neutrino masses are given at a 90% confidence level. Although non-zero neutrino masses have not been measured directly, recent evidence of atmospheric [21] and solar neutrino [22] flavour oscillations indicates that neutrinos possess some, albeit small, mass. All of the particle properties were obtained from reference [23].

both of these theories, the forces are mediated by particles that are vector (spin = 1) bosons. The electromagnetic interaction is mediated by the photon, γ; the weak interaction is mediated by the $W^{\pm}$ and Z^0 bosons; the strong force is mediated by the gluons, g. The photon and gluons are massless while the $W^{\pm}$ and Z^0 bosons are very massive (see table 2.2).

Force	mediating particle	mass (GeV/c^2)
electromagnetic	photon (γ)	0
weak	$W^{\pm}$, Z^0	80.4, 91.2
strong	gluons (g)	0

Table 2.2: The force mediating particles of the Standard Model.

Both electroweak theory and QCD are quantum field theories which obey the principle of local gauge invariance. A theory is said to be locally gauge invariant if the fields in the Lagrangian density, $\mathcal{L}$, that describes the interaction, can be locally transformed (change gauges) without changing $\mathcal{L}$. The changing of gauges is equivalent to multiplying the fields in the Lagrangian density by a matrix. In order to construct Lagrangian densities that are locally gauge invariant under specific transformations, the Lagrangian densities in QCD and the electroweak theory contain terms that represent vector bosons. These bosons are sometimes called vector *gauge* bosons because they are required in $\mathcal{L}$ to ensure local gauge invariance. Vector gauge bosons are responsible for the propagation of the forces in the Standard Model.

Both QCD and the electroweak theory are based on assumed symmetries of nature. The symmetry group describing the electroweak interaction is called $SU(2)_L \otimes U(1)$[3]. QCD is described by the colour SU(3) symmetry group. The elec-

[3]These symmetry groups, $SU(2)_L$ and U(1), are represented by matrices. S stands for *special* (matrix is traceless) and U stands for *unitary*. The numbers in the brackets refer to the dimensions of the matrices. The L subscript stands for *left* and refers to the fact that only left-handed fermions experience the weak interaction.

troweak and QCD Langrangian densities are invariant under local transformations by their respective symmetry groups. In QCD, local gauge invariance requires the existence of eight vector gauge bosons: the massless gluons.

In electroweak theory, local $SU(2)_L \otimes U(1)$ gauge invariance requires the existence of four vector gauge bosons. In the theory, these bosons are initially massless but the $W^{\pm}$ and Z^0 acquire masses due to spontaneous breaking of the electroweak symmetry by a process called the Higgs mechanism [24–27]. An important consequence of electroweak symmetry breaking is that an electrically neutral, massive scalar boson must exist: the Higgs boson. Fermions that interact with the Higgs field obtain non-zero masses. The Higgs boson has not been discovered yet, but experimental results from LEP show that its mass is at least 114.1 GeV/c^2 at 90% confidence level [28].

Weak interactions

In the Standard Model, there are two types of weak interactions: those mediated by the Z^0 and those mediated by the $W^{\pm}$. Interactions mediated by a Z^0 are called neutral current interactions and interactions mediated by a W^+ or W^- are called charged current interactions. Only left handed fermions and right handed anti-fermions[4] experience the weak force. The Feynman diagram shown in figure 2.1 depicts a Z^0 coupling to a left-handed fermion. The vertex factor for the coupling of a Z^0 to a fermion is

$$\frac{-ig_z}{2}\gamma^{\mu}(c_V^f - c_A^f\gamma^5), \tag{2.3}$$

[4]Left handed fermions have their spins anti-aligned with their momentum vectors; right handed anti-fermions have their spins aligned with their momentum vectors.

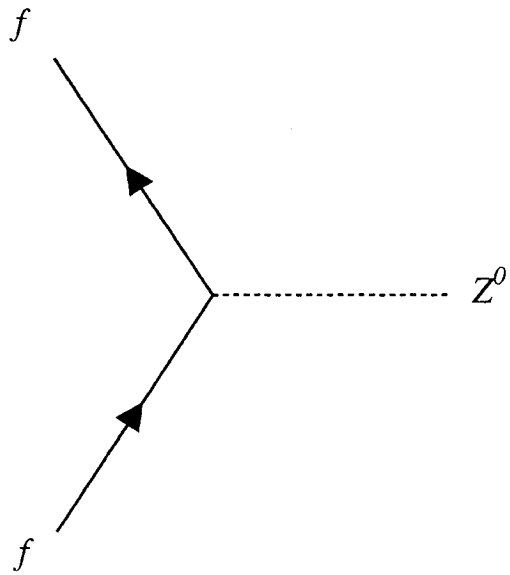

Figure 2.1: Weak neutral current vertex. The fermion flavour is conserved.

where γ^μ and γ^5 are matrices that give the interaction a vector (γ^μ) and axial-vector ($\gamma^\mu\gamma^5$) nature, c_V^f is the vector coupling coefficient, c_A^f is the axial-vector coupling coefficient, and g_z is the neutral weak coupling constant. The coupling coefficients are determined by the type of fermion to which the Z^0 couples (see table 2.3). The neutral weak coupling constant is related to the electromagnetic, g_e, and charged weak, g_w, coupling constants by

$$g_z = \frac{g_e}{\sin\theta_w \cos\theta_w} \quad , \quad g_z = \frac{g_w}{\cos\theta_w}, \tag{2.4}$$

fermion	c_V^f	c_A^f
u, c, t	1/2-(4/3)sin$^2\,\theta_W$	1/2
d, s, b	-1/2+(2/3) sin$^2\,\theta_W$	-1/2
e^-, μ^-, τ^-	-1/2+2sin$^2\,\theta_W$	-1/2
ν_e, ν_μ, ν_τ	1/2	1/2

Table 2.3: Weak neutral current coupling coefficients, c_V^f and c_A^f. The values of the coupling coefficients depend on the fermion, f, to which the Z^0 couples.

where θ_w is a parameter of the electroweak theory called the weak mixing angle. The charged weak coupling constant, g_w, is related to the Fermi weak coupling constant, G_F, by

$$G_F = \frac{\sqrt{2}}{8}\left(\frac{g_w}{M_W c^2}\right)^2 (\hbar c)^3, \tag{2.5}$$

where M_W is the mass of the $W^{\pm}$ boson. An important property of the neutral weak interaction is that it does not change the flavour of fermions.

In contrast to the neutral weak interaction, the charged weak interaction does change the flavour of fermions. Charged weak interactions change up-type quarks to down-type quarks (and vice versa), and charged leptons to neutrinos (and vice versa). Figure 2.2 shows the Feynman diagram for a charged weak interaction vertex. The vertex factor for the coupling of a $W^{\pm}$ to a fermion is similar to the vertex factor for a Z^0, but the coupling coefficients for the vector and axial-vector portions of the charged interaction are the same:

$$\frac{-ig_w}{2\sqrt{2}}\gamma^\mu(1-\gamma^5)V_{f_i f_f}. \tag{2.6}$$

The value of $V_{f_i f_f}$ depends on what kind of fermion, f_f, is produced after the original

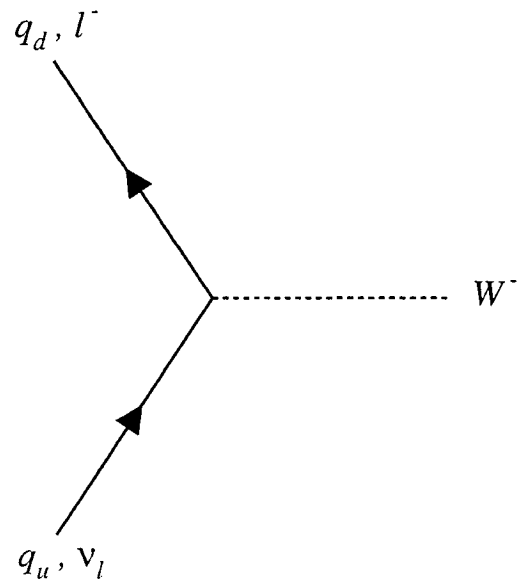

Figure 2.2: Weak charged current interaction of $W^{\pm}$ with a fermion. The interaction changes the flavour of the fermion.

fermion, f_i, interacts with the $W^{\pm}$. If f_i is a charged lepton, then f_f is the associated neutrino; so for leptons, $V_{l\nu_l} = V_{\nu_l l} = 1$ and $V_{l'\nu_l} = V_{\nu_l l'} = 0$. If f_i and f_f are quarks though, the picture is slightly more complicated.

As previously mentioned, the charged weak current changes up-type quarks to down-type quarks (and vice versa). As a result, there are nine different $V_{q_i q_f}$ ($V_{q_i q_f} = V_{q_f q_i}$). The 3×3 matrix that consists of the nine $V_{q_i q_f}$ is called the Cabibbo-Kobayashi-Maskawa (CKM) matrix [29,30]. This matrix parameterizes the relative probability for different quark flavour-changing processes in charged weak interac-

tions. Neglecting kinematic factors,

$$\frac{P(q \to q')}{P(q \to q'')} \propto \left(\frac{V_{qq'}}{V_{qq''}}\right)^2 . \tag{2.7}$$

Because any up-type quark can change into any down-type quark, one can re-write the quark doublets originally shown in equation 2.1 as

$$\begin{pmatrix} u \\ d' \end{pmatrix}_L \begin{pmatrix} c \\ s' \end{pmatrix}_L \begin{pmatrix} t \\ b' \end{pmatrix}_L , \tag{2.8}$$

where the charged weak interaction down-type quarks, d', s', b', are related to the physical quarks, d, s, b, by

$$\begin{pmatrix} d' \\ s' \\ b' \end{pmatrix} = \begin{pmatrix} V_{ud} & V_{us} & V_{ub} \\ V_{cd} & V_{cs} & V_{cb} \\ V_{td} & V_{ts} & V_{tb} \end{pmatrix} \begin{pmatrix} d \\ s \\ b \end{pmatrix} . \tag{2.9}$$

The "L" subscripts on the quark doublets in equation 2.8 denote the fact that only left-handed fermions participate in weak charged current interactions. So, the charged weak interaction transforms the up-type quark of each doublet in equation 2.8 to its "primed" down-type partner. In the same way, the charged weak interaction transforms the charged lepton of each lepton doublet (equation 2.2) to its neutrino partner in the doublet. Lepton flavour is conserved in charged weak interactions though; for example, an e^- can transform only to a ν_e in a charged weak interaction.

Both the neutral and charged weak interactions are of great importance to this thesis. The neutral weak interaction is important because the centre of mass energy of the e^+e^- annihilations at LEP was equal to the mass of the particle responsible

for the neutral weak interaction, the Z^0 boson. As a result, the cross section for e^+e^- annihilation at LEP was very large. Figure 2.3 shows the cross-section for e^+e^- annihilation to hadrons as a function of centre of mass energy. The Z^0 bosons that are produced in these annihilations decay to $b\bar{b}$ approximately 16% of the time. The b and $\bar{b}$ combine with other quarks and anti-quarks to form beauty hadrons[5] which ultimately decay via charged weak interactions. The virtual $W^{\pm}$ emitted in charged weak decays produce either a charged lepton and a neutrino or an up-type quark and a down-type anti-quark. The purpose of this thesis is to determine how often the virtual $W^{\pm}$ produces an anti-charm quark (in addition to the charm quark that is usually produced when the beauty quark emits the virtual $W^{\pm}$).

Strong Interactions

Quantum Chromodynamics is the theory that describes the strong interaction in the Standard Model. In QCD, quarks interact with each other through the exchange of gluons. Each quark possesses one of three colour charges (red, blue, green). Interaction with a gluon changes the colour charge of a quark. In order to conserve colour at strong interaction vertices, gluons carry colour and anti-colour. Figure 2.4 shows the Feynman diagram for a quark interacting with a gluon. In QCD, gluons can also interact with other gluons. An important consequence of this gluon self-interaction is that as the separation between quarks increases (or momentum transfer, q, decreases), the attractive force between the quarks increases. The attractive force increases because the strong coupling "constant", α_s, increases as the momentum transfer of the reaction decreases. For this reason, α_s is referred to as a

[5]See section 4.2.1 for a description of the hadronization process.

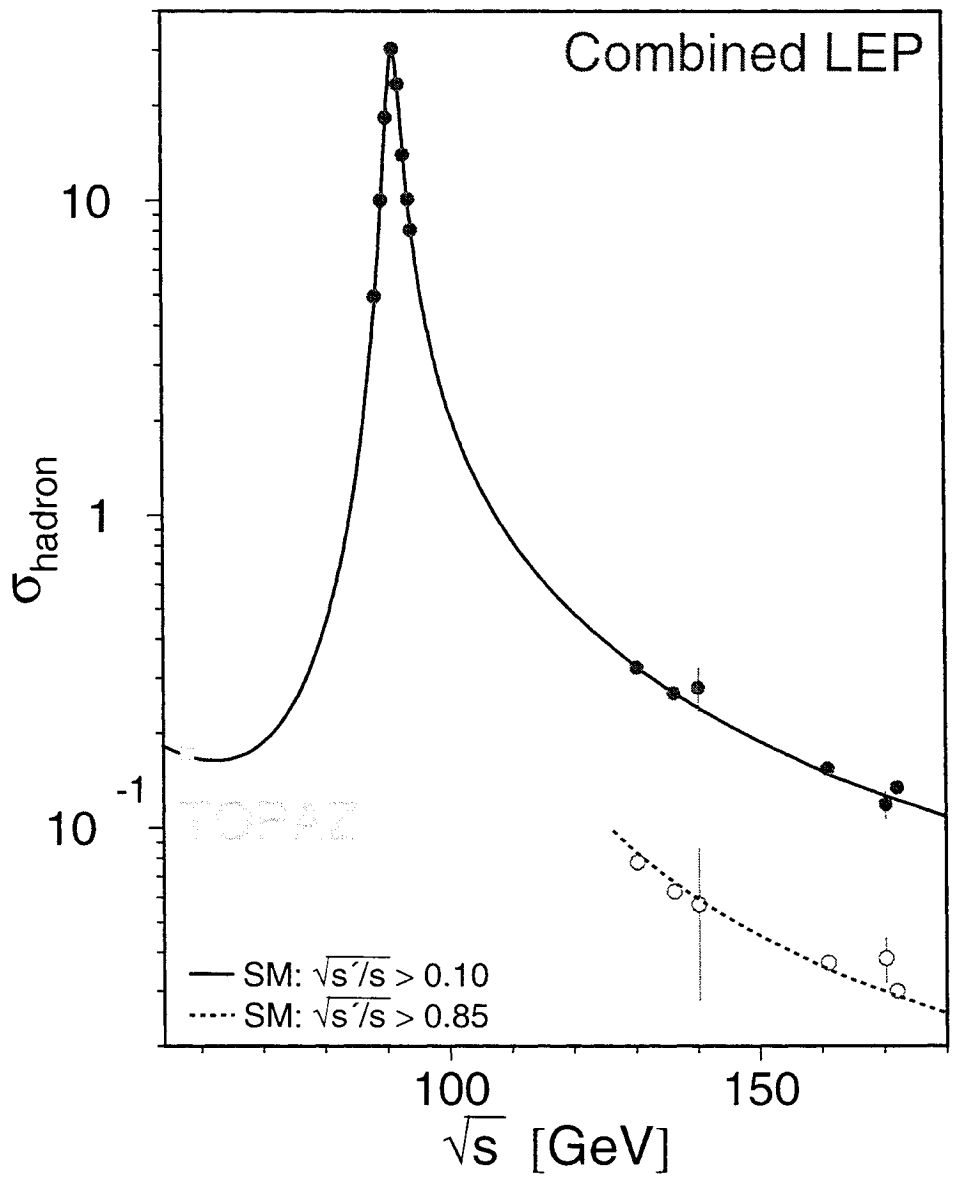

Figure 2.3: Hadronic cross-section for electron-positron annihilation as a function of centre of mass energy ($\sqrt{s}$) [31]. The data point at $\sqrt{s} = 58$ GeV was measured by the TOPAZ collaboration at the TRISTAN electron-positron collider [32]. The variable $\sqrt{s'/s}$ represents the fraction of the summed beam energies measured by the detectors; the cut $\sqrt{s'/s} > 0.85$ rejects events in which the electron or positron radiated a hard photon before annihilation (changing the centre of mass energy of the annihilation). For high energy electron-positron annihilations (> 15 GeV), the hadronic and $b\bar{b}$ cross sections are maximized when $\sqrt{s} = m_{Z^0}$.

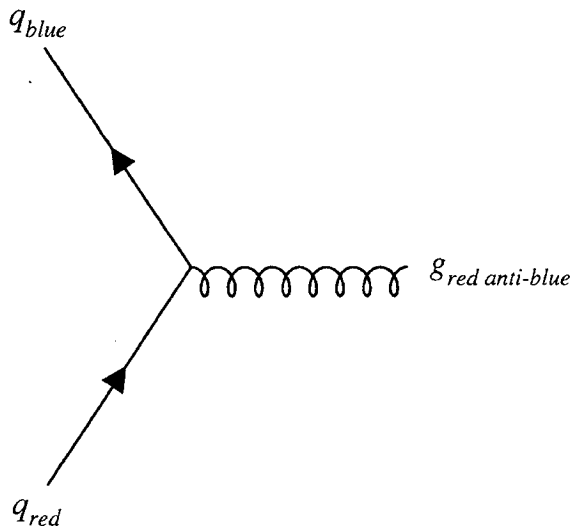

Figure 2.4: Strong interaction vertex: quark coupling to a gluon. A red quark emits a red anti-blue gluon. The quark is blue afterward.

"running" coupling constant. Its dependence on the q^2 of an interaction is given by

$$\alpha_s(|q^2|) = \frac{12\pi}{(11n - 2f)\ln(|q^2|/\Lambda^2_{QCD})} \quad \text{for} \quad |q^2| \gg \Lambda^2_{QCD}, \tag{2.10}$$

where n is the number of colours in QCD (n=3), f is the number of quark flavours in the Standard Model that are kinematically accessible, and Λ_{QCD} is a parameter that also depends on the number of quarks that are kinematically accessible. For strong interactions at the Z^0 resonance (5 quark flavours accessible), $\Lambda_{QCD} = 216^{+25}_{-24}$ MeV [23]. The running of α_s results from colour anti-screening of the quark's colour charge by virtual gluon loops. Since α_s gets larger as quarks get farther apart, quarks are confined to be in hadrons with other quarks or anti-quarks. Because the coupling

between quarks and/or gluons gets very large at small q^2, perturbation theory (which is used for calculations involving the weak and electromagnetic forces) is not valid for calculating strong interactions at small q^2. As a result, it is very challenging to understand soft interactions between quarks and gluons.

2.2 Heavy quark physics

In the remainder of this chapter, various pertinent aspects of the physics of charm and beauty quarks are discussed. The production and detection of beauty quarks is outlined in section 2.2.1. The most successful theory to date for describing the decays of hadrons containing heavy quarks, Heavy Quark Effective Theory (HQET), is briefly summarized in section 2.2.2. Finally, in section 2.2.3, the importance of charm quark/hadron counting in beauty quark/hadron decays is discussed.

2.2.1 Production and detection of heavy quarks

Heavy quarks are produced either in colliding beam or fixed target experiments. Although the beauty quark was discovered at a fixed target experiment at Fermilab, colliding beam experiments have produced almost all of the advances in beauty quark physics in the last 20 years. Electron-positron colliding beam experiments have been particularly successful at making precision measurements of the properties of hadrons containing beauty quarks. This success is largely due to the experimentally clean environment in which the beauty hadrons are produced. The two most fruitful centre of mass energies for b physics in electron-positron annihilations have been at the $\Upsilon(4S)$ and Z^0 resonances. The $\Upsilon(4S)$ resonance (10.58 GeV) decays almost

exclusively to B^+B^- or $B^0\bar{B}^0$ mesons[6] that have very little momentum in the rest frame of the $\Upsilon(4S)$. Many precision b physics measurements have been produced by experiments at the Cornell electron-positron storage ring (CESR), running at the $\Upsilon(4S)$ in Ithaca, New York. The electron and positron beams have the same energy at CESR. Recently, the first measurements of CP violation in B decays have been made at two asymmetric colliding beam experiments running at the $\Upsilon(4S)$: BELLE, at KEK in Japan [33], and BABAR at SLAC [34].

Both the Large Electron Positron (LEP) collider near Geneva, Switzerland and the Stanford Linear Collider (SLC) at SLAC had successful b physics programs running at the Z^0 resonance. As previously mentioned, Z^0 bosons decay to a $b\bar{b}$ pair 16% of the time. The b hadrons that are produced in Z^0 decays possess a large amount of energy so travel at high velocity before decaying. Because of their relativistic velocities, the b hadrons experience time dilation ($\gamma \approx 7.5$) so travel a mean distance of 3 mm in the lab frame before decaying, even though the average b hadron lifetime is approximately 1.5×10^{-12} seconds. The significant separation between the decay points of the b hadrons and the interaction point makes it possible to identify $Z^0 \rightarrow b\bar{b}$ events with high efficiency and purity. Good charged particle tracking resolution is important for identifying b hadron decay points separated from the interaction point. In b physics analyses, events are usually divided into two hemispheres or two "jets" of particles; if one hemisphere/jet is identified ("tagged") as containing a b hadron, then the opposite hemisphere/jet is analyzed. By doing this, a relatively unbiased sample of b decays is obtained. The copious production

[6]Unfortunately there is no universal nomenclature for heavy quark physics. In this thesis, the names of the individual hadrons containing b or c quarks are the standard ones used by the Particle Data Group [23]. Beauty (charm) quarks are referred to by the letter b (c) in italics, "b" ("c"); the $B^{\pm}$, B^0, and $\bar{B}^0$ mesons produced in $\Upsilon(4S)$ decays are collectively referred to as "B mesons"; the different beauty hadrons produced in Z^0 decays are collectively referred to as "b hadrons". The charmed hadrons (including baryons) produced in b hadron decays are collectively referred to as D hadrons.

of b hadrons, long decay lengths, and efficient b tagging made the Z^0 resonance an excellent environment for studying b physics. Many properties of b hadrons, including the properties measured for this analysis, have been measured most precisely at LEP and SLC. These precise measurements have provided stringent tests of Heavy Quark Effective Theory's abiltity to predict the properties of hadrons containing heavy quarks.

2.2.2 Heavy Quark Effective Theory

Beauty hadrons undergo weak decays to three categories of final states: leptonic, semi-leptonic, and hadronic. The tree-level Feynman diagrams showing these processes are depicted in figure 2.5. Leptonic decays are the least difficult to understand theoretically as the only strong interactions are between the q and $\bar{q}$ in the initial state. Semi-leptonic and hadronic decays are more difficult to understand as there is at least one strongly interacting hadron in the final state. Hadronic decays are particularly difficult to understand as the two (or more) hadrons in the final state can interact with each other via the strong force. These strong interactions can occur at momentum transfers where perturbation theory is not valid so the interactions are notoriously difficult to calculate. Fortunately, recent theoretical advances have been made in our understanding of interactions involving heavy quarks [35]. Heavy Quark Effective Theory has enabled the calculation of many of the properties of heavy hadrons, including the quantity that is measured for this thesis.

Heavy Quark Effective Theory (HQET) provides a systematic method for calculating the properties of hadrons containing heavy quarks. HQET is based on the idea of Heavy Quark Symmetry (HQS): according to HQS, the mass of the heavy quark in a hadron can be approximated as being infinite. In this limit, the light anti-quark

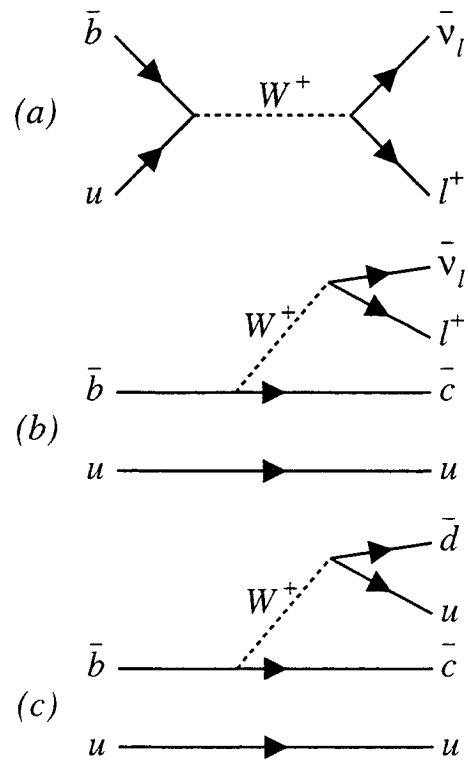

Figure 2.5: Feynman diagrams of weak decays of b hadrons. Diagram (a) shows the leptonic decay of a B^+ meson ($\bar{b}u$ bound state). Diagram (b) shows the semi-leptonic decay of a B^+. Diagram (c) shows the hadronic decay of a B^+.

or quarks that accompany the heavy quark in a hadron do not "see" the quantum numbers of the heavy quark. As a result, the properties of heavy hadrons are largely determined by the properties of the light quarks. The light quarks do not see the quantum numbers of the heavy quark because of the difference in energy/mass scales in the hadron: the soft gluons that bind the quarks together have wavelengths on the order of $1/\Lambda_{QCD}$, while the heavy quark's Compton wavelength $\rightarrow 0$ as its mass $\rightarrow \infty$. The light quark experiences the colour field of the heavy quark but is blind to its other properties: changes in the quantum numbers of the heavy quark (e.g.

spin alignment or flavour) do not change the properties of the heavy hadrons to first order. Of course, the masses of the b and c quarks are not infinite so the first order calculations must be corrected for the finite quark masses. This is where HQET comes in. HQET provides a systematic way of accounting for the masses of the quarks. Expressions for various heavy hadron properties are written as summations of terms containing inverse powers of the heavy quark masses.

HQET is especially useful for calculating the properties of inclusive heavy hadron decays. The inclusive decay rate of a heavy hadron, b, to a final state, f, is given by

$$\Gamma(\mathrm{b} \to f) = \frac{G_F^2 m_b^5}{192\pi^3} \left\{ c_1^f + \frac{c_2^f}{m_b^2} + \dots \right\}, \tag{2.11}$$

where G_F is the Fermi coupling constant, and c_i^f are constants that are calculated using HQET and depend on the final state f. As $m_b \to \infty$, the $1/m_b^n$ corrections $\to 0$. Inclusive calculations are generally more reliable than calculations involving exclusive final states as much of the complicated hadronic physics (e.g. final state interactions) can be ignored if one assumes quark-hadron duality. Quark-hadron duality assumes that the quantum numbers (e.g. flavour) of the final state hadrons are the same as the quantum numbers of the final state quarks. The measurement performed for this thesis is an inclusive measurement of the production of charm quarks in beauty quark decays. This quantity is measured using final state hadrons, so quark-hadron duality is assumed.

2.2.3 Charm counting and $\mathrm{Br}(\mathrm{b} \to \mathrm{D\bar{D}X})$

Studying the decays of b hadrons allows important tests of the Standard Model and HQET to be made. One such test is whether the observed number of charmed

hadrons produced in b hadron decays is consistent with theoretical expectations. A similar test that does not involve hadronic complications is whether the average number of c and $\bar{c}$ quarks produced in the decays of b quarks, n_c, is consistent with theory. One can determine n_c experimentally by measuring the various "topological" branching ratios of b hadrons and summing up the different contributions. One way to write n_c in terms of some of these topological branching ratios is

$$n_c = 1 + \mathrm{Br}(\mathrm{b} \to \mathrm{D}\bar{\mathrm{D}}\mathrm{X}) + \mathrm{Br}(\mathrm{b} \to \text{charmonium}) - \mathrm{Br}(\mathrm{b} \to \text{no charm}). \quad (2.12)$$

This analysis measures the inclusive branching ratio of b hadrons to two charmed hadrons, $\mathrm{Br}(\mathrm{b} \to \mathrm{D}\bar{\mathrm{D}}\mathrm{X})$, and combines this number with previous measurements of $\mathrm{Br}(\mathrm{b} \to \text{charmonium})$ $(= (2.4 \pm 0.3)\%$ [36]) and $\mathrm{Br}(\mathrm{b} \to \text{no charm})$ $(= (0.7 \pm 2.1)\%$ [37]) to obtain n_c. Using HQET, Neubert *et al.* calculate $n_c = 1.20 \pm 0.06$ [38]. The theoretical prediction for n_c is currently limited by uncertainty in the ratio of the charm and beauty quark masses $(0.25 < \mathrm{m}_c/\mathrm{m}_b < 0.33)$.

Besides being interesting in their own right, $\mathrm{Br}(\mathrm{b} \to \mathrm{D}\bar{\mathrm{D}}\mathrm{X})$ and n_c are correlated to the semi-leptonic b hadron branching ratio:

$$\mathrm{Br}(\mathrm{b} \to \ell\nu\mathrm{X}) = \frac{\Gamma_{total} - \Gamma_{hadronic} - \Gamma_{leptonic}}{\Gamma_{total}}, \quad (2.13)$$

where Γ_{total} is the total b decay width, $\Gamma_{leptonic}$ is the width to final states containing only leptons (*e.g.* $\mathrm{B}^+ \to \tau^+\nu_\tau$), and $\Gamma_{hadronic}$ is the width for b decays to final states including only hadrons. The semileptonic b hadron branching ratio has been measured with high precision by CLEO [39] and the four LEP experiments [40–43]. The current combined values for $\mathrm{Br}(\mathrm{b} \to \ell\nu\mathrm{X}) = (10.73 \pm 0.18)\%$ at the Z^0 (LEP) [44] and $\mathrm{Br}(\mathrm{b} \to \ell\nu\mathrm{X}) = (10.45 \pm 0.21)\%$ at the $\Upsilon(4\mathrm{S})$ (CLEO) [39] are slightly lower

than expected by precise theoretical predictions [38, 45, 46][7]. If any component of the hadronic width (*e.g.* b $\rightarrow$ no charm or b $\rightarrow$ D$\bar{\text{D}}$X) is larger than expected, then the measured Br(b $\rightarrow \ell\nu$X) will be in better agreement with theoretical predictions.

Various models incorporating new physics beyond the Standard Model predict a larger charmless b decay width by increasing the $b \rightarrow sg$ [47] or $b \rightarrow s\gamma$ [48] rates. The possibility that a large charmless width is responsible for the discrepancy is unlikely though, as recent experimental results from LEP [49, 50], CLEO [51] and BELLE [52] have set tight limits on these charmless decays. If the $b \rightarrow c\bar{c}s$ rate (mainly b $\rightarrow$ D$\bar{\text{D}}$X) is larger than expected, this too can reconcile the experimental Br(b $\rightarrow \ell\nu$X) results with theory [38, 53–56].

Previous analyses measuring n_c at the Υ(4S) and Z^0 resonances have either reconstructed exclusive final state D hadrons [57–60] or used more inclusive techniques [37, 61]. The only inclusive analysis for charm counting published to date is by the DELPHI collaboration [37]. The DELPHI analysis uses the joint probability variable to determine the fractions of different b hadron decay modes and backgrounds present in their data. The SLD collaboration has also measured n_c using an inclusive technique that takes advantage of the excellent vertex reconstruction abilities of their detector [61]. The analysis presented in this thesis makes the first inclusive measurement of Br(b $\rightarrow$ D$\bar{\text{D}}$X) and n_c using data collected by the OPAL detector. This analysis uses a technique similar to the one employed by DELPHI; the joint probability variable is used to discriminate amongst the different b decay topologies.

The joint probability is a measure of the separation between the e^+e^- interaction point and an ensemble of charged particles (which produce tracks in the OPAL

[7] All of these theoretical predictions for Br(b $\rightarrow \ell\nu$X) are inconsistent with the experimental values except the prediction of Neubert *et al.* [38].

detector). Large joint probability means the tracks in an ensemble appear to have originated at the interaction point; small joint probability means the tracks appear to have originated far from the interaction point. The finite lifetimes of the weakly decaying D hadrons produced in b hadron decays are used to separate double charm b decays from the dominant single charm b decays. The long lifetime of the D hadrons means that single charm b hadron decays will tend to have larger joint probabilities than double charm b hadron decays.

Chapter 3

The LEP Collider and the OPAL Detector

3.1 The LEP Collider

The Large Electron Positron (LEP) Collider at the European Laboratory for Particle Physics (CERN) near Geneva, Switzerland collided beams of electrons and positrons at high energy from May 1989 to November 2000. From 1989 to 1995, the centre of mass energy, $\sqrt{s}$, of the electron-positron collisions was at or near the mass of the Z^0 boson. From 1995 to 2000, the energy of the beams was increased in order to produce pairs of $W^{\pm}$ and Z^0 bosons and also to search for new particles. The LEP collider was removed from the LEP tunnel after 2000 to make way for the construction of the Large Hadron Collider. The following sections describe the LEP collider from 1993 to 1995 as the data used for this analysis were collected during these years at $\sqrt{s} = m_{Z^0}$.

3.1.1 Production of e^+ and e^-

The electrons used in the LEP collider were obtained from a thermionic electron gun. A metal filament in the electron gun emitted electrons when heated by a high current. The emitted electrons were accelerated by a 200 MeV linear accelerator into a tungsten target. The 200 MeV electrons interacted with the target material to produce pairs of electrons and positrons. The positrons produced in the target and electrons produced by the electron gun were transferred by electric and magnetic fields to the next in a chain of accelerators that ended with the LEP collider.

3.1.2 Acceleration of e^+ and e^-

After the tungsten target, the electrons and positrons underwent four stages of acceleration. A different accelerator was used for each stage of acceleration. A schematic view of the accelerator complex at CERN is shown in figure 3.1. The first stage of acceleration was provided by a 600 MeV linear accelerator. After being accelerated to 600 MeV, the electrons and positrons were transferred to the Electron Positron Accumulator (EPA). The 200 and 600 MeV linear accelerators (linacs) and the positron producing target are collectively called the LEP Injector Linac (LIL). The LIL ran at 100 Hz at low intensity (especially for the positrons) while the next stage of acceleration was at 10 Hz and required much higher particle intensities [62]. The EPA allowed the electron and positron bunch frequency to be reduced and the intensity to be increased before transfer to the next stage of acceleration. After accumulating in the EPA, the electrons and positrons were transferred to the CERN Proton Synchrotron (PS). The Proton Synchrotron accelerated the particles around its 630 m circumference to 3.5 GeV before transferring them to the Super Proton Synchrotron (SPS). The 6.9 km circumference Super Proton Synchrotron provided

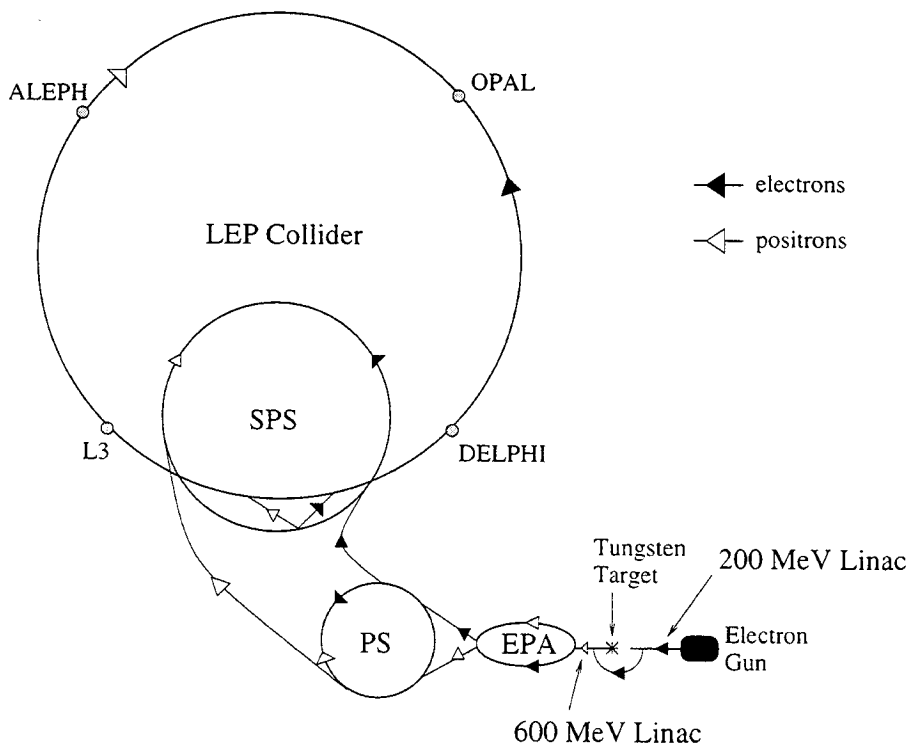

Figure 3.1: Schematic view of the accelerator complex at CERN. Only those machines that accelerated electrons and positrons are shown. The different accelerators are not drawn to scale.

the final stage of acceleration before injection into the LEP ring. The electrons and positrons entered the LEP ring at 20 GeV.

The LEP collider was 26.6 km in circumference and was located underground at depths from 50 m to 150 m. The collider tunnel was dug at a 1.4% incline so that most of the tunnel and all of the experimental cavities could be located in solid rock. The LEP collider accelerated bunches of positrons and bunches of electrons from 20 GeV to 45.6 GeV (or higher energies from fall 1995 to 2000). Each bunch contained approximately 10^{11} particles. For the period of data-taking relevant for this thesis, the LEP collider's radio-frequency (RF) acceleration was provided by 128 copper cavities. The RF cavities operated at 352.21 MHz and were powered by 16 klystrons providing 1 MW of power each. The peak voltage available for acceleration was 400 MV per revolution.

Once the beams were accelerated to collision energies, they still required power to maintain their energies because energy was lost due to synchrotron radiation. The rate of energy loss due to synchrotron radiation, P, for a positron or electron is

$$P = e^2\beta^4 \left(\frac{E}{m_e c^2}\right)^4 \frac{1}{\rho^2}, \tag{3.1}$$

where e is the electric charge of an electron, c is the speed of light in a vacuum, β is the particle's velocity divided by c, E is the energy of the particle, m_e is the electron rest mass, and ρ is the particle's radius of curvature.

At 45.6 GeV, the electrons and positrons were travelling at essentially the speed of light so they circulated in the collider at approximately 11 kHz. During 1993 and 1994 (1995), LEP operated with 8(4) bunches of positrons and 8(4) bunches of electrons so the rate at which the bunches crossed at 16(8) locations on the ring was 176(88) kHz. The electrons and positrons were brought into collision at four

equally separated locations on the LEP ring. At the other locations where the beams passed each other, the beam orbits were altered by electrostatic separators so that the beams did not interact. This was done to increase the useful lifetime of the beams. The bunch crossing rate at each of the four collision points was 88(44) kHz. A multi-purpose particle detector was located at each of these four locations. The data used in this thesis were collected by the OPAL detector. The other three detectors were ALEPH, DELPHI and L3.

The length of time a set of 8(4) bunches was circulated in the collider (called a "fill") was determined by the rate at which the beam currents were reduced. Beam currents were reduced mainly by beam-beam bremsstrahlung and Compton scattering of the beam particles off thermal photons emitted by the beam pipe [63]. The duration of each fill was typically between six and twelve hours. After each fill, new bunches of electrons and positrons were injected into LEP.

3.1.3 Collision of e^+ and e^-

To bring the beams into collision required excellent control over the orbits of the beams. Control of the beams' orbits was provided by electric and magnetic fields. The most basic requirement for the collider was to steer the beams through the evacuated beam pipe. The vacuum in the pipe was maintained at less than 10^{-10} Torr in order to minimize beam-gas interactions. The beams were bent around the LEP collider by 248 large sets of magnets [64]. Each set was composed of 12 0.1 T dipole bending magnets and several quadrupole, sextupole and octopole focussing magnets. The two quadrupoles in each set were arranged so that their poles were rotated by 90° with respect to each other to provide "strong focussing" of the beams. Focussing reduced the cross-sectional area of the beams, thereby increasing the beam lifetimes

and increasing the luminosity, or intensity of the colliding beams, at the detectors. The sextupole magnets were used to make chromaticity corrections; chromaticity is the tendency of particles with different energies to have different focal lengths when focussed by magnets. The octopole magnets were used for further corrections to the focussing of the beams. In addition to the aforementioned sets of focussing magnets, superconducting quadrupole magnets were located close to both ends of each of the four detectors to further squeeze the beam profiles to approximately 8 μm $\times$ 200 μm in the vertical and horizontal directions. The bunches were approximately 1.8 cm long.

The luminosity of colliders, $\mathcal{L}$, is governed by

$$\mathcal{L} = \frac{N_1 N_2 f n}{A}, \tag{3.2}$$

where N_1 and N_2 are the numbers of particles in each of the electron and positron bunches, f is the frequency at which the bunches circulate in the collider, n is the number of positron or electron bunches (assuming an equal number of each) and A is the area of overlap between the two beams. As $\mathcal{L}$ is inversely proportional to the cross-sectional area of the beams, reducing the beam profile increases the luminosity at the detectors. This also increases the interaction rate,

$$R = \sigma \mathcal{L}, \tag{3.3}$$

where σ is the total cross section for interactions. The luminosity at LEP was approximately 2×10^{31} cm^{-2}s^{-1} for Z^0 running.

3.2 The OPAL Detector

The Omni-Purpose Apparatus at LEP (OPAL) was one of four multi-purpose particle detectors at the LEP collider. Its objectives were to make precise measurements of Standard Model processes and parameters and to search for physics beyond the Standard Model. These objectives were met by constructing a nearly hermetic detector capable of measuring many different properties of the neutral and charged particles produced in high energy electron-positron annihilations. The OPAL detector measured the trajectory, momentum, energy, time of flight, electric charge, and rate of energy loss for charged particles. For neutral particles other than neutrinos, the OPAL detector measured their direction and energy. Reliable particle identification was achieved by combining information from different portions of the detector (particularly the rate of energy loss in the gaseous tracking system and the amount of energy deposited in the different sub-detectors). Due to the hermeticity of the detector and momentum conservation, it was also possible to determine the vector sum of the momenta of any neutrinos produced in an electron-positron annihilation.

In order to measure these many different properties of particles produced in electron-positron annihilations, the OPAL detector was composed of many specialized sub-detectors. Each sub-detector was responsible for specific measurement tasks. A schematic view of the OPAL detector is shown in figure 3.2. The sub-detectors that constituted OPAL will be described in the rest of this chapter, with emphasis on the sub-detectors that are most important for this analysis: the sub-detectors that make up the charged particle tracking system. Most of the details of the OPAL detector that are provided in this chapter were obtained from reference [65].

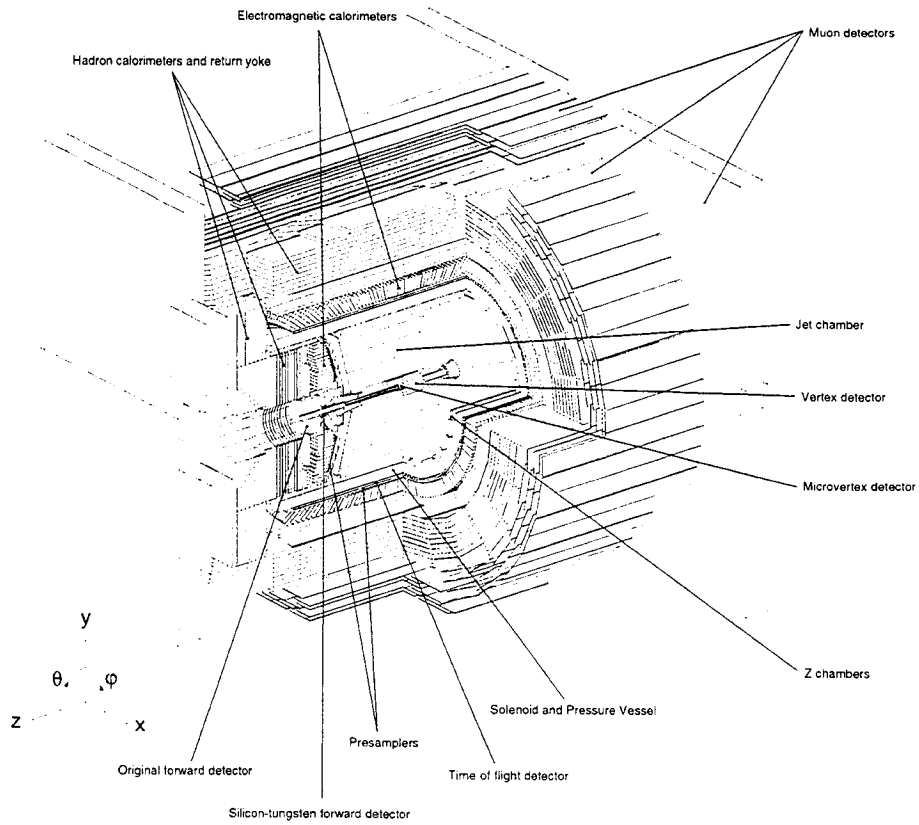

Figure 3.2: Schematic view of the OPAL detector. The microvertex detector (or silicon vertex detector) is closest to the beam pipe. The gaseous tracking chambers are located outside the silicon vertex detector. The tracking chambers are inside the solenoid that produces an axial magnetic field in the tracking chambers. The barrel sections of the electromagnetic and hadronic calorimetry are located outside the solenoid. The endcap sections of the electromagnetic and hadronic calorimeters are located at either end of the the barrel. The outermost layer of the OPAL detector is the muon detection system.

3.2.1 Charged particle tracking system

OPAL's charged particle tracking system consisted of gaseous tracking chambers and a silicon vertex detector. The trajectories of charged particles, "tracks", through the gaseous detectors were reconstructed by observing electrical signals produced in the gas that was ionized by the passage of charged particles. Under the influence of electric fields generated by high voltage wires in the tracking chambers, the ionization electrons drifted towards sense wires in the chambers. The ionization electrons underwent charge multiplication via the electron avalanches that occurred in the high electric fields close to the sense wires. The displacement of the resulting positive ions and electrons by the electric field induced a current in the sense wires. The locations of the wires and the drift times of the ionization charge were used to determine points in space where the ionizing charged particles had been. Once many space points are determined, the trajectory of the charged particle is estimated by the best fit of a helix to these points [66]. The trajectories were helical as the tracking system was in a 0.435 T axial magnetic field that was generated by the solenoid surrounding the tracking chambers.

After a helical track is fitted in the gaseous tracking chambers, the track is extrapolated back towards the silicon vertex detector to determine whether the track can be associated with any "hits" in this detector. Locations of energy deposition in the silicon vertex detector, hits, are tested for consistency with having been produced by the same charged particle that produced the track in the gaseous tracking chambers. Those tracks that have silicon detector hits associated to them are re-fit to re-determine their track parameters. The silicon detector had excellent position resolution so it improved the precision of the track parameters. In addition, hits in the silicon detector were very useful for resolving tracks that overlapped in the

gaseous tracking detectors. For a brief description of the OPAL track parameters and co-ordinate system, the reader is directed to Appendix A.

Once the track fitting is completed, the electric charge, q, and momentum of the charged particle can be determined. The sign of q is determined by the direction the particle is deflected in the axial magnetic field, $\vec{B}$, using

$$\vec{F} = q\vec{v} \times \vec{B}, \tag{3.4}$$

where $\vec{F}$ is the Lorentz force on the particle, and $\vec{v}$ is the velocity of the particle. The momentum, p, of a particle is determined from two parameters of the fitted helical track: the dip angle, λ, and ρ, the radius of curvature (in metres) of the particle in the $r - \phi$ plane. The momentum is related to these quantities by

$$p = \frac{0.3\rho B}{\cos\lambda}, \tag{3.5}$$

where B (in tesla) is the magnitude of the axial magnetic field. This equation assumes that the magnitude of the electric charge of the particle is equal to the magnitude of the charge of an electron.

Silicon vertex detector

The OPAL silicon vertex detector was the sub-detector that was closest to the beampipe. It is a vital sub-detector for this analysis as it helped to provide excellent track parameter resolution. The silicon vertex detector was first operational in 1991. In 1991 and 1992 it provided information only in the $r - \phi$ plane. In 1993 the silicon vertex detector was upgraded to provide z information as well. The silicon detector was upgraded again in 1995 to improve its geometrical acceptance. Details

of the silicon detector will be provided for 1993 to 1995. The details about the silicon detector that are provided in this section were obtained from references [67–69].

The silicon detector was composed of many 3.3 cm × 6.0 cm wafers of silicon which were 250 μm thick. Charged particles that passed through the silicon deposited small amounts of energy through ionization. The ionization resulted in charge accumulating on the parallel thin conducting strips that were on the surface of the silicon. A voltage was applied across the wafer to facilitate charge collection on the conducting strips. Pairs of wafers were glued back-to-back so that the strips on one wafer were orthogonal to the strips on the other wafer. The strips on one wafer gave ϕ information, and the strips on the other wafer gave z information. The third co-ordinate, r, was determined by the radial separation between the hit location on the silicon wafer and the beam line. The conducting strips on the silicon were 25 μm apart. The wafers that measured ϕ had every second strip capacitively-coupled to a readout aluminum strip. The wafers that measured z had every fourth strip capacitively-coupled to a readout strip. There were 30,325 readout strips in 1993-1994.

Charge produced by the passage of a single ionizing particle was measured by many adjacent readout strips. This means that the best estimate of the hit location of the particle is determined by using information from all the adjacent readout strips that measured current significantly above background. A weighted mean of the locations of the readout strips with significant current provides an estimate of the track location that is much more precise than the 50(100) μm readout strip pitch; the spatial resolution obtained with this method is 5(13) μm for minimum ionizing particles at normal incidence to the silicon. The mean of the locations is weighted by the pulse heights from each of the readout strips.

The silicon detector was arranged in two approximately cylindrical layers located

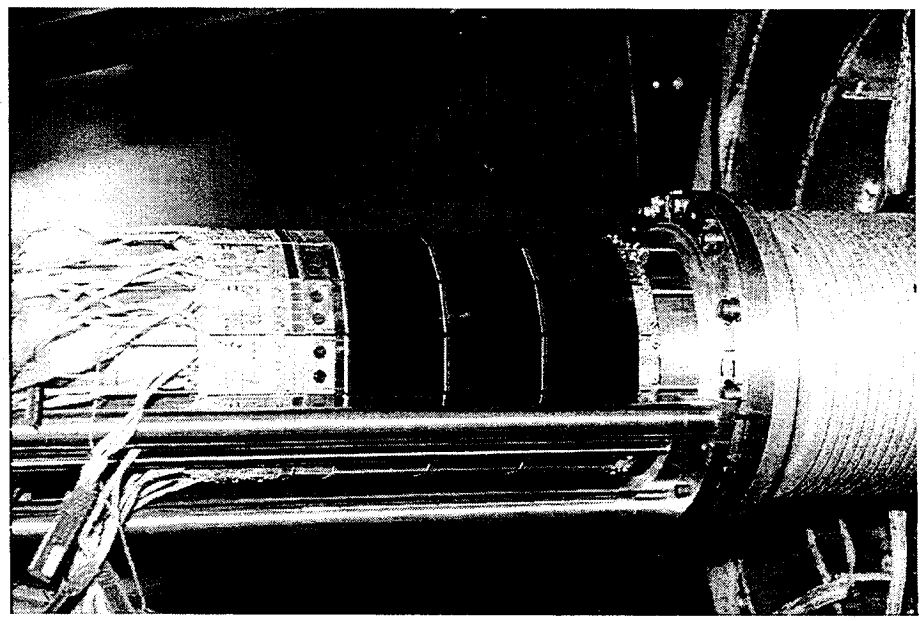

Figure 3.3: The OPAL silicon vertex detector during installation around the beam pipe. Several of the ladders of the outer layer of the detector are visible. The three wafers in each ladder are clearly visible, as are the readout electronics on the left side of the ladders.

very close to the beam pipe. The inner layer was located at a radius of 6.1 cm. The outer layer was located at 7.5 cm. The inner layer was made out of 11 rows (or "ladders") of silicon wafers (12 ladders in 1995). The outer layer was made out of 14 ladders (15 ladders in 1995). In both the inner and outer layers, the ladders were composed of 3 back-to-back pairs of wafers attached end to end. Figure 3.3 shows the silicon vertex detector during installation around the beam pipe. The maximum $|\cos\theta|$ acceptance was 0.83 for the inner layer and 0.77 for the outer layer. The ϕ acceptance of each layer was not 100% as there were narrow gaps between the active regions of the silicon wafers. The ϕ acceptance was improved in 1995 by adding one extra ladder to each layer; this decreased the size of the gaps between the active regions of the wafers. Because of the non-uniform acceptance, the inner and outer ladders were arranged so that gaps between ladders did not line up with the beam

line.

The intrinsic position resolution for 5 GeV pions was measured to be 5 μm for the ϕ wafers. For the z wafers, the resolution was 13 μm. In conjunction with the rest of the OPAL tracking system, the silicon detector helped to provide 18 μm impact parameter (d_0) resolution for di-lepton events. Tracks from hadronic Z^0 decays with $r\phi$ and z hits in both the inner and outer layers of the silicon detector (the tracks used in this analysis) had a mean d_0 resolution of approximately 80 μm.

Vertex drift chamber

The OPAL vertex chamber was a cylindrical precision drift chamber that was composed of 36 axial and 36 stereo sectors. Charged particles passing through the vertex chamber ionized the gas mixture inside the chamber. By making precise measurements of the drift times of electrons resulting from this ionization, precise measurements of track $r\phi$ coordinates were made (55 μm resolution). The wires in the axial sectors were parallel to the beam line, while the wires in the stereo sectors made a 4° angle with the axial wires. The combination of hit information from the stereo and axial wires provided a reasonably precise measurement of the z coordinates of tracks (700 μm resolution). A less precise but quicker measurement of z (4 cm resolution) was also provided by measuring the time difference between signals received at either end of a hit axial wire. The less precise z information was used for the track trigger (see section 3.2.8).

The vertex chamber was 1.00 m long and subtended polar angles from 18° to 162°. The inner radius of the vertex chamber was 8.8 cm from the beam axis and the outer radius was at 23.5 cm. The vertex chamber, jet chamber and zed chambers were contained in a pressure vessel as the gas in these chambers was at 4 bar. The gas was maintained at high pressure in order to improve the resolution of ionization

energy loss measurements in the jet chamber. A thin aluminised mylar cylinder separated the gas mixture in the vertex chamber from the gas mixture in the jet chamber. The gas mixture in the vertex, jet and zed chambers was 88.2% argon, 9.8% methane and 2.0% isobutane. Very small amounts of water vapour were also added to the gas mixture to increase the longevity of the chamber.

Each axial sector consisted of one plane of anode wires with cathode planes on either side. Each anode plane was made up of 12 anode wires that were 5.83 mm apart. Between the anode wires were potential wires for field shaping purposes. The anode wires were staggered by 82 μm in order to determine from which side of the anode plane the ionization electrons had originated. The cathode wires were maintained at a negative voltage while the anode wires were kept at ground potential. The drift fields were typically 2 kV/cm. The stereo sectors were similar except they had six sense wires per anode plane and the stereo wires made a 4° angle with the axial wires.

Jet chamber

The jet chamber was the largest volume sub-detector in the charged particle tracking system of OPAL. Like most of the sub-detectors in OPAL it was cylindrically symmetric about the beam axis. It worked the same way as the vertex chamber except all the wires were parallel to the beam axis so precise measurements of the z coordinates of tracks were not available. Instead, a rough measurement of z (6 cm resolution) was made by comparing the amount of charge collected at either end of a hit wire (charge division method). Since drift times in the jet chamber were longer than those in the vertex chamber, the precision with which the jet chamber measured the $r\phi$ coordinates of tracks (135 μm resolution) was not as good as the precision of the vertex chamber.

The jet chamber was 4 m long and its inner and outer radii were 0.25 m and 1.85 m. The jet chamber subtended 98% of the solid angle for tracks with at least eight wire hits possible ($11° \leq \theta \leq 169°$). The chamber was divided into 24 sectors with one plane of 159 anode sense wires per sector. The anode sense wires were spaced 1.00 cm apart and were staggered by 200 μm. Potential wires at -2.38 kV were located in the anode plane between each sense wire. Between the anode planes, planes of high negative voltage (-25 kV to -2.5 kV) cathode wires constituted the boundaries between the jet chamber sectors.

Besides measuring the tracks from charged particles, the jet chamber was vital also for particle identification. By measuring the rate of energy loss, dE/dx, and the momentum of charged particles, it is possible to distinguish between different charged particle species. The rate of energy loss by a charged particle is estimated by measuring the size of the induced electrical signal on each hit wire. Figure 3.4, a plot of dE/dx versus momentum, shows the separation between different charged particle species obtained by this method.

Zed chambers

The OPAL zed chambers were located just outside the jet chamber and inside the tracking system pressure vessel. The zed chambers made precise measurements of the z coordinates of tracks in the barrel portion of OPAL; the resolution was 100 μm to 350 μm, depending on the track polar angle. For polar angles $|\cos\theta| \leq 0.72$, the acceptance in ϕ was 94%. The zed chambers were drift chambers so worked in the same manner as the vertex and jet chambers. The main difference between the zed chambers and the other gaseous tracking chambers was the segmentation of the chambers and the geometry of the wires inside them. The zed chambers were composed of 24 rows of 8 rectangular drift chambers attached end to end. Each

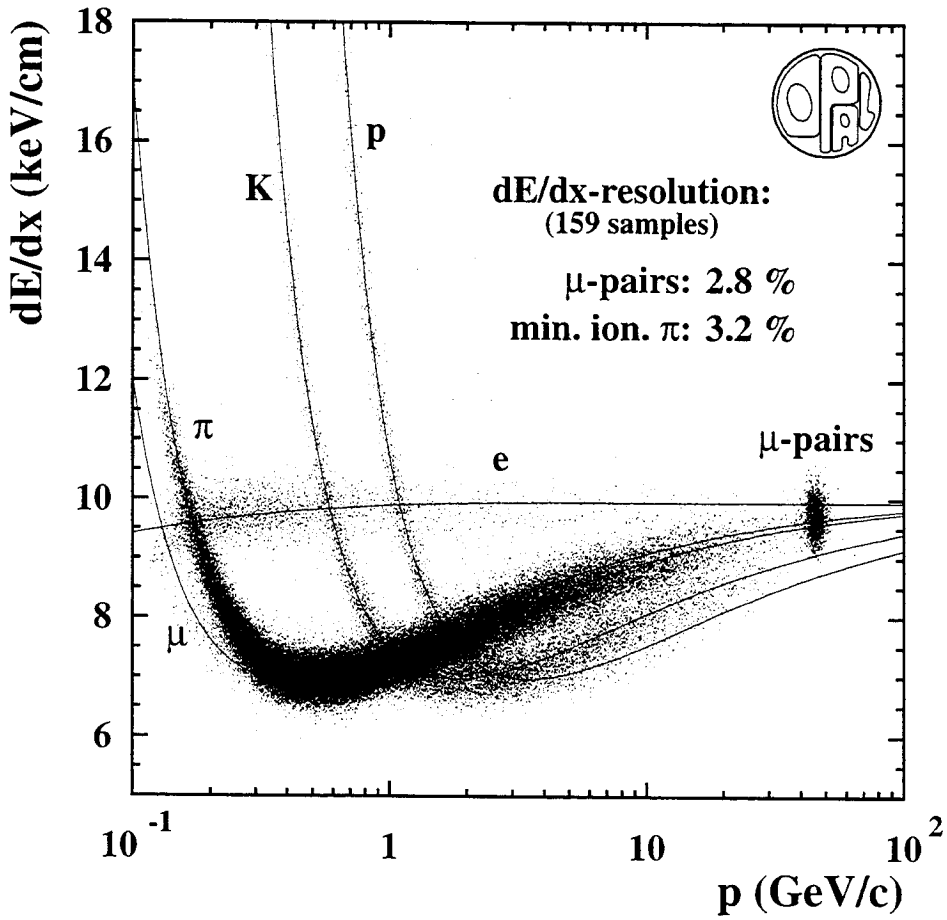

Figure 3.4: Measured dE/dx as a function of momentum for tracks in hadronic and muon pair Z^0 decays [70]. The smooth functions represent the expected dE/dx as a function of momentum for different charged particle species. The dE/dx resolution for muon pairs and minimum ionizing pions with at least 159 samples of dE/dx is indicated in the figure.

rectangular drift chamber cell was 50 cm × 50 cm and 5.9 cm thick. The plane of six anode sense wires in each cell was located in the $x - y$ plane so that ionization electrons drifted in the z-direction. The sense wires were spaced 4 mm apart and were staggered by 500 μm. This allowed precise measurements of the z-coordinates of tracks to be made. Charge division was used to make a rough ϕ measurement for tracks (1.5 cm resolution).

3.2.2 Magnet

The 0.435 T axial magnetic field in the OPAL tracking system was produced by a solenoidal coil located just outside the tracking system pressure vessel. Measuring the curvature of charged particles in the magnetic field allowed the momentum and sign of the electric charge of charged particles to be determined (see section 3.2.1). In order to minimize the number of radiation lengths in the detector before the calorimeters, the coil was self-supporting and composed of aluminum and glass epoxy. The return yoke for the magnetic field was located just outside the electromagnetic calorimeter, 3.39 m to 4.39 m from the beam axis. The yoke was made of 10 cm thick soft steel plates that had the gaps between them instrumented to provide hadron calorimetry.

3.2.3 Time of flight detectors

Before 1996, time of flight (TOF) detectors were located only in the barrel region of the detector; in 1996 endcap TOF detectors were added to OPAL. The barrel TOF detector was composed of one hundred and sixty 684 cm × 9 cm panels. The panels were located at a mean radius of 2.36 m so covered the polar angle range $|\cos\theta| \leq 0.82$. The TOF detectors measured the length of time it took a charged

particle to travel from the interaction point to the TOF detectors. The time of flight information was used for trigger purposes and also for particle identification for low energy (0.6 to 2.5 GeV) particles. The TOF detectors were made out of scintillator material, so they detected the passage of a charged particle by the scintillation light it produced. The scintillation light propagated through plexiglass light guides that were glued to the ends of the scintillator panels. The light guides were coupled to photomultiplier tubes which detected the scintillation photons.

3.2.4 Electromagnetic calorimetry

The electromagnetic (EM) calorimeter was composed of 11,704 high density lead glass blocks coupled to light detection devices. High energy particles that entered the EM calorimeter initiated electromagnetic showers that produced Čerenkov photons in the glass. The sides and front (side closest to the interaction point) of the glass blocks were covered with reflective aluminum to increase the number of photons reaching the backs of the blocks where the photons were detected. In the barrel portion of the EM calorimeter, the photon detection was performed by photomultiplier tubes optically coupled to the blocks. In the endcap portion of the EM calorimeter, the light detection was performed by vacuum photo triodes which are capable of functioning in high magnetic fields. The amount of light measured by the light detectors is proportional to the amount of energy that was deposited in the blocks.

There were approximately 24.6(22) radiation lengths of material between the interaction point and the outside of the barrel(endcap) portion of the EM calorimeter. This ensured that electromagnetic showers were almost always fully contained in the EM calorimeter. Hadrons that passed through the electromagnetic calorimeter usually started to shower (i.e. deposit energy) in the glass blocks too; however,

most of a hadron's energy was deposited in the hadron calorimeter outside the electromagnetic calorimeter. The intrinsic energy resolution for electrons and photons was $0.2\% + 6.3\%/\sqrt{E}$ for the barrel and $5\%/\sqrt{E}$ for the endcaps, where E was the energy of the particle in GeV.

The EM barrel calorimeter was composed of 9,440 lead glass blocks (radiation length = 1.50 cm) that were aligned to point close to the interaction point. The lead glass blocks in the barrel were 10 cm × 10 cm and 37 cm deep. The EM barrel had polar angle polar angle coverage for $|\cos\theta| \leq 0.81$. The EM endcap calorimeter was composed of 2,264 blocks (radiation length = 2.51 cm) that were aligned parallel to the beam line. These blocks were 9.2 cm × 9.2 cm and 52 cm deep. The EM endcap provided polar angle coverage from $0.81 \leq |\cos\theta| \leq 0.98$.

Electromagnetic showers tended to start before the glass blocks of the EM calorimeter as there were approximately two radiation lengths of material between the interaction point and the EM calorimeter. As a result, pre-sampling devices were used for both the barrel and endcap regions. These detectors estimated the amount of energy lost by an electromagnetic shower before the lead glass blocks. The pre-sampling detectors estimated the amount of energy lost by measuring the number of charged particles passing through the detectors. The resolution of electromagnetic energy measurements was improved by including information from these devices. The precise location of an electromagnetic shower was also measured by the pre-sampling detectors. In the barrel region, the pre-sampling detector was located immediately in front of the glass blocks and was composed of two cylindrical layers of drift tubes. The endcap pre-sampler was also located immediately in front of the glass blocks and was composed of multiwire proportional chambers.

3.2.5 Hadronic calorimetry

The hadronic calorimeter was divided into three sections: barrel, endcaps and pole-tips. The barrel covered $|\cos\theta| \leq 0.81$; the endcaps covered $0.81 \leq |\cos\theta| \leq 0.91$; the pole-tips covered $0.91 \leq |\cos\theta| \leq 0.99$. Combined, the three sections of the hadronic calorimeter subtended 97% of the solid angle.

As mentioned in section 3.2.2, the hadronic calorimeter made use of the steel magnetic field yoke by instrumenting the gaps between the layers of steel. The steel acted as an absorber for this sampling calorimeter. The hadronic calorimeter provided 4.0 or more interaction lengths of material so almost all hadronic showers were fully contained. In the barrel and the endcap portions of the calorimeter, the gaps were instrumented with limited streamer tubes. The gaps in the pole-tips were instrumented with multiwire proportional chambers. The gas mixtures were 75% isobutane and 25% argon in the streamer tubes, and 45% n-pentane and 55% carbon dioxide in the multiwire proportional chambers. Charged particles in the hadronic showers ionized the gas in the detectors, after which, the liberated charge was detected by readout strips and pads in the detectors. The amount of charge detected was roughly proportional to the energy of the hadronic shower. To improve the energy resolution, a correction is made to account for the amount of energy deposited by hadronic showers in the EM calorimeter. There were approximately 2.2 interaction lengths of material (mostly in the EM calorimeter) before the hadronic calorimeter, so most hadronic showers started before they reached the hadronic calorimeter. After correcting for this, the energy resolution for the hadronic calorimeter was approximately $120\%/\sqrt{E}$, where E is the hadron energy in GeV.

3.2.6 Muon detectors

The muon detectors were the outermost sub-detector of OPAL. Besides neutrinos, the only particles that usually passed through the hadronic calorimeter without stopping were muons. Muons are identified by associating hits in the muon detectors to tracks in the central tracking chamber; for a muon candidate to be accepted, the alignment of the muon detector hits and a track in the central tracking chamber must be consistent with the amount of multiple coulomb scattering expected from a muon. As there were typically 8 interaction lengths of material between the interaction point and the muon detectors, the probability to mis-identify a pion as a muon was less than 1%, while the efficiency to detect muons over 3 GeV was virtually 100%.

The muon detectors were divided into two sections: the barrel and the endcaps. The barrel muon detector was composed of four layers of long drift chambers arranged cylindrically around the barrel hadronic calorimeter. The drift chambers contained anode wires that ran parallel to the beam line, so the drift time to an anode wire provided a precise measurement of the ϕ coordinate of a muon (1.5 mm resolution). Cathode pads were located on the inside of the chamber walls; induced charge on these pads was combined with charge division and time difference information from both ends of the anode wires to make precise measurements of the z coordinates of muons (2 mm resolution). The barrel drift chambers contained a gas mixture composed of 90% argon and 10% ethane. The muon barrel detectors covered $|\cos\theta| \leq 0.72$.

The muon endcap detectors were composed of four layers of limited streamer tubes. The high voltage anode wires in two of the layers were horizontal while the anode wires in the other two layers were vertical. The location of a hit in an endcap muon layer was determined by measuring the induced charge (resulting

from ionization in a limited streamer tube) on conducting strips on both sides of a layer. The strips on either side of a layer were orthogonal so that x and y muon hit coordinates could be determined from a single layer. The spatial resolution of a muon hit was approximately 1 mm. The muon endcap detectors were filled with a gas mixture of 75% isobutane and 25% argon. For most of the azimuthal angle (there were small gaps for cables from the inner detector and for supports for the magnet), the polar angle acceptance was $0.67 \leq |\cos\theta| \leq 0.98$.

3.2.7 Forward detectors

The forward detectors were responsible for detecting particles whose trajectories were very close to the beam pipe. They were installed to improve the hermeticity of the OPAL detector and to determine the luminosity at the OPAL interaction point. The luminosity was measured by counting electrons and positrons scattered at small polar angles (Bhabha electrons). Several different sub-detectors made up the forward detectors: a silicon tungsten precision calorimeter (for luminosity measurements), particle trackers and high energy photon detectors.

3.2.8 Trigger, data acquisition and data recording

Depending on the year of data taking (see section 3.1.2), an electron-positron bunch crossing occurred in the OPAL detector every 11 or 22 μs. However, it took approximately 20 ms to read out all the data from all the sub-detectors. This meant that data from every bunch crossing could not be read out. Instead, for each bunch crossing, a quick decision (< 11 μs) had to be made to determine whether an interaction had occurred that was worth reading out and recording. The decision to read out the data from a bunch crossing was performed by the OPAL trigger.

A small fraction of the data collected by the sub-detectors during a bunch crossing was sent to the OPAL trigger. The trigger combined data from the track trigger unit (dedicated hardware that combined limited hit information from the vertex and jet chambers), the time of flight detector, the EM calorimeter, the hadron calorimeter, the muon detector, and the forward detectors in the central trigger logic to decide whether to read out an event. Events were read out if the trigger received positive "stand alone" trigger inputs or if there existed spatially correlated signals from different sub-detectors. Trigger information from the different OPAL sub-detectors was divided into 6×24 bins in θ and ϕ respectively. The "stand alone" trigger conditions were generally met if there were ≥ 2 tracks, or if a significant amount of energy was deposited in the sub-detectors.

The data that each of the sub-detectors collected was initially buffered on its own local system crate (LSC). If one of the trigger conditions was satisfied then the (global) trigger unit signalled the sub-detector LSCs to process their data more, in preparation for data acquisition. After the "frond end" processing was completed in the LSCs, the data from the different sub-detectors were transferred to the "event builder". The event builder combined the data from all the sub-detectors. The combined data was passed to the "filter" system which performed a quick software analysis of each event in order to make a final decision about whether or not to record the data from an event. The filter was effective at identifying unwanted background events.

Once the filter decided to accept an event, the data from that event was transferred via optical cables from the detector area to the surface. All processing up to and including the filter was performed in the underground experimental hall. On the surface, the event was fully reconstructed by dedicated workstations using the latest available calibration data. Copies of the reconstructed events were recorded

on optical discs, magnetic tapes and hard disks for future physics analyses. An example of a fully reconstructed hadronic Z^0 decay in OPAL is shown in figure 3.5

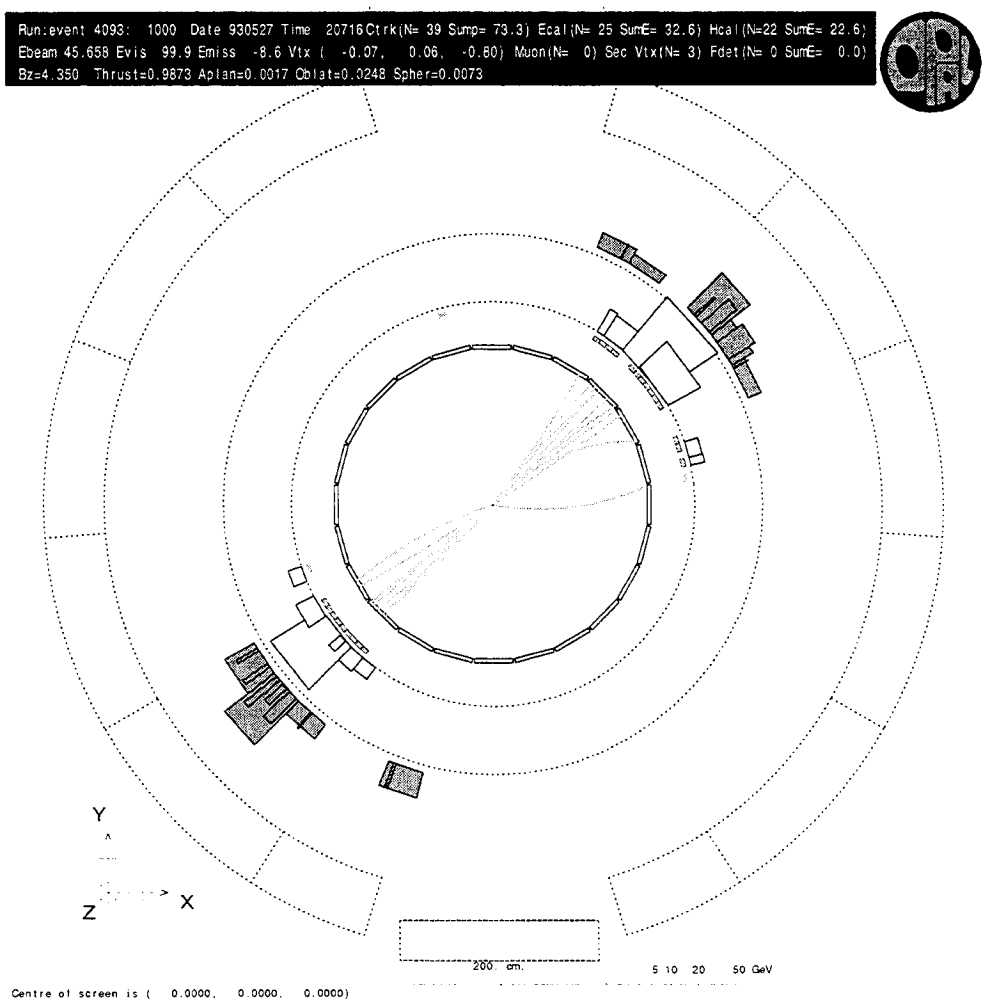

Figure 3.5: Reconstruction of hadronic Z^0 decay in OPAL. The OPAL event display software package, GROPE, shows the many reconstructed tracks (light grey curved lines) and calorimeter hits (dark grey blocks are hadronic calorimeter hits; light grey blocks next to hadronic hits are electromagnetic calorimeter hits) are from a hadronic Z^0 decay. The two collimated high multiplicity "jets" of particles are produced by the fragmentation and hadronization of the high energy quark and anti-quark from a Z^0 decay.

Chapter 4

Data Samples and Monte Carlo Simulation

4.1 Data collected by OPAL

The data used in this analysis were collected at centre of mass energies around the Z^0 resonance from 1993 to 1995. Data from the years before 1993 were not used as OPAL's silicon detector did not have three dimensional hit information before this time; all tracks used in this analysis are required to have silicon hits in both $r-\phi$ and z. Although data were collected at $\sqrt{s} \sim m_{Z^0} \pm 2$ GeV, only data collected at $\sqrt{s} \sim m_{Z^0}$ are used for this analysis. This restriction was imposed because the joint probability distributions used in this analysis vary as a function of centre of mass energy. Table 4.1 shows the year-by-year breakdown of the number of hadronic events used in this analysis. In total, 1,866k hadronic Z^0 decays were used.

A total of five data taking periods from 1993 and 1995 (20 periods in total for 1993 and 1995) were excluded from the analysis as the d_0 resolution for these periods was significantly different from other periods in the same year ($> 3\%$ difference).

Year	Hadronic events (data)	$Z^0 \to b\bar{b}$ events (MC)	$Z^0 \to q\bar{q}$ events (MC)
1993	408k	2,800k*	4,000k*
1994	1,076k	2,800k	4,000k
1995	382k	250k	1,000k
Total	1,866k	3,050k*	5,000k*

Table 4.1: The year-by-year breakdown of data and MC hadronic events used in this analysis. Only events at $\sqrt{s} \sim m_{Z^0}$ with the silicon vertex detector fully operational are used. Several periods of data taking were not used in the analysis because of significant changes in the d_0 resolution. The askerisks on the numbers of MC events emphasize that the simulated data for 1993 and 1994 were virtually the same (see text for more detail).

Consistency checks of the d_0 resolution were performed for all periods of data taking. Excluding problematic periods removes a potential source of bias and systematic uncertainty. In total, these problem periods included 493k hadronic events. The d_0 resolution changed in one period in 1993 because of a high voltage problem in one sector of the jet chamber. A random time jitter problem in all sectors of the jet chamber caused the d_0 resolution to change significantly in two periods in 1995. The cause of the d_0 resolution change for the other two problem periods is not known.

4.2 Simulated data

A total of 8,050k simulated hadronic Z^0 decays were used to generate the reference histograms (probability density functions, PDFs) for all signals and backgrounds considered for this analysis. Of these simulated hadronic Z^0 decays, 3,050k were $Z^0 \to b\bar{b}$ decays. Because of year-to-year changes in the detector, different PDFs were generated for each year of data taking. The year-by-year breakdown of the MC samples is given in table 4.1. The simulated events were first generated by

the JETSET version 7.4 Monte Carlo generator [71] then run through GOPAL, the OPAL detector simulation package [72]. GOPAL provides a description of the OPAL detector to the GEANT [73] software package, which simulates the interactions of the final state particles with the material in the detector. The JETSET event generator will be briefly described in section 4.2.1. The simulated data (JETSET + GOPAL) were processed by the same reconstruction software as was used for the real data. The analysis chain is also the same for the real and simulated data.

Due to a problem with the original detector simulation for 1993, the standard OPAL simulated data (also referred to as the Monte Carlo, MC) for 1993 was not used in this analysis. The original simulation did not properly model the silicon vertex detector, a critical detector for this analysis. Instead, a modified version of the 1994 MC was used to simulate data from 1993; the 1994 MC was modified by ignoring silicon detector hits in a ladder that was not functioning in 1993. As a result of using almost the same simulated data for 1993 and 1994, the statistical uncertainties for the 1993 and 1994 measurements of $Br(b \rightarrow D\bar{D}X)$ are correlated. In particular, the portion of the statistical uncertainty due to the limited statistics of the MC in 1993 is highly correlated to its counterpart for 1994. When the $Br(b \rightarrow D\bar{D}X)$ measurements from the different years are combined, it is assumed that the MC portion of the statistical error is 100% correlated for 1993 and 1994.

The majority of MC studies performed for this analysis were done with simulated data for the 1994 version of OPAL. In these studies, independent sets of MC were used: one set for the pseudo-data and one set for generating MC PDFs. All event, jet and track cut optimization was performed with simulated data. All cuts were frozen after the MC studies and before analyzing the data, to ensure an unbiased result was obtained from the data.

4.2.1 Simulation of hadronic Z^0 decays

The simulation of hadronic Z^0 decays after e^+e^- annihilation is performed by JETSET version 7.4 using Monte Carlo techniques. The simulation of a hadronic Z^0 decay is loosely divided into four different stages in JETSET:

- the initial hard process ($Z^0 \rightarrow q\bar{q}$),
- the ensuing parton showers (e.g. $q \rightarrow gq$),
- the fragmentation/hadronization of the partons (e.g. $q\bar{q} \rightarrow q\bar{q}'q'\bar{q} \Rightarrow q\bar{q}' \rightarrow \pi$), and
- the decays or short-lived particles (e.g. $D^0 \rightarrow K^-\pi^+$).

The four stages of the simulation are shown graphically in figure 4.1.

The first stage of the simulation involves simulating the properties of the initial quark anti-quark pair that is produced when the Z^0 boson decays. This is a "hard" process due to the large amount of energy released. At this stage, the flavour and decay angles of the quarks are determined.

In the second stage of the simulation, the processes $q \rightarrow qg$, $g \rightarrow q\bar{q}$, and $g \rightarrow gg$ are simulated using a leading log approximation of perturbative QCD. Due to the large numbers of quarks and gluons generated, this process is referred to as a parton shower. At this stage, the number of partons, their energies, and their angles with respect to each other are determined. Various "fragmentation" models can also be used at this stage of the simulation to determine the energies of the partons. In $Z^0 \rightarrow c\bar{c}$ and $Z^0 \rightarrow b\bar{b}$ events, the default version of JETSET determines the final energies of the primary c or b quarks from the Peterson *et al.* fragmentation function [74]. For this analysis though, the default energy spectrum of the primary b quarks was weighted so that it follows the Bowler fragmentation model [75]. The

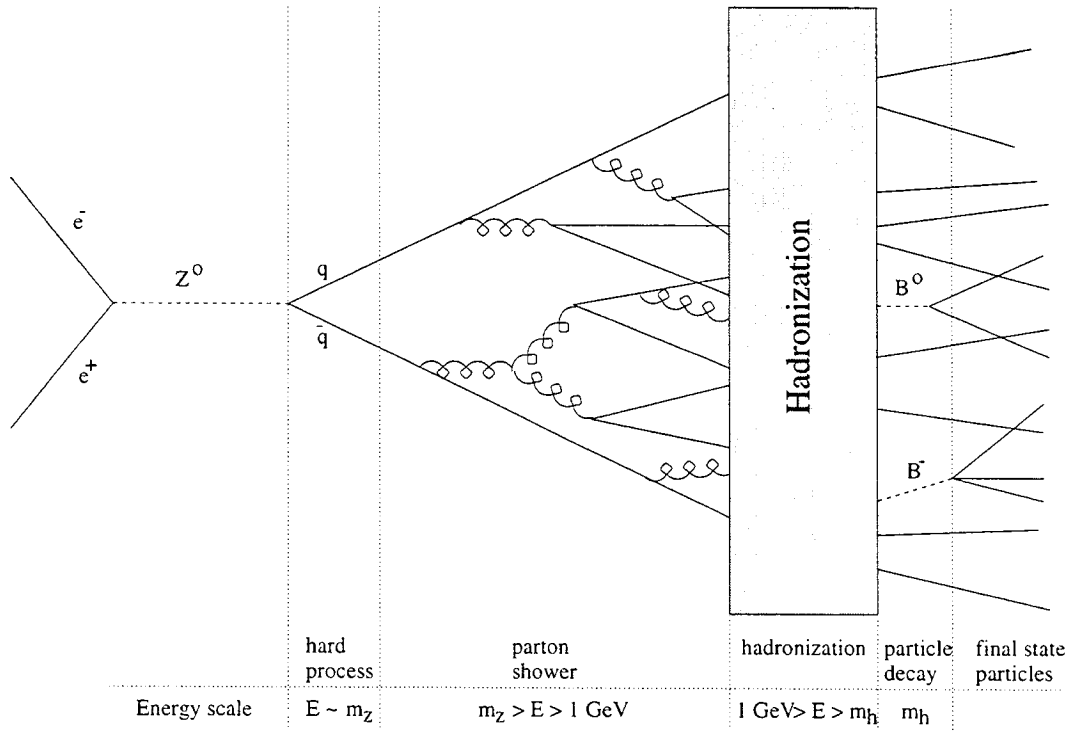

Figure 4.1: Simulation of hadronic Z^0 decay by JETSET. The different stages of the simulation occur at different energy scales, E. There is some overlap between these stages/energy scales. The typical hadron mass is denoted by m_h.

primary b quark energy spectrum was weighted because recent measurements of b quark fragmentation [76–78] show that the data are consistent with the Bowler model but not with the Peterson model.

After the parton shower is simulated, the energy scale at which interactions take place is typically less than 1 GeV. As a result, perturbative QCD no longer applies. Since non-perturbative QCD calculations are not reliable, a model must be used to describe the non-perturbative processes that cause partons to coalesce into hadrons (hadronization). In JETSET, the hadronization model is the Lund string model [79]. In this model, the attractive force between a quark and an anti-quark is represented by a string or tube of colour. As the length of the string between the quarks increases, the potential energy also increases. The quark and anti-quark lose kinetic energy to compensate for the increase in potential energy. As the string lengthens, the probability that a quark anti-quark pair will "pop" out of the vacuum increases. The appearance of a new $q\overline{q}$ pair breaks the original string. This results in there being two quark anti-quark pairs, each attached by its own colour string. This process occurs iteratively until the quark anti-quark pairs form mesons. In addition to a quark anti-quark pair "popping" from the vacuum, an anti di-quark and di-quark pair may also appear. The di-quarks can eventually coalesce with a quark to form a baryon.

The quark flavour content of the hadrons is determined by the flavour of the quarks and anti-quarks that are produced from the strings. Note that because hadronization is a relatively low energy process, the production of charm and beauty quarks is highly suppressed. JETSET determines the other quantum numbers of the hadrons from tabulated probabilities (often experimentally determined) for different combinations of quarks and/or anti-quarks to possess specific spin, orbital angular momentum, total angular momentum and radial quantum numbers.

Many of the hadrons that are generated in the hadronization process are short lived ($\tau < 10^{-11}s$). JETSET simulates the decays of these particles so that by the end of the simulation, only those particles that are relatively long lived remain. These particles are the e, μ, $\pi^{\pm}$, K, p, n, γ and hyperons that are actually observed by particle detectors, plus the ν that are not. To a large extent, the simulation of particle decays relies on tables of experimentally determined exclusive branching ratios and inclusive particle production rates. The exclusive and inclusive results are combined in JETSET so that they are self-consistent. The decays that have not been measured exclusively, are usually simulated using phase-space models. An important feature of JETSET is that the modelling of parton showers and hadronization, and the tables for particle decays are highly tunable. As a result, much effort goes into ensuring that JETSET reproduces the measured hadronic data as closely as possible. The version of JETSET used in this analysis was tuned by members of the OPAL collaboration [80–82].

Chapter 5

Analysis Method

5.1 Joint probability

The main goal of this analysis is to differentiate double charm b decays from single charm b decays. This is achieved by taking advantage of the finite lifetimes of the the D hadrons produced in b decays. The topology of a b decay depends on the number of D hadrons produced in the decay. Figure 5.1 shows the three different topologies of b decays. By taking advantage of these topological differences, this analysis statistically separates the double charm b decays from the dominant single charm b decays. As can be seen in figure 5.1, tracks from double charm B decays tend to originate farther from the interaction point than tracks from single charm B decays. This occurs for two reasons. First, most of the tracks in double charm B decays originate from the two D decay vertices. Second, tracks from D decays originate farther from the interaction point than tracks from b decays.

The separation between a track and the interaction point (IP) can be expressed in terms of its impact parameter, d_0[1], with respect to the IP divided by the uncertainty

[1]See Appendix A, for a definition of the impact parameter.

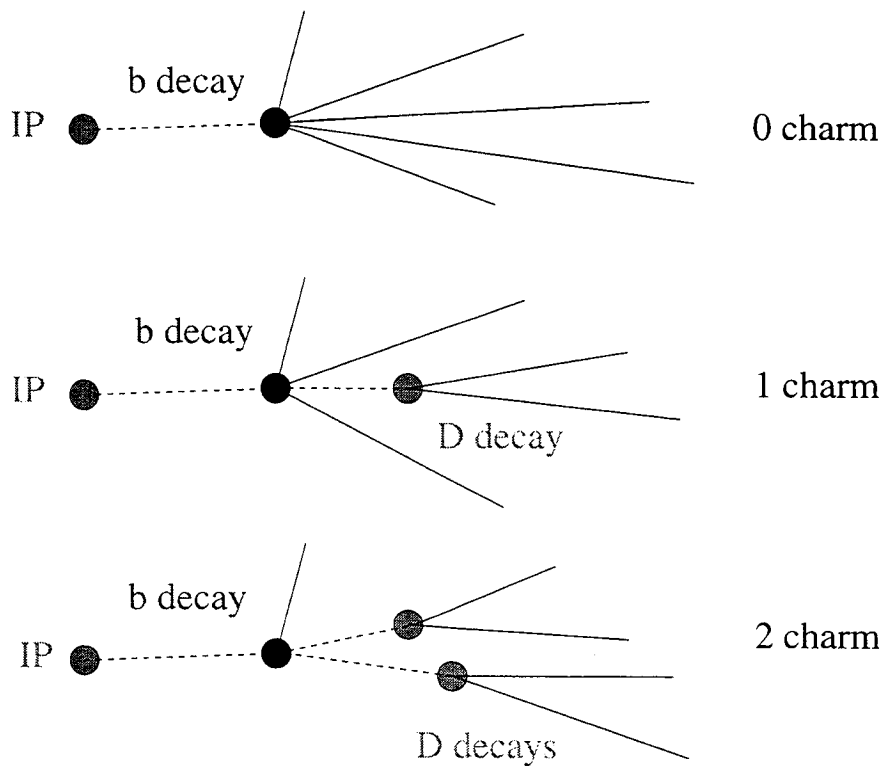

Figure 5.1: Three different topologies of beauty hadron decays. The beauty hadrons travel an average of 3 mm from the interaction point (IP) before decaying. Charmless beauty hadron decays and b $\rightarrow$ charmonium decays are both represented by the upper "0 charm" diagram. These two decay modes have similar topologies because of the prompt electromagnetic or strong decays of charmonium states.

in d_0, σ_{d_0}. This quantity is called the signed impact parameter significance ($S = d_0/\sigma_{d_0}$). The sign of S (and d_0) is determined by the location in the $r-\phi$ plane where the track crosses the axis of the "jet" to which it belongs. In particle physics, a jet is a grouping of relatively collimated particles (see figure 3.5 for an example of a jet). If a line that is drawn in the $r-\phi$ plane from the interaction point to the point where the track intersects the jet axis points in the same direction as the jet momentum vector then d_0 and S are positive. If this line and the jet point in opposite directions then d_0 and S are negative. In figure 5.1, the tracks at each B decay point have $S > 0$ (assuming the jet points from the IP to the B decay point). Most tracks from b and D decays have $S > 0$. In addition, tracks from double charm b decays tend to have larger S than tracks from single charm b decays.

This analysis uses a single variable derived from the S of tracks in a selected jet: the joint probability, P_j (only tracks with $S > 0$ are selected as they are the tracks that are most likely to have originated at b and D decay points). The joint probability is calculated by first considering the S of each selected track in a jet. Under the hypothesis that each track originated at the interaction point (approximated by the primary vertex), one can calculate the conditional probability, p_i, for a track with $S > 0$ to have its measured S or larger. This probability is calculated by comparing the measured S ($S_{meas.}$) to the S resolution function, $f(S)$, for the OPAL detector:

$$p_i = \frac{\int_{S_{meas.}}^{S_{cut}} f(S)dS}{\int_0^{S_{cut}} f(S)dS}. \tag{5.1}$$

S_{cut} (= 25) is a cutoff in S beyond which tracks are not considered. For a pictorial representation of equation 5.1 see figure 5.2. The S resolution function for OPAL is determined using tracks with $S < 0$. Details of the determination of $f(S)$ are given in section 5.2. Given an ensemble of tracks that do originate from the interaction

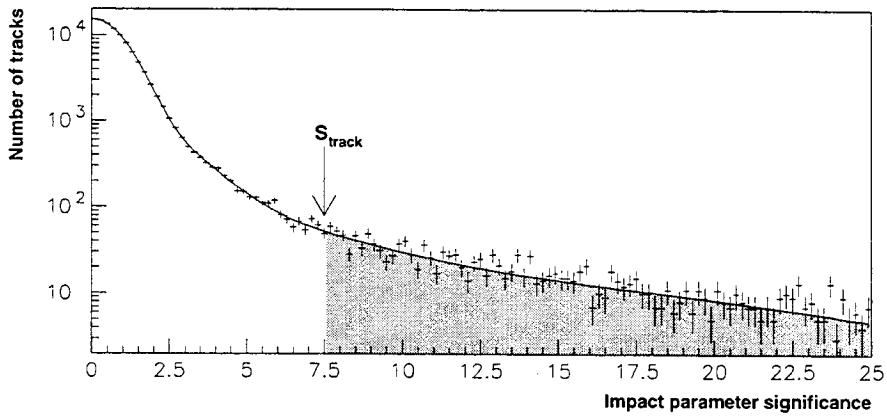

Figure 5.2: Calculation of track p_i. The probability, p_i, for a track originating from the primary vertex with $S > 0$ to have its measured S or larger equals the area under the fitted curve (resolution function) from S_{track} (= $S_{meas.}$) to 25 (= S_{cut}) divided by the total area under the fitted curve from 0 to 25.

point, the distribution of p_i will be uniform from 0 to 1.

The p_i of all the tracks in an ensemble can be combined into a single probability called the joint probability. The joint probability, P_j, is calculated using

$$P_j = y \sum_{m=0}^{N-1} \frac{(-\ln(y))^m}{m!}, \tag{5.2}$$

where y is the product of the N individual track probabilities, p_i [83]. P_j is the probability that the product of N random numbers uniformly distributed from 0 to 1 is y or smaller. The larger the S of tracks in a jet, the smaller the p_i and subsequently P_j will be.

5.2 S resolution function determination

The S resolution function, $f(S)$, for OPAL is determined using tracks with $S < 0$ (backward tracks) in a heavy flavour suppressed data sample. Backward tracks are used as it is assumed that these tracks originated from the interaction point. Tracks originating from locations other than the interaction point (*e.g.* tracks from the charged decay products of long lived particles) tend to have positive S (forward tracks). For each year of data taking, an analytic form for the S resolution function is determined by fitting an appropriate function to the S distribution of backward tracks from hadronic Z^0 decays in the data. The same event and track selection cuts are applied to select backward tracks for $f(S)$ and forward tracks for P_j (except by definition, $S < 0$ for backward tracks and $S > 0$ for forward tracks). This ensures that the tracks used to determine $f(S)$ have similar properties to the tracks used in the Br(b $\rightarrow$ D$\bar{\text{D}}$X) analysis. A cut is also employed on the opposite jet to reduce the fraction of tracks from b and c quark jets[2]; this reduces the fraction of backward tracks that originate from points other than the interaction point.

For each year of data taking, three different S resolution functions are determined. The different resolution functions apply to tracks in three different momentum bins: $p < 1.5$ GeV/c, 1.5 GeV/$c < p < 4.0$ GeV/c, and $p > 4.0$ GeV/c. There are approximately the same number of tracks in each momentum bin. The p distribution of selected tracks is slightly harder in the MC than in the data; this is most likely due to higher neutral particle multiplicities in the data. Since the S resolution is dependent on track momentum, the tuning of the MC d_0 resolution and σ_{d_0} distribution was performed separately for the three aforementioned p bins.

The standard OPAL b physics software contains a routine for calculating the

[2]See section 5.5.2 for a short description of b jet identification/tagging.

joint probability of an ensemble of tracks. The default S resolution functions used in this routine, BTJPRB, were significantly modified to meet the demands of this analysis. The differences are summarized in table 5.1 with details in the following paragraphs.

	This analysis	Default BTJPRB
anti-b/c cut	yes	no
track classes	SI-$r\phi$=SI-z=2	SI-z=1 or 2
$f(S)$	3 gaussians + 1 exponential	1 gaussian + 3 exponentials
p dependence	yes	no

Table 5.1: Summary of differences between S resolution functions used in this analysis and default resolution functions used in BTJPRB. SI-$r\phi$ and SI-z refer to the number of hits in the different layers of the silicon vertex detector.

The first difference between the resolution functions used for this analysis and the default resolution functions is that not all backward tracks in hadronic events are used for this analysis. After an event is forced to have two jets by the Durham jet finding algorithm [84–87], a b quark tagging algorithm [88, 89] is applied to each jet. Backward tracks from a jet are used to determine $f(S)$ only if the b likelihood variable for the opposite jet is less than 0.1. Monte Carlo studies show that this cut increases the purity of backward tracks from the interaction point from 85.6% to 92.5%. Table 5.2 shows the composition of the non-fragmentation tracks with and without the anti-heavy quark cut. Although employing this cut means fewer tracks are used to determine the resolution functions, a more accurate determination of the S resolution functions is obtained.

The second difference between the default $f(S)$ and this analysis' $f(S)$ is that only tracks with two silicon detector hits in each of $r\phi$ and z are used here. In the

Track origin	Fraction without anti-b/c cut	Fraction with anti-b/c cut
b hadron decay	0.041	0.007
D hadron decay	0.073	0.041
strange hadron decay	0.015	0.014
other	0.014	0.014

Table 5.2: Fraction of non-fragmentation backward tracks passing track selection cuts with and without anti-heavy flavour tag on opposite jet. Tracks whose origin is classified as "other" are mostly from interactions with the detector material.

default version of BTJPRB, tracks with SI-z=1 or SI-z=2 are used. The S distributions of backward tracks in the MC and the data were compared and significant discrepancies were identified when the tracks were classified by the number of SI-z hits.

Dividing the backward tracks into more classes based on the number of SI-z and SI-$r\phi$ hits showed that the largest discrepancy between MC and data was for the class of tracks with SI-$r\phi$=2 and SI-z=1. It is likely that many tracks in this class have one misassociated SI-$r\phi$ hit. A misassociated SI-$r\phi$ hit tends to pull the measured S far from its true S. This misassociation is likely not well modelled. Details of SI hit association can be found in reference [67]. In the data, this class represents 1.6% of tracks with at least one hit in each of SI-z and SI-$r\phi$. Approximately 50.3% of all tracks in the data that pass preliminary quality cuts (listed in table 5.3) have at least one hit in each of SI-z and SI-$r\phi$. To improve agreement between the MC and the data, and to reduce the systematic uncertainty associated with the modelling of d_0 and σ_{d_0}, this class of tracks was not used in the analysis. Neglecting 1.6% of tracks with SI information does not significantly affect the statistical precision of the measurement but does significantly reduce the systematic uncertainty.

Even after re-tuning the MC, there was also a significant discrepancy between

Track variable	cut
$\|d_0\|$ w.r.t. beamspot	<5 cm
$\|z_0\|$ w.r.t. beamspot	<200 cm
jet chamber hits	$\geq$20
$\chi^2_{reduced}$ $r-\phi$ track fit	<100
$\chi^2_{reduced}$ z track fit	<100
momentum	<65.0 GeV/c
transverse momentum	$\geq$0.15 GeV/c

Table 5.3: Definition of "quality" tracks. Tracks must satisfy these cuts to be accepted.

the d_0 distributions of tracks with SI-$r\phi$=SI-z=1 in the data and the MC. In order to reduce the systematic uncertainty due to d_0 modelling, these tracks also are not used in the analysis. The remaining SI-$r\phi$=SI-z=2 tracks make up 38.2% of all quality tracks in hadronic data events. Besides having the best d_0 agreement between data and MC, SI-$r\phi$=SI-z=2 tracks also have the best d_0 resolution so have the most discriminating power for the analysis.

The third significant difference between the $f(S)$ used for this analysis and the default $f(S)$ from BTJPRB is the parameterization of the functions. This analysis fits the S distribution of backward tracks with a function of the form

$$f(S) = P_1 e^{\frac{-S^2}{2P_2^2}} + P_3 e^{\frac{-S^2}{2P_4^2}} + P_5 e^{\frac{-S^2}{2P_6^2}} + P_7 e^{\frac{-S}{P_8}}. \tag{5.3}$$

The default BTJPRB $f(S)$ consist of one gaussian centered at zero and three exponential decays. This analysis' parameterization of $f(S)$ gives an improved χ^2 per degree of freedom over the range $0 \leq S \leq 25$. Tracks with S larger than 25 are not used in this analysis as they are very unlikely to have originated at the decay point of a b hadron or a daughter D hadron. The Monte Carlo S distributions for forward tracks originating at b and D decay points are shown in figure 5.3.

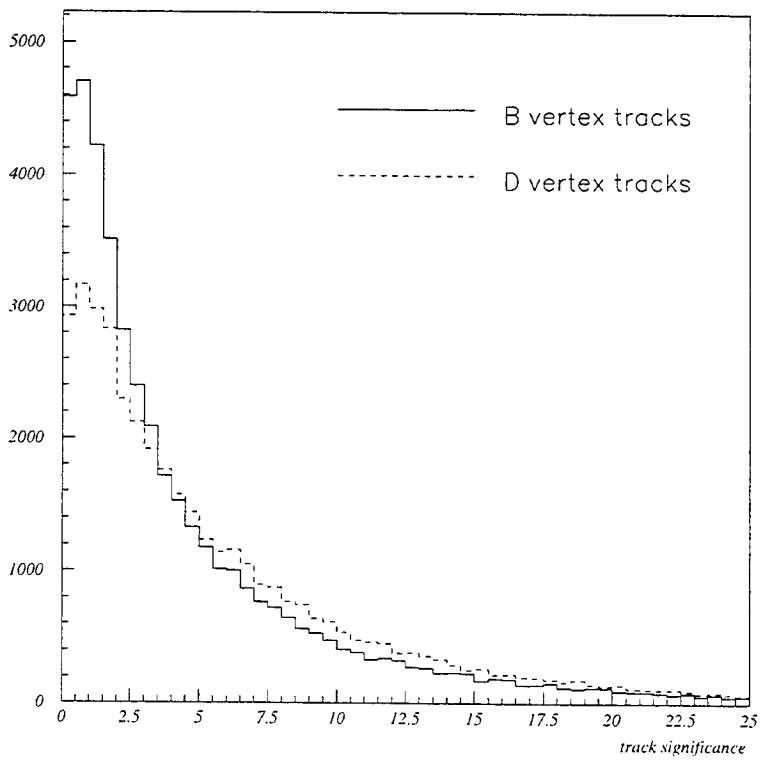

Figure 5.3: S distributions from $Z^0 \rightarrow b\bar{b}$ Monte Carlo for SI-$r\phi$=SI-z=2 tracks originating at decay points of b and daughter D hadrons.

5.3 Tuning of d_0 and σ_{d_0}

The default version of the MC has d_0 and σ_{d_0} distributions for SI-$r\phi$=SI-z=2 backward tracks that are significantly different from the d_0 and σ_{d_0} distributions in the data. This difference is shown in figure 5.4. The MC d_0 and σ_{d_0} distributions were re-tuned to improve the agreement between the MC and the data. The re-tuning for d_0 was done by scaling the difference between the measured and true track parameters on a track-by-track basis. For a detailed discussion about track parameter tuning at OPAL see reference [90]. The amount of re-scaling depended on the track momentum and the year of data taking.

Three different methods were used to determine the best d_0 scaling factors. The first method (method A) determined the d_0 factor that minimized the χ^2 calculated by comparing the normalized d_0 distributions of selected backward tracks in the data and the MC. The χ^2 were calculated over wide ranges of d_0. For the different years and momentum bins, tuning the MC d_0 resolution reduced the χ^2 by amounts varying from approximately 3 (for the middle p bin in 1995) to 100 (for the middle p bin in 1994). Table 5.4 shows the best d_0 scale factors determined by method A. The improved agreement between the data and the MC for SI-$r\phi$=SI-z=2 tracks is shown in figure 5.5. The residual (pull) distributions and data/MC distributions for $|d_0|$ of backward tracks are shown in figure 5.6 for untuned MC and in figure 5.7 for tuned MC.

In addition to tuning d_0 over a wide range, the "cores" of the d_0 distributions for backward tracks were studied (method B). First, the d_0 distributions of backward tracks in the data and the MC were fit by two gaussians centered on $d_0 = 0$. The d_0 scale factors for the MC were then varied to determine what scale factors yielded the best agreement between the widths of the narrow (core) gaussians in the data

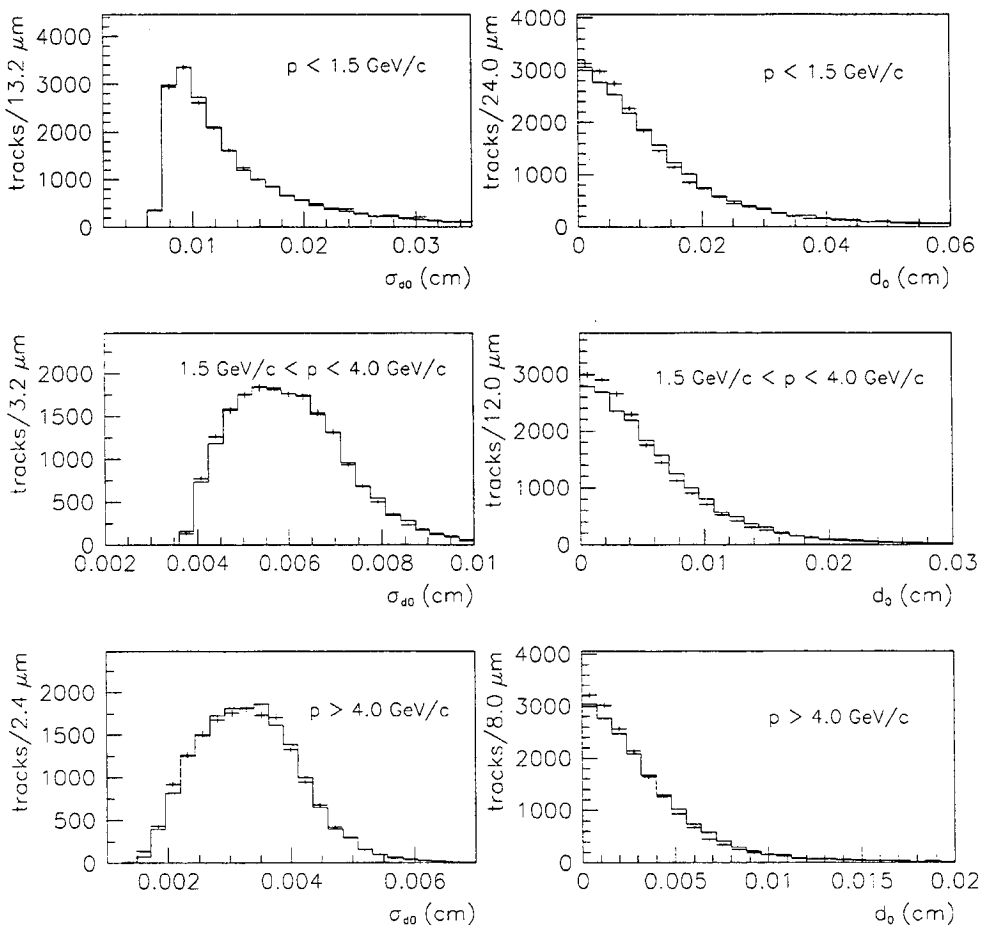

Figure 5.4: Comparison of $|d_0|$ and σ_{d_0} distributions of SI-$r\phi$=SI-z=2 backward tracks for *default* MC (histograms) and data (data points with error bars) from 1994. The difference between the data and the MC is more apparent in the d_0 distributions.

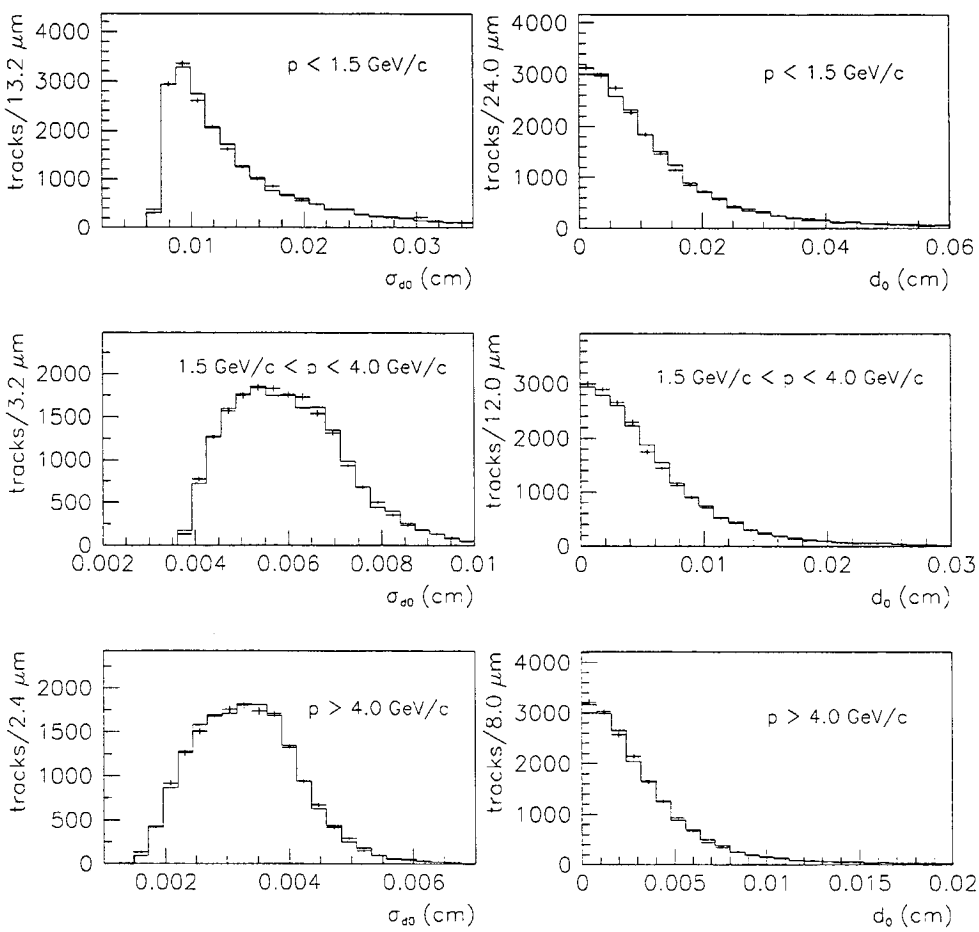

Figure 5.5: Comparison of $|d_0|$ and σ_{d_0} distributions of SI-$r\phi$=SI-z=2 backward tracks for 1994 *tuned* MC (histograms) and data (data points with error bars). The MC $|d_0|$ and σ_{d_0} distributions were tuned by method A.

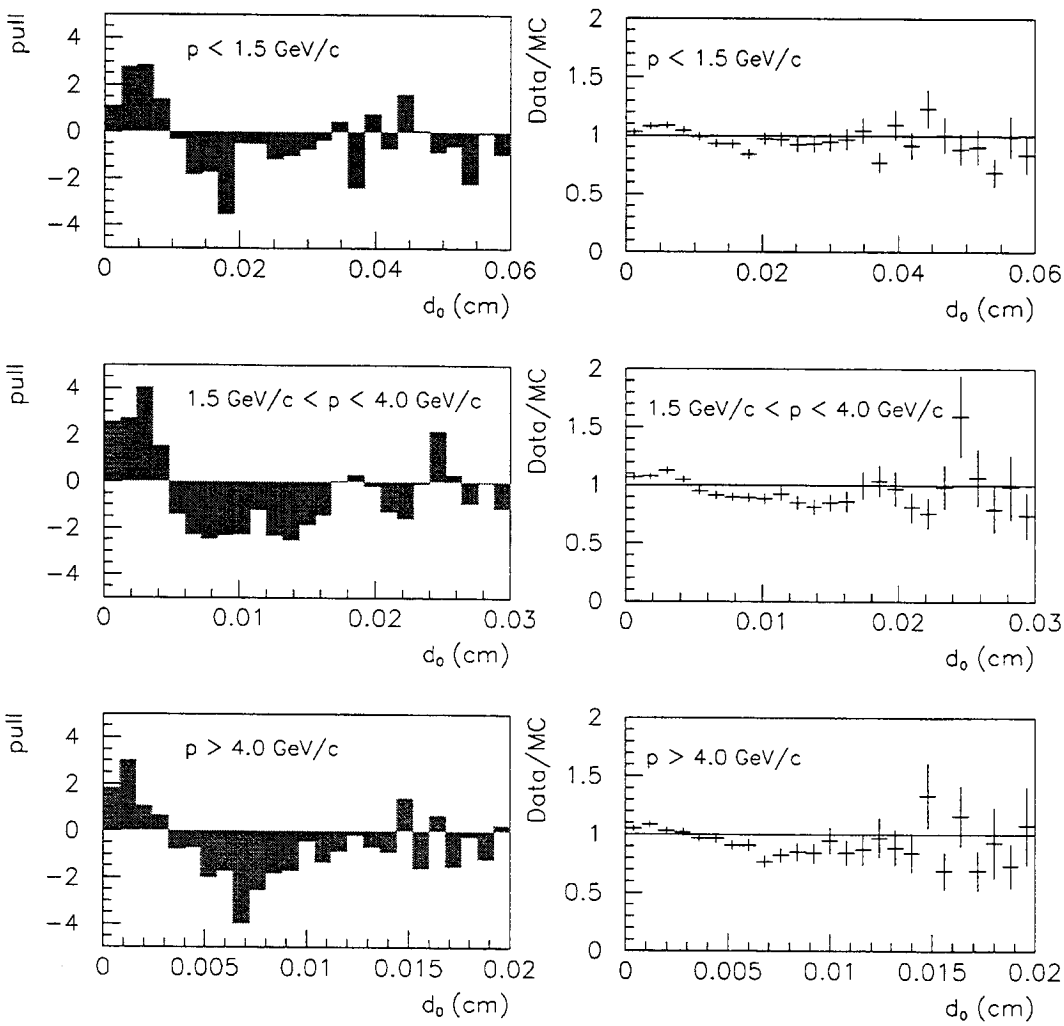

Figure 5.6: Pull distributions and data/MC ratios for $|d_0|$ of backward tracks from 1994. Tracks from data are compared to tracks from default MC.

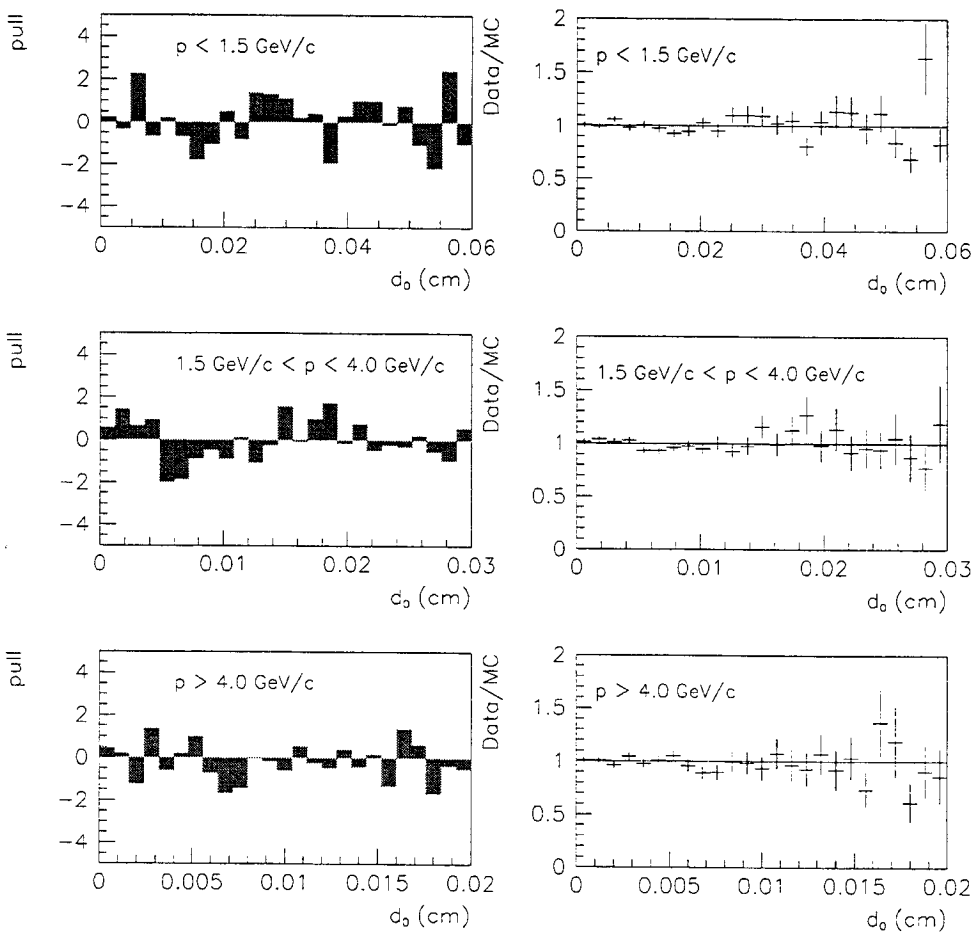

Figure 5.7: Pull distributions and data/MC ratios for $|d_0|$ of backward tracks from 1994. Tracks from data are compared to tracks from tuned MC.

Year	p bin (GeV/c)	d_0 Scale Factor	σ_{d_0} Scale Factor
1993	$p < 1.5$	0.965	1.007
1993	$1.5 < p < 4.0$	0.972	1.005
1993	$p > 4.0$	0.934	1.011
1994	$p < 1.5$	0.933	1.002
1994	$1.5 < p < 4.0$	0.916	0.999
1994	$p > 4.0$	0.927	0.996
1995	$p < 1.5$	0.985	1.005
1995	$1.5 < p < 4.0$	0.991	1.001
1995	$p > 4.0$	1.022	1.005

Table 5.4: Best d_0 and σ_{d_0} scale factors for single SI-$r\phi$=SI-z=2 backwards tracks over wide range of d_0 and σ_{d_0}. d_0 scale factors less than 1.0 imply that the d_0 resolution in the default MC is worse than the resolution in the data. σ_{d_0} scale factors smaller than 1.0 imply that the impact parameter uncertainties were overestimated in the MC.

and the MC. For each year of data taking and each momentum bin, the best d_0 scale factor was between 0 and 0.030 smaller than the best d_0 scale factors determined from method A.

Finally, the d_0 tuning was studied in a third way (method C). To study the effect of possible correlations in the significance of tracks in the same jet, a collective property of tracks from the same jet was studied. This property was $-\ln(P_j)$ for backwards tracks in the same jet. For both the data and the MC, "backwards" $-\ln(P_j)$ distributions were generated using the S resolution functions from the data. Again, the d_0 scale factors were varied to determine which scale factors gave the best agreement between the data and the MC for the backwards $-\ln(P_j)$ distributions. As with method B, the best d_0 scale factors were between 0 and 0.030 smaller than those determined by method A.

In order to obtain a conservative estimate of the systematic uncertainty due to modelling d_0, the central values for the d_0 scale factors were chosen to be 0.015

smaller than those shown in table 5.4 (method A). The d_0 scale factors were then varied by ± 0.015 to determine the systematic uncertainty in $\mathrm{Br}(\mathrm{b} \to \mathrm{D}\bar{\mathrm{D}}\mathrm{X})$. This variation in the scale factors is much larger than the statistical uncertainties of the estimates of the best d_0 scale factors obtained by the three different methods (approximately ± 0.002).

The re-tuning of σ_{d_0} was achieved by scaling the default σ_{d_0} values by a constant (different constant for each year of data taking and each track momentum bin). The magnitude of re-tuning required to maximize the agreement between the MC and the data for σ_{d_0} was significantly less than the re-tuning required for d_0. Nevertheless, it is very important that σ_{d_0} is modelled correctly as it is the denominator that determines S for tracks. The σ_{d_0} scale factors adopted for this analysis are shown in table 5.4. Examples of the σ_{d_0} distributions in the default and re-tuned MC and the data are shown in figures 5.4 and 5.5 respectively. The pull distributions and data/MC distributions for σ_{d_0} of backward tracks are shown in figure 5.8 for the default MC and in figure 5.9 for the re-tuned MC. The χ^2 values that were calculated to determine the best σ_{d_0} scale factors changed significantly with small changes in the scale factors ($2 < \Delta(\chi^2) < 15$ for 0.001 change in scale factors). The smallest χ^2/d.o.f. values from comparing the MC and the data σ_{d_0} distributions varied from 45/25 to 115/25 however. For this reason, a variation of ± 0.005 ($= \pm 0.001 \times 115/25$) for the σ_{d_0} scale factors was adopted for determining the associated systematic uncertainties. Examples of the impact parameter significance distributions after tuning d_0 and σ_{d_0} are shown in figure 5.10.

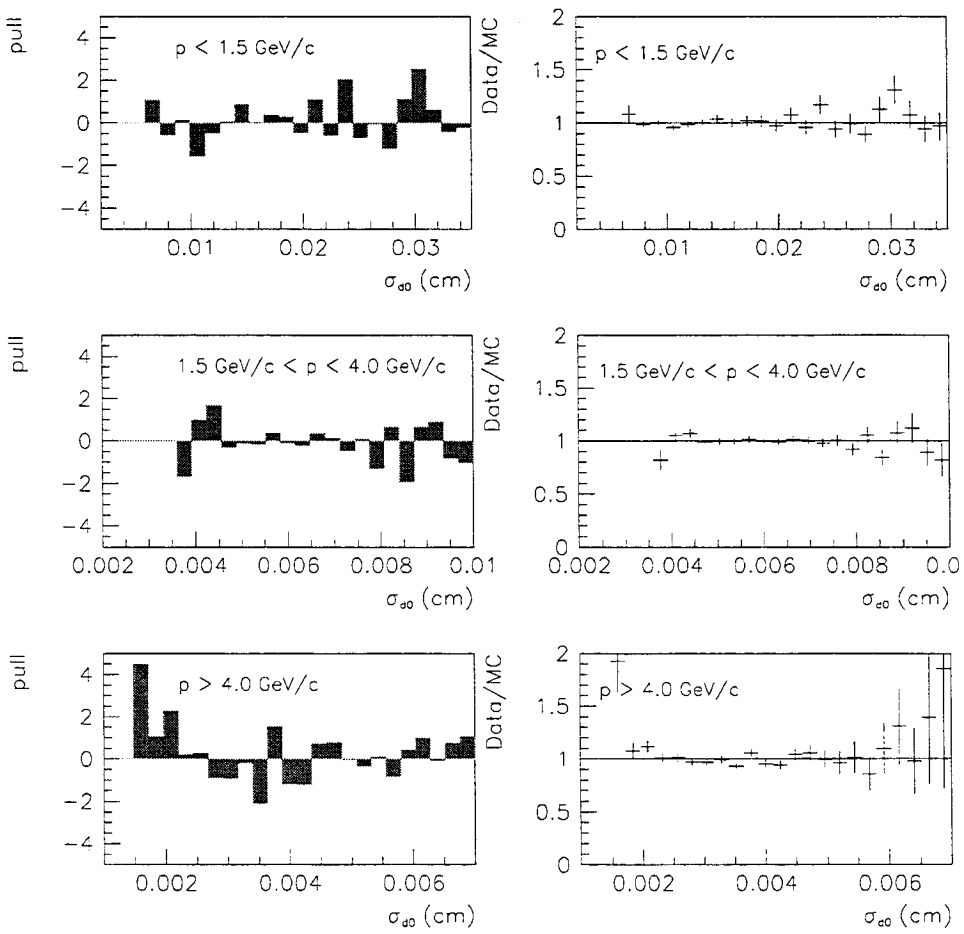

Figure 5.8: Pull distributions and data/MC ratios for σ_{d_0} of backward tracks from 1994. Tracks from data are compared to tracks from default MC.

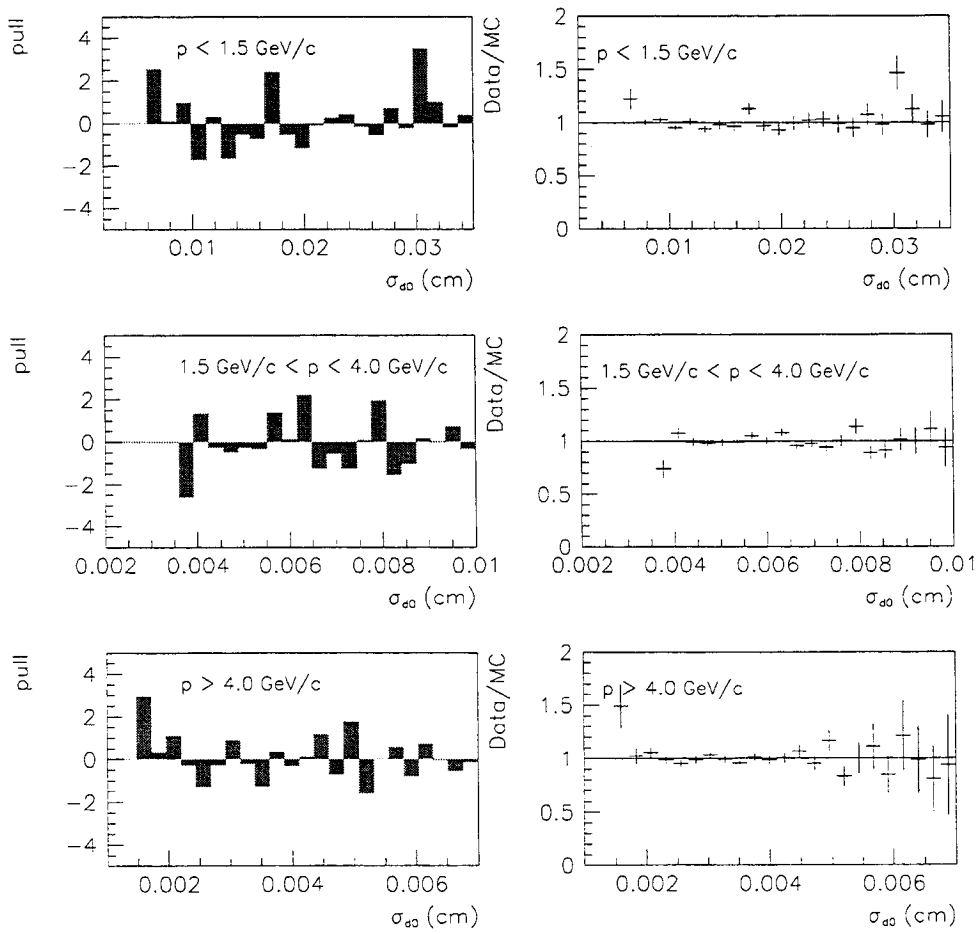

Figure 5.9: Pull distributions and data/MC ratios for σ_{d_0} of backward tracks from 1994. Tracks from data are compared to tracks from tuned MC. The MC $|d_0|$ and σ_{d_0} distributions were tuned by method A.

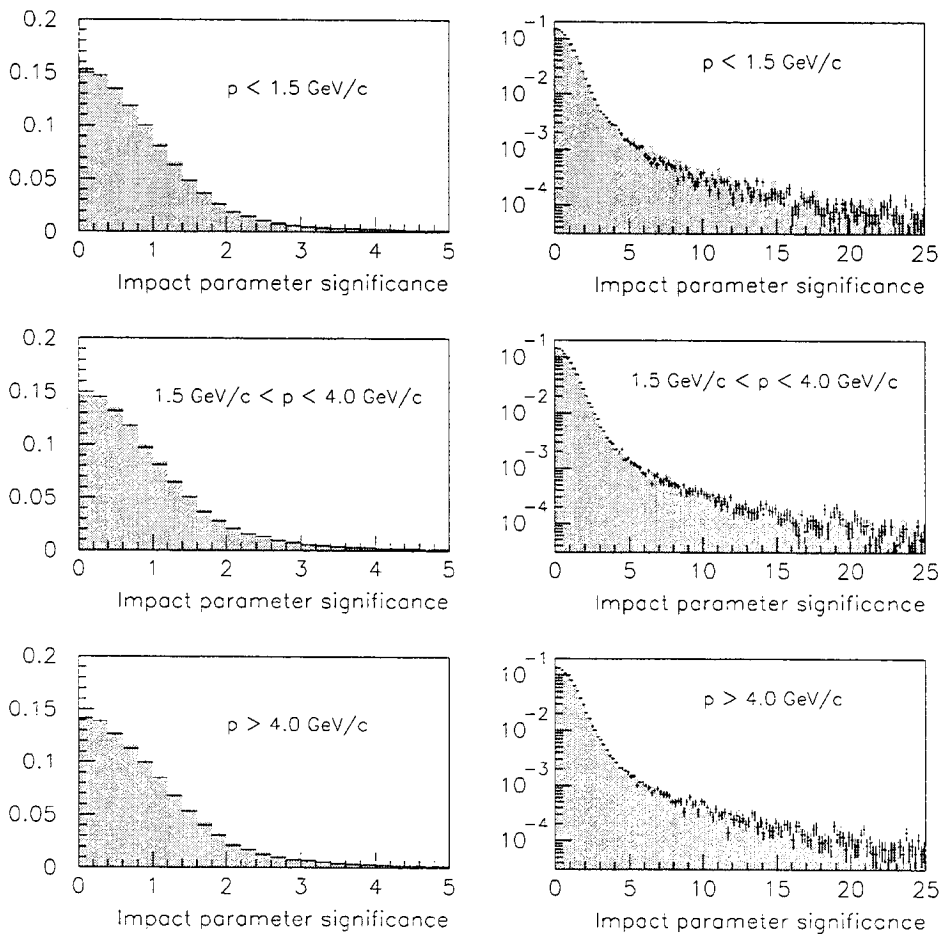

Figure 5.10: Impact parameter significance distributions for SI-$r\phi$=SI-z=2 backward tracks. The histograms are from the 1994 MC and the data points with error bars are from the 1994 data. The plots on the left of the figure show the agreement between the MC and the data for tracks at low impact parameter significance. The plots on the right of the figure show the agreement for tracks at high impact parameter significance. The MC $|d_0|$ and σ_{d_0} distributions shown here were tuned by method A.

5.4 Fitting procedure

The fraction of double charm b decays in data is determined by comparing the $-\ln(P_j)$ PDFs for the different signals and backgrounds from the MC to the -ln(P_j) distributions of the data. The -ln(P_j) distributions for the different signals and backgrounds are shown in figures 5.11 and 5.12 respectively. A χ^2 fit is performed to estimate the best fit values of the free parameters and their associated statistical uncertainties. The MINUIT package [91] is used to minimize the χ^2 function. The fitting function used is

$$\begin{aligned} F(x) = \; & N(1+\alpha x)\Big[\{1 - f_{uds} - f_c - f_g\} \times \\ & \Big\{\mathrm{Br}_{0c}G^{0c}(x) + \mathrm{Br}_{1c}G^{1c}(x) + \\ & \mathrm{Br}_{2c}G^{2c}(x) + \mathrm{Br}_{charmonium}G^{charmonium}(x)\Big\} + \\ & \Big\{f_{uds}G^{uds}(x) + f_cG^c(x) + f_gG^g(x)\Big\}\Big] \end{aligned} \tag{5.4}$$

where $x = -\ln(P_j)$ and N is a normalization factor chosen so that $\int F(x)dx$ is equal to the number of events in the data. The different $G^i(x)$ are the normalized PDFs for the different signals and backgrounds. Br_{1c} is the b $\rightarrow$ single charm branching ratio; Br_{2c} is the double charm branching ratio; Br_{0c} is the charmless branching ratio; $\mathrm{Br}_{charmonium}$ is the (b$\rightarrow$ charmonium) branching ratio. The background fractions are f_c, the fraction of charm jet background in data, f_{uds}, the fraction of light quark jet background, and f_g, the fraction of data made up of gluon jets in $\mathrm{Z}^0 \rightarrow b\bar{b}$ events. Finally, α is a term used to parameterize mis-modelling due to incomplete knowledge of all physics inputs (*e.g.* mean multiplicity of charged particles from fragmentation). The α term is described in more detail below. Only Br_{2c} and α are

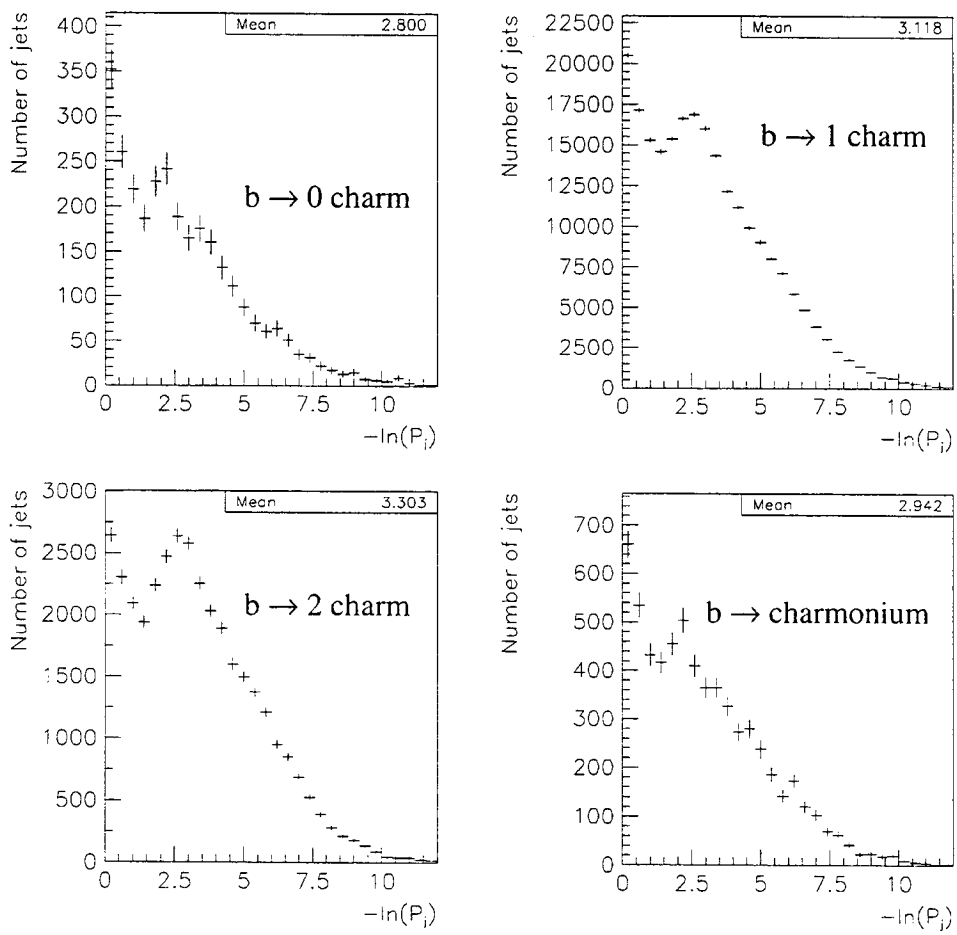

Figure 5.11: Signal (b hadron decay) $-\ln(P_j)$ distributions from 1994 MC for jets with two tracks contributing to $-\ln(P_j)$.

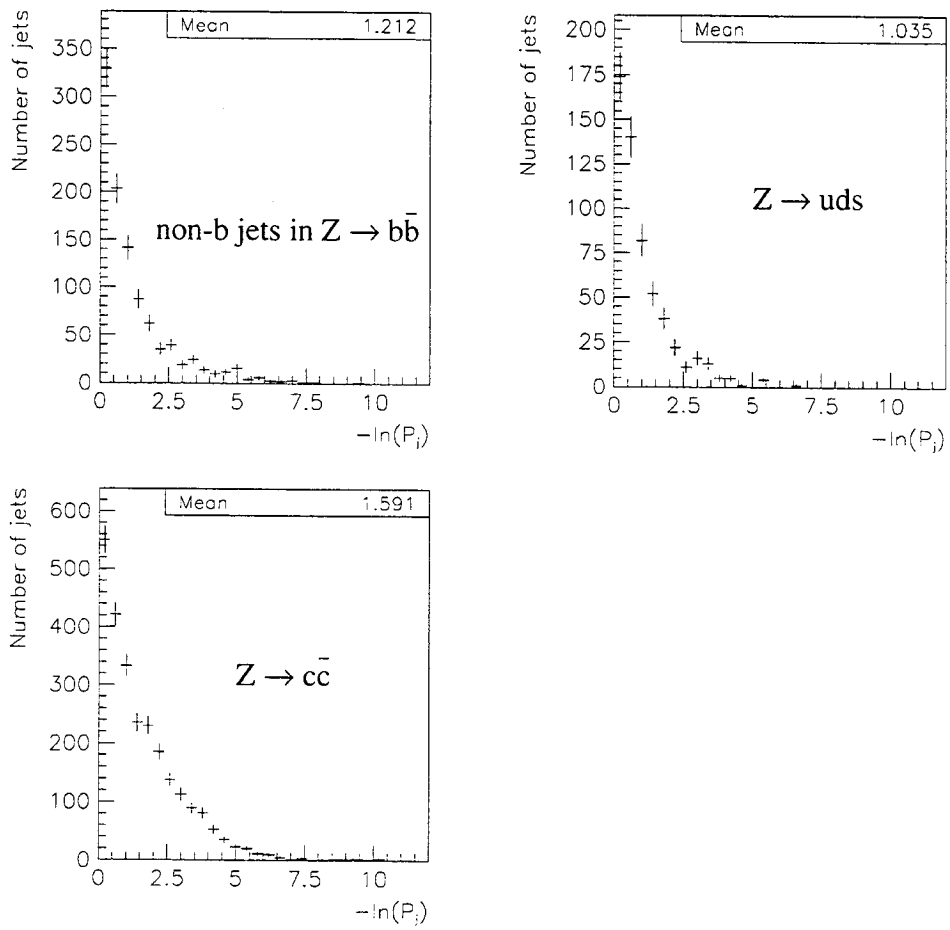

Figure 5.12: Background (no b hadron decay) $-\ln(P_j)$ distributions from 1994 MC for jets with two tracks contributing to $-\ln(P_j)$.

free parameters in the fit. Br_{1c} is constrained by

$$Br_{1c} = 1 - Br_{2c} - Br_{0c} - Br_{charmonium}, \tag{5.5}$$

while Br_{0c} and $Br_{charmonium}$ are fixed to the world average values listed in [23]. A constraint is also imposed on the α term; if the modelling of all physics inputs was perfect then α would equal zero. As the degree of mis-modelling is not large, α is constrained to be close to zero. This constraint is achieved by including an extra term in the evaluation of the χ^2 so that

$$\chi^2_{mod.} = \chi^2 + \frac{\alpha^2}{\sigma^2_\alpha}. \tag{5.6}$$

The value of σ_α is discussed in the following section.

α parameter

MC studies show that changing the input values for the mean multiplicity of charged particles from fragmentation ($< N_{ch} >_{frag}$), b lifetimes (τ_b) or a variety of other physics inputs results in a change to the $-\ln(P_j)$ distributions that can be corrected to first order by the inclusion of the α term in equation 5.4. Figure 5.13 shows an example of this behaviour. Allowing α to assume non-zero values in the fit partially corrects for the mis-modelling of some physics inputs; the α term also accounts for correlations between mis-modelled physics inputs (*e.g.* if the effect of mis-modelling τ_b partially cancels the effect of mis-modelling $< N_{ch} >_{frag}$). In principle, the best fit value for α contains information about $< N_{ch} >_{frag}$, b lifetimes and any other physics inputs that result in an approximately linear change in the -ln(P_J) distributions. As a result, α could be used to measure these values. In practice

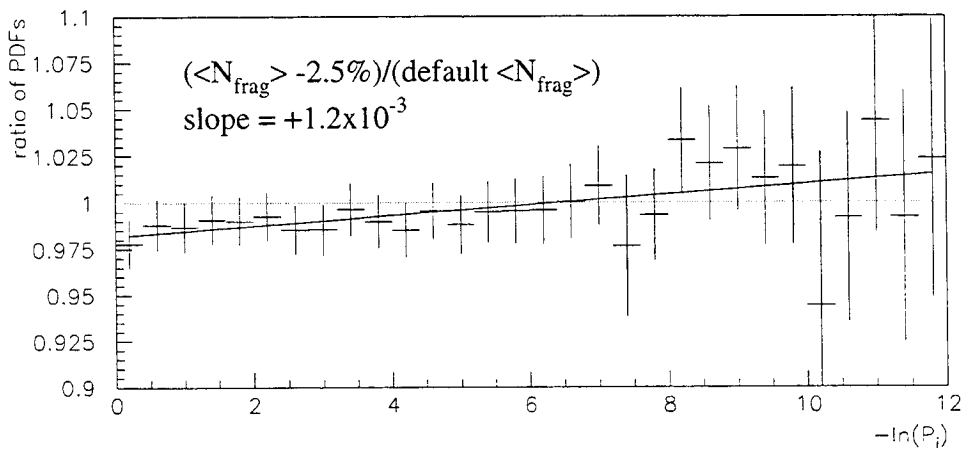

Figure 5.13: Comparison of $-\ln(P_j)$ distributions with different mean charged particle multiplicities from fragmentation, $< N_{ch} >_{frag}$. In this plot, the $-\ln(P_j)$ distribution for single charm b decays with four tracks contributing to $-\ln(P_j)$, and with $< N_{ch} >_{frag}= 12.14$ is divided by the same $-\ln(P_j)$ distribution with $< N_{ch} >_{frag}= 12.46$. The resulting histogram demonstrates how an approximately linear change in $-\ln(P_j)$ occurs when $< N_{ch} >_{frag}$ is varied. The α parameter used in the fitting function (equation 5.4) partially corrects mis-modelling of this nature.

though, it is difficult to measure any one of these inputs in isolation while properly accounting for the influence of the other variables. MC studies showed that inclusion of the α parameter in the fit increased the statistical uncertainty of the measurement but reduced the total uncertainty by reducing the systematic uncertainty.

MC studies were performed to determine the value of σ_α in equation 5.6 that results in the smallest predicted total uncertainty for Br(b $\rightarrow$ D$\bar{\text{D}}$X). It was found that although the statistical and systematic uncertainties did change appreciably as σ_α was varied, the total uncertainty for Br(b $\rightarrow$ D$\bar{\text{D}}$X) was not very sensitive to the value of σ_α. The value adopted for σ_α was 3×10^{-3}. MC studies also showed that α changed by $\sim 3 \times 10^{-3}$ when the source of the largest systematic uncertainty, $< N_{ch} >_{frag}$, is varied by its measured uncertainty. This reinforces the choice of $\sigma_\alpha = 3 \times 10^{-3}$.

Binning of Data and PDFs by track multiplicity

The comparison of MC and data -ln(P_j) distributions is performed with jets containing the same number of tracks contributing to -ln(P_j). The data are binned by track multiplicity to improve the sensitivity of the analysis and to reduce uncertainties due to incorrect modelling of the number of tracks contributing to -ln(P_j). The PDFs were divided into six track multiplicity bins: one bin for each track multiplicity one through five and one bin for track multiplicities ≥ 6. Separate "signal" PDFs were generated for each track multiplicity bin for b hadrons decaying to final states containing no charm quarks, one charmed hadron, two charmed hadrons, and charmonium states. "Background" PDFs were generated for light quark jets (u, d or s) from Z $\rightarrow u\bar{u}(d\bar{d}, s\bar{s})$ decays, charm jets in Z $\rightarrow c\bar{c}$ events, and non-b jets in Z $\rightarrow b\bar{b}$ events (*i.e.* jets from hard gluons). The fractions of the different signals and backgrounds vary as a function of track multiplicity. The fraction of each background

and fixed signal in each multiplicity bin is determined from the MC.

In order to ensure that the minimum number of expected data entries (based on MC) in each $-\ln(P_j)$ bin is at least 50, the number of bins varies for each track multiplicity. The $-\ln(P_j)$ range over which the fits are performed also varies for each track multiplicity. Jets with $-\ln(P_j)$ greater than the range considered are included in the largest $-\ln(P_j)$ bin. The first several $-\ln(P_j)$ bins of each track multiplicity are also combined into one large bin in order to reduce the analysis' sensitivity to changes in the d_0 resolution. MC studies show that the shapes of the $-\ln(P_j)$ distributions change quite significantly at low $-\ln(P_j)$ when the d_0 resolution is varied. Table 5.5 details the number of $-\ln(P_j)$ bins, ranges of fits, and numbers of bins combined for each track multiplicity. These numbers are the same for each year of data taking. The number of $-\ln(P_j)$ bins used in the fits was varied in a MC study; the branching ratios and statistical uncertainties obtained in fits to MC pseudo-data were not sensitive to the numbers of bins used.

Track multiplicity	$-\ln(P_j)$ fit range	n_{bins}	n_{comb}
1	$0 \rightarrow 6$	25	10
2	$0 \rightarrow 8$	20	5
3	$0 \rightarrow 10$	25	5
4	$0 \rightarrow 10$	25	5
5	$0 \rightarrow 12$	15	5
6+	$0 \rightarrow 12$	10	5

Table 5.5: Details of $-\ln(P_j)$ binning for fits. n_{bins} is the number of bins the fit range is initially divided into. n_{comb} is the number of low $-\ln(P_j)$ bins that are combined in order to reduce the analysis' sensitivity to the modelling of the d_0 resolution.

The data $-\ln(P_j)$ distributions of each track multiplicity bin for a given year are fit by the MC PDFs using a single α parameter. A different Br_{2c_i} is determined

for each track multiplicity bin. At the same time, the total number of b decays for each track multiplicity bin, N_{b_i}, is determined. By combining Br_{2c_i} and N_{b_i}, $\mathrm{Br}(\mathrm{b} \rightarrow \mathrm{D}\bar{\mathrm{D}}\mathrm{X})$ is calculated for each year's data:

$$\mathrm{Br}(\mathrm{b} \rightarrow \mathrm{D}\bar{\mathrm{D}}\mathrm{X}) = \frac{\sum_{i=1}^{6} \mathrm{Br}_{2c_i} N_{b_i}}{\sum_{i=1}^{6} N_{b_i}}. \tag{5.7}$$

The fits are done separately for each year as the S resolution of the detector is different for each year. Consistency checks are also made between years to ensure that the uncertainties have been correctly estimated and no significant biases exist for individual years. Once Br_{2c} is determined for all years of interest, a weighted average for $\mathrm{Br}(\mathrm{b} \rightarrow \mathrm{D}\bar{\mathrm{D}}\mathrm{X})$ is calculated. The final value for $\mathrm{Br}(\mathrm{b} \rightarrow \mathrm{D}\bar{\mathrm{D}}\mathrm{X})$ can then be input into equation 2.12 to determine n_c.

5.4.1 Potential bias in fit

A bias exists in the analysis if the χ^2 for the $-\ln(P_j)$ fit is calculated without including the individual statistical uncertainties of the MC PDFs that make up the fitting function, $F(x)$. This bias was discovered in the course of investigating two different methods for determining the uncertainty in $\mathrm{Br}(\mathrm{b} \rightarrow \mathrm{D}\bar{\mathrm{D}}\mathrm{X})$ due to finite MC statistics.

The first (biased) method involved calculating the χ^2 for the fit of $F(x)$ to the data without including the statistical uncertainty of the MC. In this case

$$\chi^2 = \sum_{i=1}^{n_{bins}} \frac{(N_{i_{data}} - N_{i_{MC}})^2}{N_{i_{MC}}}, \tag{5.8}$$

where $N_{i_{data}}$ is the number of data entries in $-\ln(P_j)$ bin i, $N_{i_{MC}}$ is the number of MC events (determined by $F(x)$) in bin i, and n_{bins} is the total number of bins used in the

fit. In this method, the uncertainty due to finite MC statistics is determined by first randomly fluctuating the bin contents of the MC PDFs by their Poisson uncertainties and redoing the fit to determine Br(b $\rightarrow$ D$\bar{\text{D}}$X) . This process is repeated many times (100+) to generate a distribution of values for Br(b $\rightarrow$ D$\bar{\text{D}}$X). The RMS of this distribution represents the one standard deviation uncertainty due to finite MC statistics.

The second method calculates the χ^2 in such a way that the statistical uncertainty due to finite MC statistics is included in the total statistical uncertainty determined by the fit. Here,

$$\chi^2 = \sum_{i=1}^{n_{bins}} \frac{(N_{i_{data}} - N_{i_{MC}})^2}{N_{i_{MC}} + \sigma^2_{N_{i_{MC}}}}, \tag{5.9}$$

where $\sigma_{N_{i_{MC}}}$ is the combination of the statistical uncertainties of the MC PDFs that make up $F(x)$.

To test for biases in the Br(b $\rightarrow$ D$\bar{\text{D}}$X) estimators for these two methods, a MC study was performed using toy samples of MC and pseudo-data. The pseudo-data were randomly drawn from two gaussians with different means and widths. The two MC PDFs (histograms) used to fit the pseudo-data were generated from gaussian distributions, $g1$ and $g2$, that had the same means and widths as the gaussians in the pseudo-data. Fits of the MC PDFs to the pseudo-data were performed to extract the fractions of $g1$, $\mathcal{F}_{g1}$, and $g2$, $\mathcal{F}_{g2}$, present in the pseudo-data. $\mathcal{F}_{g1}$ was constrained by $\mathcal{F}_{g1} = 1 - \mathcal{F}_{g2}$. The same fitting routine was used for this study and the Br(b $\rightarrow$ D$\bar{\text{D}}$X) analysis.

The relative sizes of the $g1$ and $g2$ MC samples were varied to see what effect they had on the fitted fractions and the statistical uncertainty, $\sigma_{stat.}$. For gaussians that were well separated (e.g. $\mu_1 = 0.0$, $\sigma_1 = 1.0$; $\mu_2 = 1.0$, $\sigma_2 = 1.0$) there was no

bias in the value of $\mathcal{F}_{g2}$ except when method 1 was used with a very large number of bins (3000 bins for 200,000 psuedo-data "events", and 800,000 MC "events") and the relative sizes of the MC samples for $g1$ and $g2$ were quite different ($N_{g1} = 600,000$ and $N_{g2} = 200,000$). In this case, the estimators $\mathcal{F}_{g1}$ and $\mathcal{F}_{g2}$ from the fit were biased towards the fractions of $g1$ (0.75) and $g2$ (0.25) in the MC. Even though there were equal amounts of $g1$ and $g2$ in the pseudo-data, the estimates of $\mathcal{F}_{g1}$ and $\mathcal{F}_{g2}$ were 9σ from the correct values. An even larger bias resulted when method 1 was used to fit pseudo-data consisting of two gaussians whose means were very similar ($\mu_1 = 0.9$, $\mu_2 = 1.0$; $\sigma_1 = 1.0$, $\sigma_2 = 1.0$). Again the values for $\mathcal{F}_{g1}$ and $\mathcal{F}_{g2}$ were biased towards the fractions of $g1$ (0.75) and $g2$ (0.25) in the MC: $\mathcal{F}_{g1} = 0.740 \pm 0.016$ even though the true fraction in the pseudo-data was 0.5. As with the previous example, if the number of entries per bin is reduced, the bias increases.

The bias for the $\mathcal{F}_{g2}$ estimator in method 1 can be understood as arising from the relative "smoothness" of the g_1 and g_2 MC PDFs. The $\mathcal{F}_{g2}$ estimator is biased towards $N_{g2}/(N_{g1}+N_{g2})$ as the smoother distribution tends to contribute less to the χ^2. As the number of entries per bin is decreased, the "smoothness" of the PDFs decreases and the bias increases.

In addition to the problem with bias, method 1 also causes the estimates of statistical and systematic uncertainties to be inaccurate. The statistical uncertainty of $\mathcal{F}_{g2}$ from the fit is underestimated when the number of entries per bin is small or when the MC PDFs are very similar. Studies with the $-\ln(P_j)$ distributions from MC also show that the estimates of the systematic uncertainties are smaller with method 1 than with method 2. This occurs because the Br(b $\rightarrow$ D$\bar{\text{D}}$X) estimator is biased towards the value of Br(b $\rightarrow$ D$\bar{\text{D}}$X) in the MC.

In summary, method 1 leads to an underestimate of the statistical and systematic uncertainties, and a bias in the Br(b $\rightarrow$ D$\bar{\text{D}}$X) estimator. For these reasons, method

2 is adopted for calculating the χ^2 for the fits.

5.5 Event, jet and track selection

The values of event, jet and track selection cuts were determined from Monte Carlo (MC) studies of the effect of different cut values on the total uncertainty of Br($b \rightarrow D\bar{D}X$). No data were used to optimize the cuts. The MC studies did not attempt to calculate the total systematic uncertainty for each possible combination of cuts; this procedure would have taken a prohibitively long time. Instead, what were considered to be the dominant systematic uncertainties and the statistical uncertainty were studied. The quadratic sum of these uncertainties will be referred to as the "expected uncertainty" in this section.

These studies were performed assuming that the different cuts are largely independent (*i.e.* once the minimum total uncertainty was determined as a function of one cut, that cut was no longer varied); exploring the full multi-parameter space would also have taken prohibitively long. However, it is not believed that there should be any large correlations between the different cut variables that would cause this strategy to lead to a choice of cuts that is far from optimal. The different event, jet and track cuts are summarized in the sections that follow.

5.5.1 Event selection

Hadronic Z^0 decays are selected by requiring

1. the total energy measured in the calorimeters $\geq 10\%$ of $2 \times E_{beam}$,

2. the measured energy is deposited on both sides ($+z$ and $-z$) of the detector,

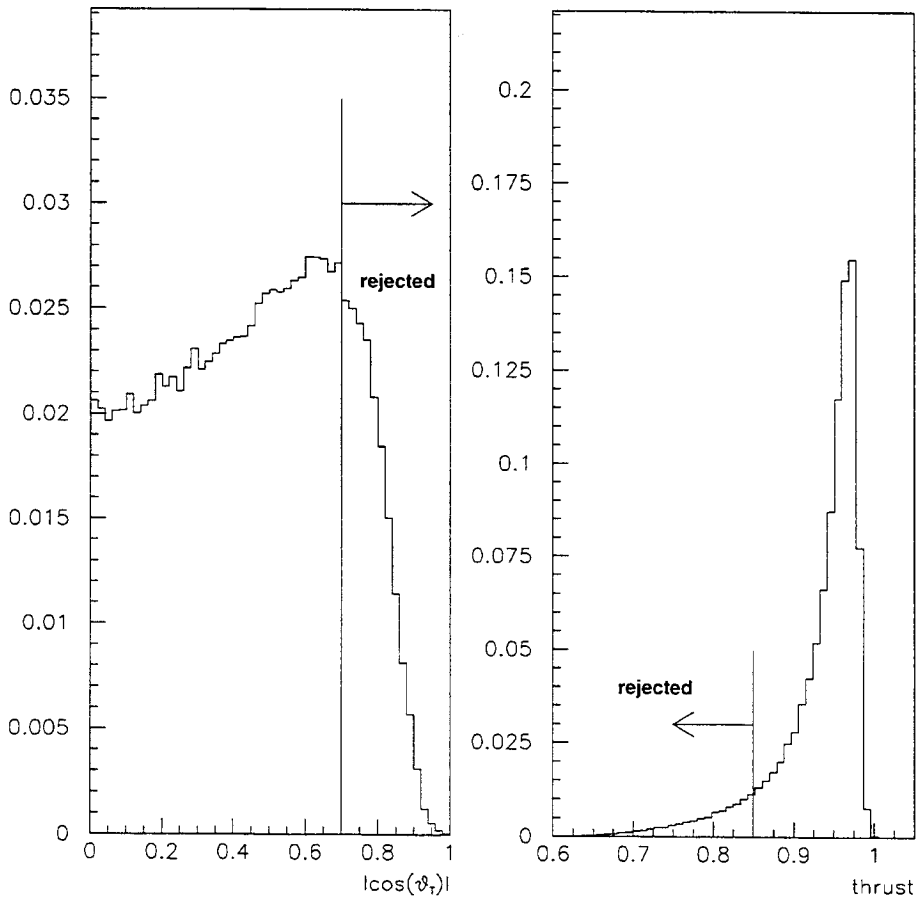

Figure 5.14: The left plot shows the $|\cos(\theta_T)|$ distribution of events in the data. The right plot shows the thrust distribution of events in the data.

3. $\geq$7 regions of energy deposition in the calorimeters ("clusters") with $E_{barrel} \geq$ 0.1 GeV or $E_{endcap} \geq$ 0.2 GeV, and

4. $\geq$7 well measured tracks.

The efficiency to select hadronic Z^0 decays is 98.1%, with a background less than 0.1% [92]. Since all tracks used in the analysis must have silicon vertex detector hits associated to them, events were selected only if the silicon vertex detector was fully operational at the time of data-taking.

After these preliminary selection criteria are satisfied, the two main goals of the event selection are to select $Z \rightarrow q\bar{q}$ events that are well contained in the central portion of the tracking detectors (especially the silicon vertex detector) and to select events that are two-jet-like. The first requirement is met by requiring that $|\cos(\theta_T)| \leq 0.7$, where θ_T is the polar angle of the "thrust axis" of an event. The thrust axis is determined by calculating a quantity called the "thrust", T, of an event:

$$T = \text{maximum} \left(\frac{\sum_i |\hat{t} \cdot \vec{p}_i|}{\sum_i |\vec{p}_i|} \right), \tag{5.10}$$

where $\vec{p}_i$ are the momemtum vectors for tracks and energy clusters in an event, and $\hat{t}$, the thrust axis, is the vector that maximizes the right hand side of equation 5.10. In a two jet event, the thrust axis tends to be collinear with the jets. The expected uncertainty for $Br(b \rightarrow D\bar{D}X)$ does not have a strong dependence on $\cos(\theta_T)$ unless $|\cos(\theta_T)| \leq 0.6$; the statistical uncertainty becomes quite large if the $|\cos(\theta_T)|$ cut is too tight.

The requirement that the event be two-jet-like is met by making a cut on the thrust of an event. The thrust (see equation 5.10) is a measure of the anisotropy of

the energy flow in the event. A cut requiring $T > 0.85$ is used. Lower T values are associated with events containing more than two jets. Two jet events are preferred here as the analysis uses jets that are opposite identified b jets. Events with three or more jets (resulting from hard gluon emission) are undesirable as gluon jets are a background to the b jets that the analysis studies. Although the statistical uncertainty increases as the T cut is increased, the systematic uncertainty due to gluon jet background is reduced. Figure 5.14 shows the distributions of T and $|\cos(\theta_T)|$ in the data.

5.5.2 Jet selection

The purpose of the jet selection is to obtain a high purity, unbiased sample of jets containing b hadrons. This is achieved by first calculating a b-likelihood variable for each jet in an event. The b-likelihood variable is calculated by the LEP-2 b-tagging algorithm [88, 89]. This "b-tagger" is a sophisticated algorithm that uses several artificial neural networks to calculate three discriminants that include lifetime, lepton and jet shape information. The discriminants are combined to produce a single likelihood variable that is used to identify jets containing b hadrons. Figure 5.15 shows the distributions of the b-tagging variable for jets initiated by different flavour quarks. The LEP-2 b-tagger has a good b-tagging efficiency while maintaining a high b purity. For this analysis, a cut on the b likelihood of > 0.9 was chosen to obtain a high purity b jet sample (purity $\sim$95% and efficiency $\sim$40%). Backgrounds from uds and c jets produce significant systematic uncertainties in the measurement of $\mathrm{Br(b \to D\bar{D}X)}$ so it is important to reduce these backgrounds.

A jet is used in the analysis if the opposite jet passes the b-tag cut. If both jets pass the b-tag cut then both jets are used. The opposite jet is used for b-tagging to

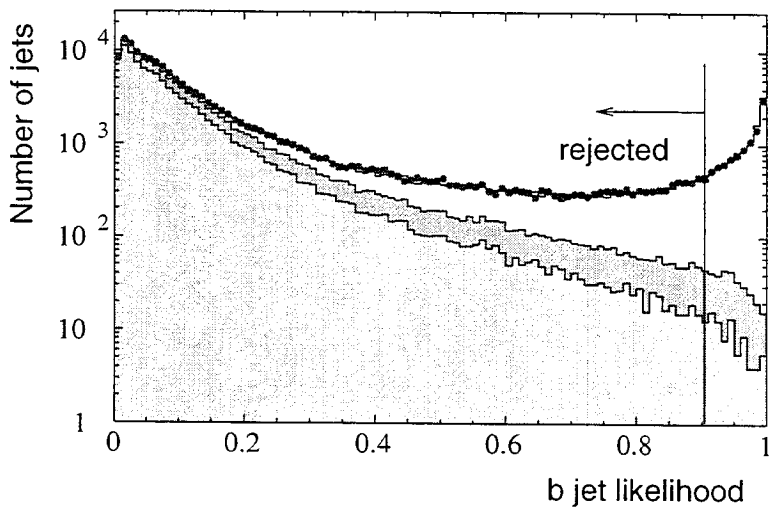

Figure 5.15: b-tagging variable for jets initiated by different flavour quarks in simulated and data hadronic Z^0 decays in 1994 configuration of detector [89]. The light grey histogram represents simulated jets initiated by u, d, or s quarks; the darker grey histogram represents simulated c jets; and, the open histogram represents simulated b jets. The data points represent real data. Jets opposite a jet with a b-likelihood < 0.9 are not used in the analysis.

provide an unbiased sample of predominantly b jets.

5.5.3 Track selection

Track selection cuts are made to select a sample of well measured tracks that is enriched in decay products of b and D hadrons. As a preliminary track selection, the standard OPAL "quality" track selection cuts were employed (see table 5.3). In addition, tracks were required to have two hits in each of SI-$r\phi$ and SI-z as Monte Carlo studies show this requirement greatly reduces the systematic uncertainty due to detector resolution modelling (see section 5.3).

It is important to select tracks that are predominantly from b and D hadron decays as these tracks differentiate single from double charm b decays. Fragmentation tracks in jets containing a single charm b decay are the same as fragmentation tracks in jets containing a double charm b decay, so they diminish the separation obtainable from the b and D tracks. The most useful cuts for reducing tracks from fragmentation are cuts on a track's impact parameter significance, S, momentum, p, angle with respect to the jet axis, θ_{t-j}, and rapidity with respect to the jet axis, $y = \frac{1}{2}\ln(\frac{E+p_{||}}{E-p_{||}})$ (E is the energy of the track and $p_{||}$ is the component of the track's momentum that is parallel to the jet axis). Figure 5.16 shows the distributions of these variables for tracks from fragmentation and b or D decays.

Track origin	Fraction
b and D hadron decay	0.686
fragmentation	0.270
K^0 and Λ decay, γ conversions	0.025
other	0.019

Table 5.6: Origin of tracks passing track selection cuts (after event and jet cuts are applied). Tracks whose origin is classified as "other" are mostly from interactions with the detector material.

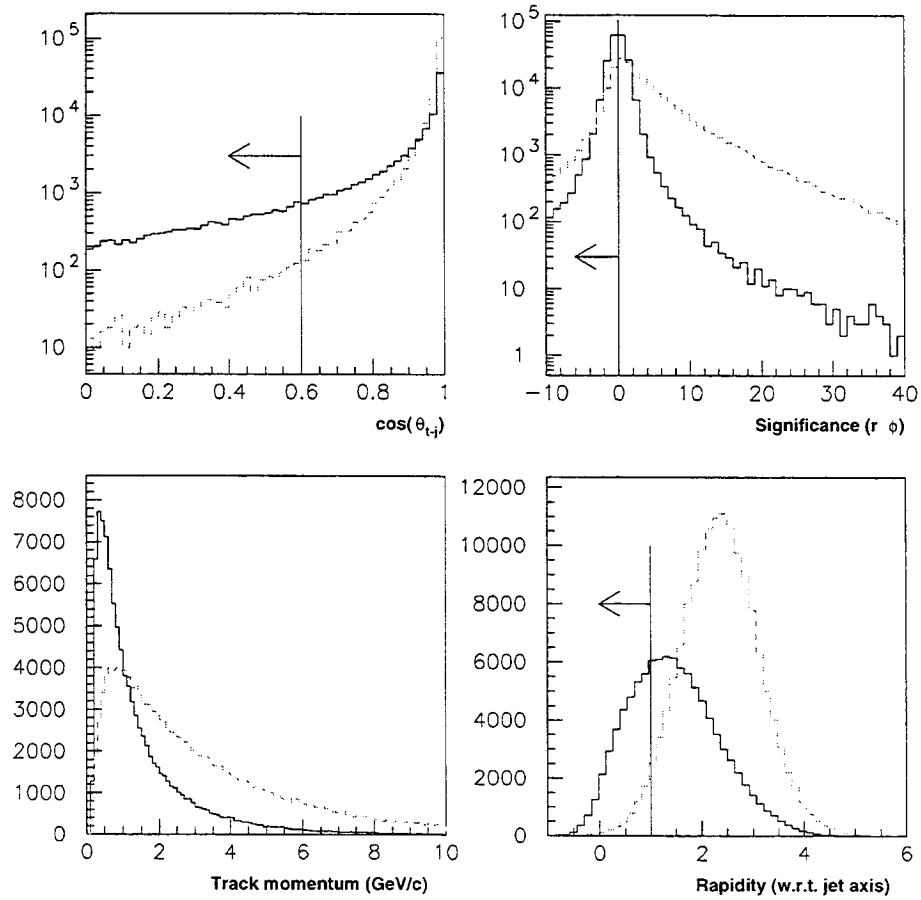

Figure 5.16: Track cuts used for analysis. Tracks on the same side of the vertical line as the arrow are rejected. The tracks shown in these plots satisfied the quality and silicon detector hits cuts but did not have the other track cuts applied to them. The solid histograms represent fragmentation tracks. The dashed histograms represent tracks from b and D hadron decays. The top left plot shows the angle of the track with respect to the jet axis. The top right plot shows the impact parameter significance in the $r - \phi$ plane. The bottom left plot shows the track momentum. For reasons described in the text, no additional momentum cut was applied (a transverse momentum cut, $p_T > 0.15$ GeV/c, was applied in the quality track cuts). The bottom right plot shows the rapidity of the track with respect to the jet axis.

Tracks with $S < 0$ tend to come from fragmentation so all tracks were required to have $S > 0$. Also, very few tracks from b and D decays have $S > 25$ so a cut of $0 < S < 25$ is used. Tracks from fragmentation have a soft p spectrum but MC studies show that a p cut harder than $p > 0.15$ GeV/c increases the statistical uncertainty of Br(b $\rightarrow$ D$\bar{\text{D}}$X). This occurs because the number of jets with at least one selected track is reduced. For this reason, $p > 0.15$ GeV/c was chosen as the momentum cut. The angle between the direction of the track and the jet axis, θ_{t-j}, was required to be <0.6 radians. Most b and D daughter tracks fall inside a cone about the jet axis defined by this cut, while many fragmentation tracks are rejected. Finally, a cut of $y > 1.0$ was made to further reduce the fraction of fragmentation tracks selected. Tracks from b and D decays tend to follow the direction of the initial b quark (as approximated by the jet momentum vector) and have high momentum so have larger y than fragmentation tracks. The rapidity cut is similar to a combination of the p and θ_{t-j} cuts but this cut further reduces the total expected uncertainty. Table 5.6 lists the fractions of tracks from different origins that pass all track selection cuts.

Chapter 6

Results

6.1 Results for each year

Separate fits of the $-\ln(P_j)$ distributions are performed for each year of data taking to determine $\mathrm{Br}(b \to D\bar{D}X)$. The results of these fits are shown in table 6.1. A total of 91 different $-\ln(P_j)$ bins are used for each year for the different track multiplicities. There are 7 free parameters: one value of $\mathrm{Br}(b \to D\bar{D}X)$ for each track multiplicity and α. This results in a total of $91 - 7 = 84$ degrees of freedom. With χ^2 values of 88.0, 96.6, and 80.4 for 1993-95 respectively, the probabilities to obtain these χ^2 values or larger for 84 degrees of freedom are 0.36, 0.16, and 0.59. For this reason, the shapes of the MC $-\ln(P_j)$ distributions are considered consistent with the data $-\ln(P_j)$ distributions for each year of data taking.

The best fit values of $\mathrm{Br}(b \to D\bar{D}X)$ for each year and each track multiplicity bin are not constrained to the physically allowed region, $0\% < \mathrm{Br}(b \to D\bar{D}X) < 100\%$. This is done because the results for each year and each track multiplicity bin are combined. If any of the branching ratios had been constrained to be between 0% and 100%, the combined result would have been biased [93].

year	Br(b $\rightarrow$ D$\bar{\text{D}}$X) (%)	σ_{stat} (%)	α	χ^2/d.o.f.
1993	-2.2	6.5	$(1.0 \pm 2.4) \times 10^{-3}$	88.0/84
1994	15.0	4.4	$(-0.8 \pm 2.0) \times 10^{-3}$	96.6/84
1995	15.5	6.7	$(-1.4 \pm 2.7) \times 10^{-3}$	80.4/84

Table 6.1: Results of $-\ln(P_j)$ fits for each year of data-taking. Only the statistical errors of the fits are shown in this table. The systematic uncertainties are discussed in detail in chapter 7. The best fit value of the α parameter used in the fitting function (equation 5.4) is listed. The number of degrees of freedom for each fit was 84.

The best fit values of α are consistent with zero for each year of data taking. This shows that the physics inputs to the MC and the detector modelling are in reasonable agreement with the data. The statistical uncertainties for the different α values are all smaller than the value of σ_α ($= 3 \times 10^{-3}$) that is used to constrain α.

Figures 6.1, 6.3, 6.5 show the fits of the MC PDFs to the data for each year. The residuals of the $-\ln(P_j)$ bins are shown in figures 6.2, 6.4, 6.6.

6.2 Cross check: analysis with simulated "pseudo-data"

In order to test the experimental method that is used for the analysis, the analysis was first performed with a set of simulated "pseudo-data" for the 1994 configuration of the OPAL detector. The simulated data that were used to construct the MC PDFs were distinct from the simulated data that were used for the pseudo-data. One million hadronic Z^0 decays were used for the pseudo-data. This number was chosen so that the pseudo-data sample was comparable to the real data sample used in the 1994 analysis. Two million $Z^0 \rightarrow b\bar{b}$ and one million five-flavour hadronic Z^0 decays were used to generate the MC PDFs. Although only one million five-

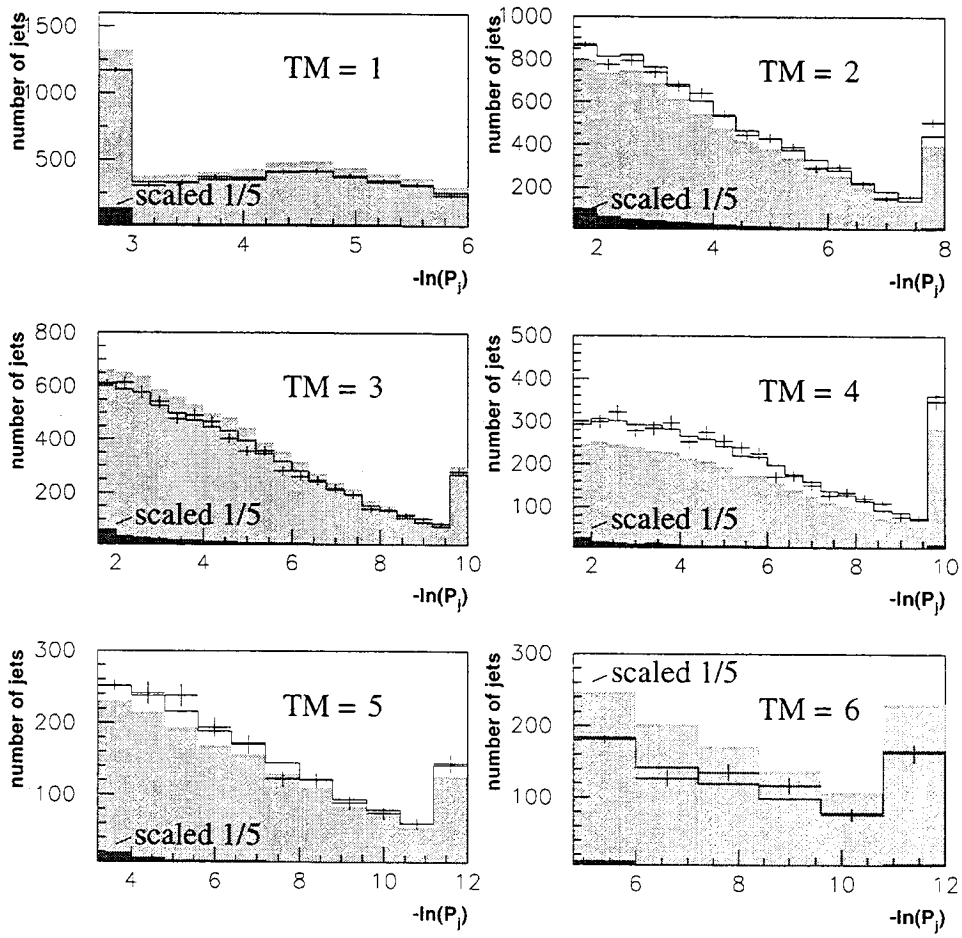

Figure 6.1: Fits of MC PDFs to data for 1993 for each track multiplicity bin. The line histogram is the sum of the MC PDFs. The dark grey histogram depicts the backgrounds: b $\rightarrow$ 0 charm, b $\rightarrow$ charmonium, *uds* jets, *c* jets, and gluon jets in $Z^0 \rightarrow b\bar{b}$ events. The light grey histogram depicts the single charm b decays, and the open white histogram depicts the b $\rightarrow$ D$\bar{\text{D}}$X component. The number of jets in the first bin of each histogram is scaled by a factor of 1/5 to make the b $\rightarrow$ D$\bar{\text{D}}$X contribution easier to see. For some track multiplicities (*e.g.* TM = 1, 3, 6 above), the single charm component is > 100% and Br(b $\rightarrow$ D$\bar{\text{D}}$X) < 0%; for these cases, there is no visible b $\rightarrow$ D$\bar{\text{D}}$X component in the plots and the number of entries in the light grey histogram is greater than the number of entries in the line histogram that is the sum of all the MC PDFs.

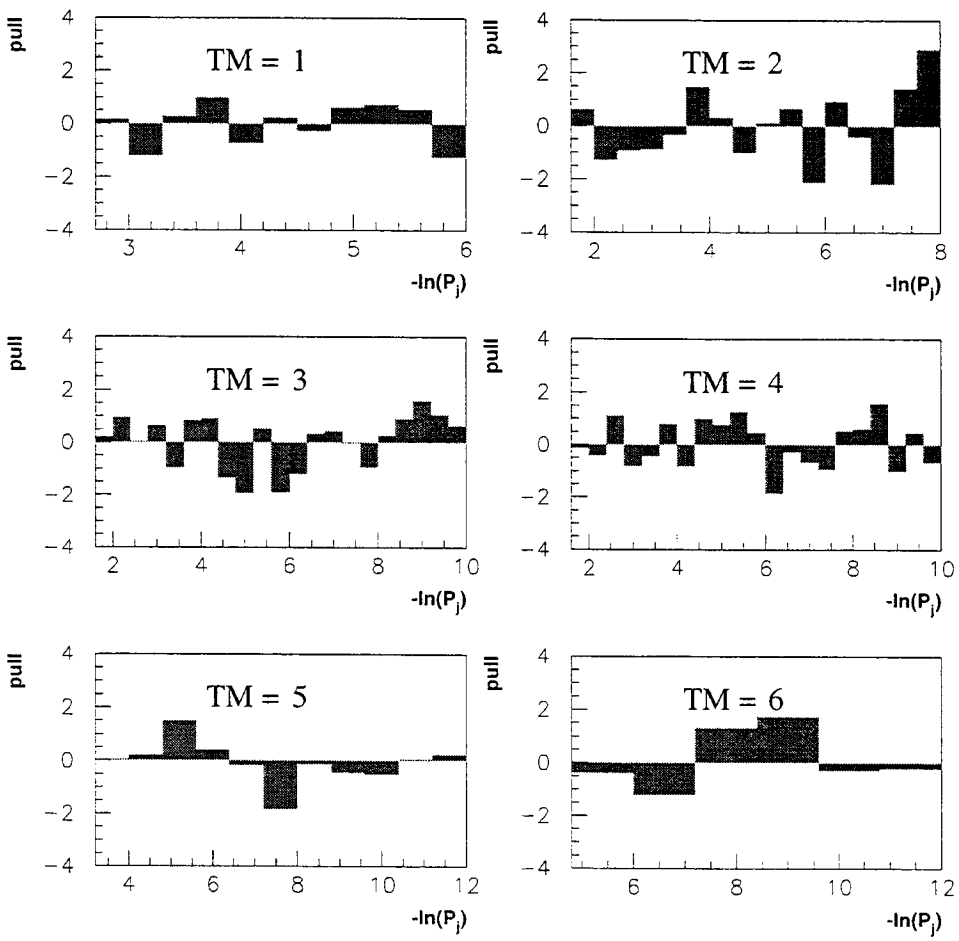

Figure 6.2: Residuals for fits of MC $-\ln(P_j)$ PDFs to 1993 data.

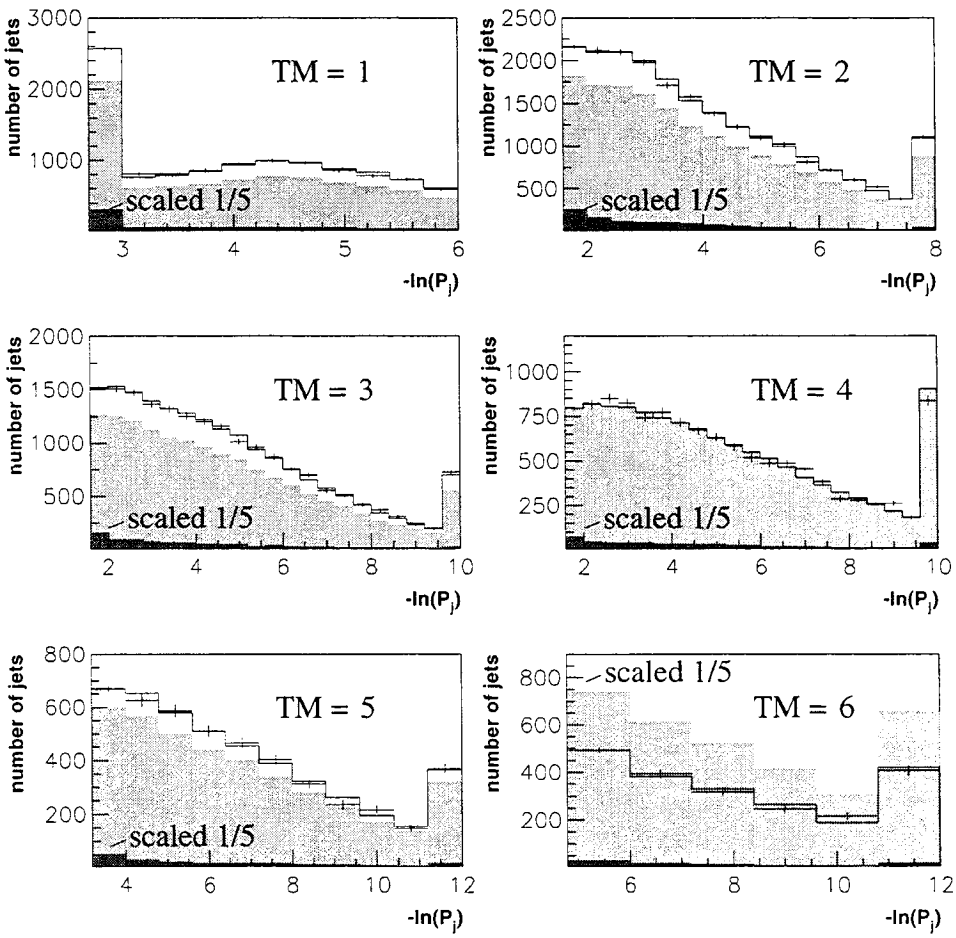

Figure 6.3: Fits of MC PDFs to data for 1994 for each track multiplicity. For details about this figure, see the caption for figure 6.1.

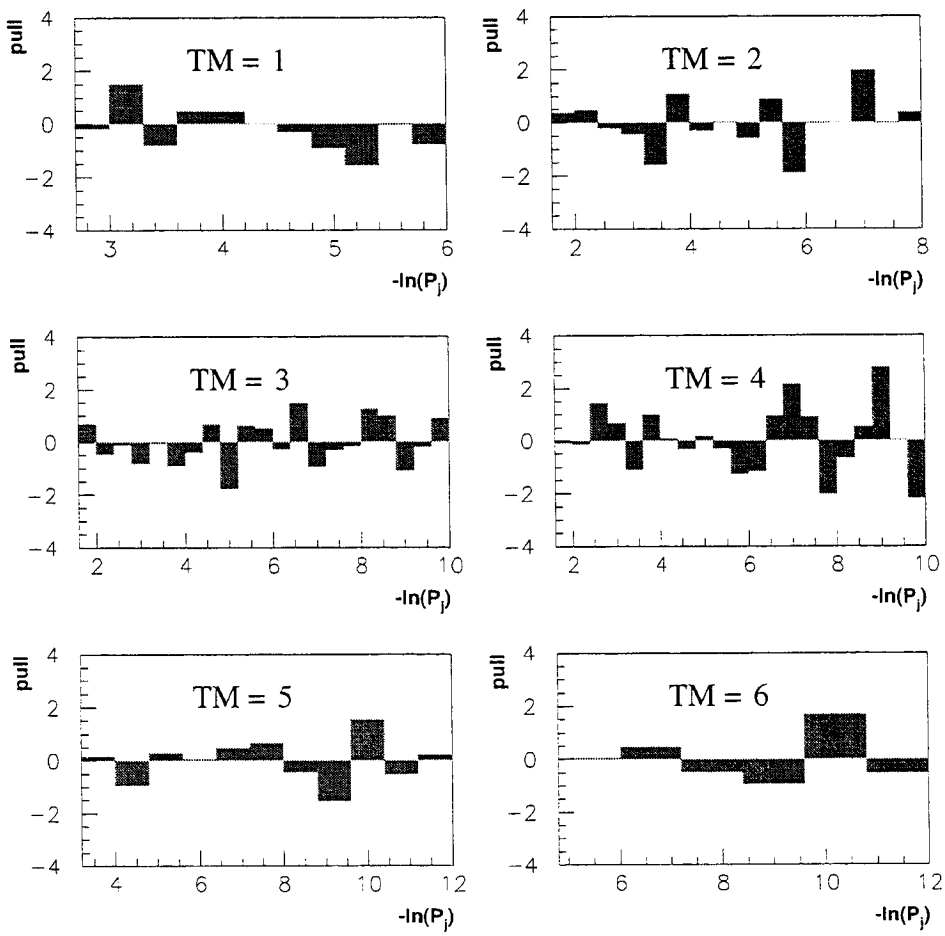

Figure 6.4: Residuals for fits of MC $-\ln(P_j)$ PDFs to 1994 data.

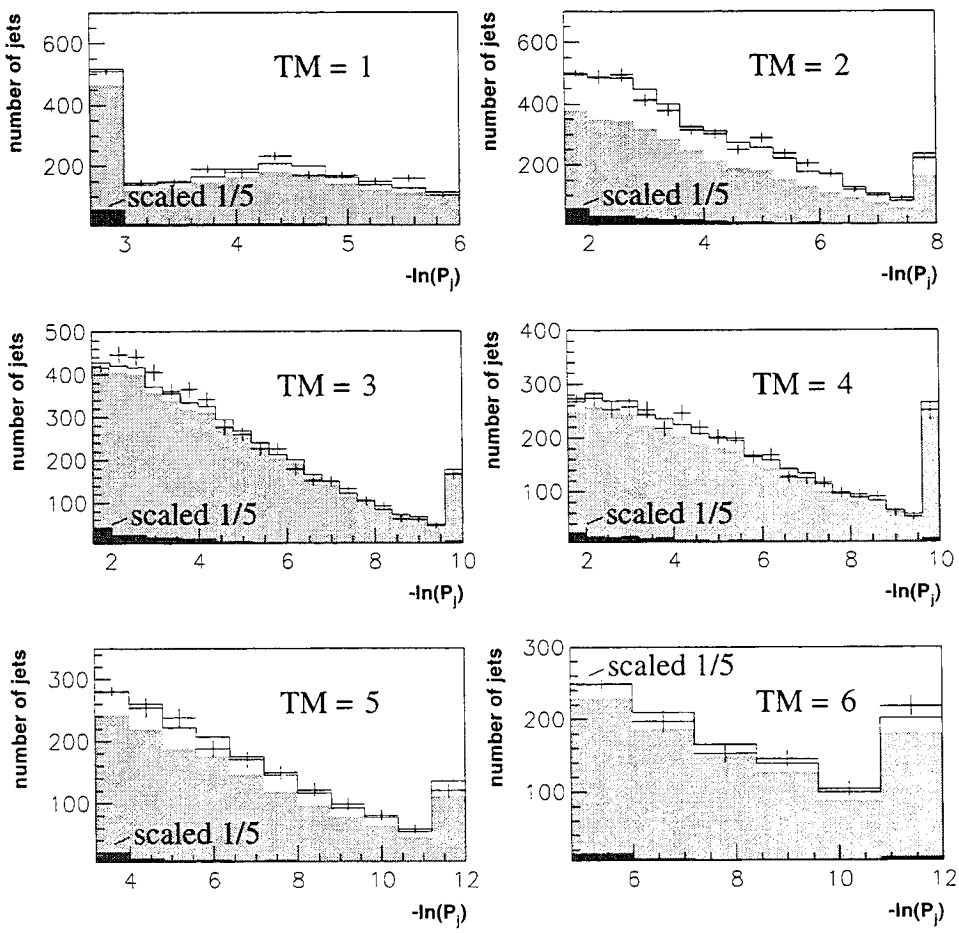

Figure 6.5: Fits of MC PDFs to data for 1995 for each track multiplicity. For details about this figure, see the caption for figure 6.1.

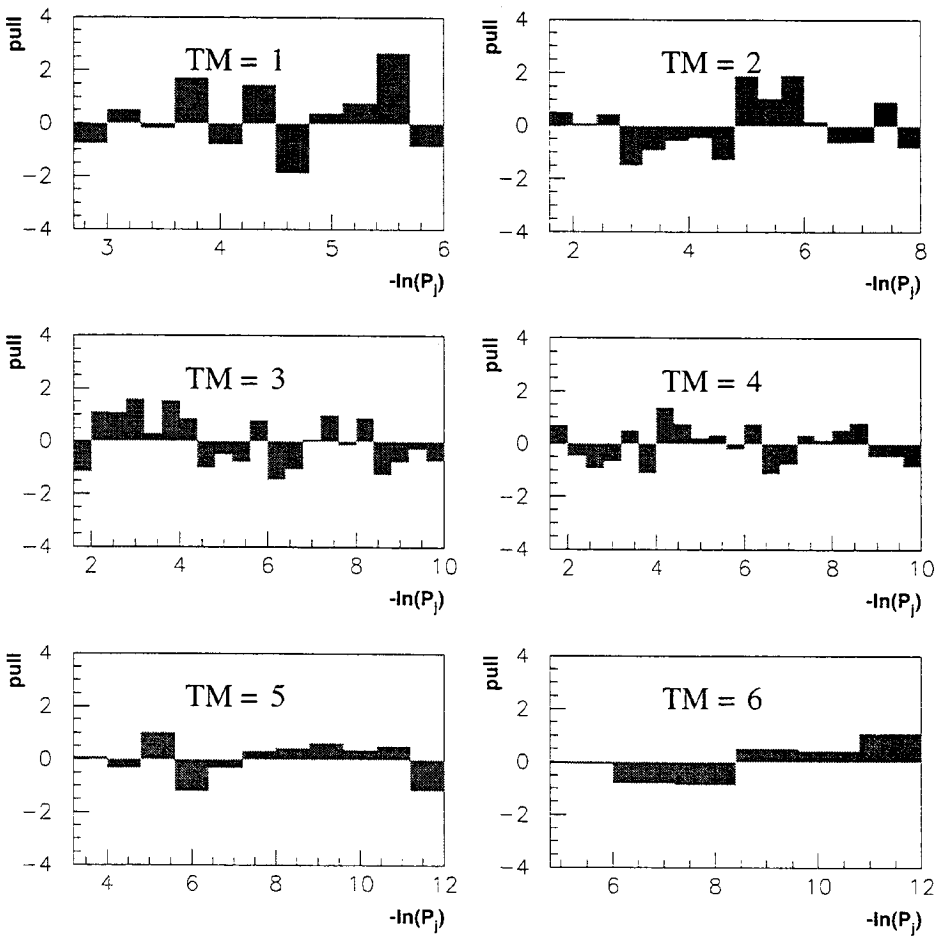

Figure 6.6: Residuals for fits of MC $-\ln(P_j)$ PDFs to 1995 data.

flavour hadronic Z^0 decays were used, the background PDFs had large statistics as no b-tagging requirement was made of the opposite jet. The OPAL R_b analysis [94] showed that there is very little correlation between opposite jets in $udsc$ events so this did not distort the shapes of the backgrounds. The ratio of $Z^0 \to b\bar{b}$ MC events to data events was approximately the same in the analysis of the real data.

The Br(b $\to$ D$\bar{\text{D}}$X) result obtained in this pseudo-data analysis, $(17.4^{+5.5}_{-4.6}(stat.))\%$, is in agreement with the true Br(b $\to$ D$\bar{\text{D}}$X) value in the pseudo-data, 13.3%. The magnitude of the statistical uncertainty is in line with the statistical uncertainty from the fit to the 1994 data. The χ^2/d.o.f. for the fit was 90.2/84. The best fit value for α was $(-0.02 \pm 2.01) \times 10^{-3}$. As the MC and pseudo-data were generated with the same physics inputs and the same detector simulation, the fact that α was so close to zero is not surprising. These results give confidence in the results obtained with the real data.

Unfortunately, the sample size of the MC was not sufficient to indicate any bias in the estimator for Br(b $\to$ D$\bar{\text{D}}$X) that is less than σ_{stat}. However, the toy MC study that involved fitting similar gaussians (see section 5.4.1) showed that the results of those fits are not biased. The fits for the toy MC study and the Br(b $\to$ D$\bar{\text{D}}$X) analysis are very similar. MC studies also show that in the simulated data, there are no significant differences in the efficiencies to select the different topologies of b hadron decays (single charm, double charm, etc.) after cuts have been applied.

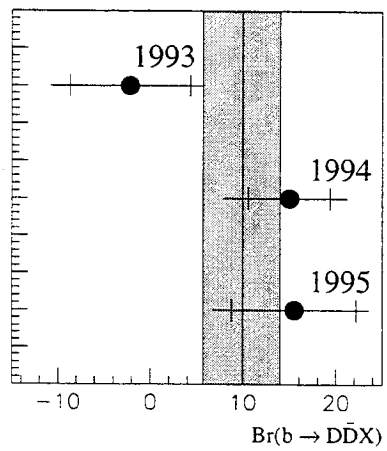

Figure 6.7: Combined result for Br(b → DD̄X). The inner portion of the error bars is the statistical uncertainty. The outer portion is the systematic uncertainty due to detector modelling combined in quadrature with the statistical uncertainty.

6.3 Combination of Br(b → DD̄X) results

The Br(b → DD̄X) results for each year of data taking can be combined by calculating a weighted mean that yields

$$\mathrm{Br(b \to D\bar{D}X)} = (10.0 \pm 3.2(stat.)^{+2.4}_{-2.9}(syst.\ det.))\%, \tag{6.1}$$

where *syst. det.* is the portion of the uncertainty that is uncorrelated from year-to-year due to detector modelling (see section 7.3.4). Systematic uncertainties from the modelling of particle physics processes (see section 7.4) are fully correlated from year to year so do not need to be considered when the weighted mean for Br(b → DD̄X) is calculated. The weights for each year are $1/(\sigma^2_{stat.} + \sigma^2_{syst.\ det.})$. Figure 6.7 shows the Br(b → DD̄X) results for the three separate years of data taking and the combined Br(b → DD̄X) result. The χ^2/d.o.f. for combining the results from the three years

is 3.7/2. The probability to have this χ^2 or larger with two degrees of freedom is 0.16. This combination includes the statistical correlation between the 1993 and 1994 results (see section 4.2). The MC $Z^0 \rightarrow b\bar{b}$ samples for 1993 and 1994 are much larger than the $Z^0 \rightarrow b\bar{b}$ data samples for these years, so the effect of this correlation (assumed to be 100% for the MC statistics) on the combined statistical uncertainty is minimal.

The final result for Br(b $\rightarrow$ D$\bar{\text{D}}$X), including statistical, and detector and particle physics systematic uncertainties is

$$\text{Br(b} \rightarrow \text{D}\bar{\text{D}}\text{X)} = (10.0 \pm 3.2(stat.)^{+2.4}_{-2.9}(syst.\ det.)^{+10.4}_{-9.0}(syst.\ phys.))\%, \qquad (6.2)$$

where *syst. phys.* is the systematic uncertainty due to the modelling of the underlying particle physics.

6.4 n_c result

This Br(b $\rightarrow$ D$\bar{\text{D}}$X) result can be combined with previous experimental determinations of Br(b $\rightarrow$ charmonium) (= $(2.4 \pm 0.3)\%$ [36]) and Br(b$\rightarrow$ no charm) (= $(0.7 \pm 2.1)\%$ [37]) in equation 2.12 to give

$$n_c = 1.12^{+0.11}_{-0.10}. \qquad (6.3)$$

The uncertainty of n_c includes the correlations between the measured value of Br(b $\rightarrow$ D$\bar{\text{D}}$X) and the assumed values of Br(b$\rightarrow$ no charm) and Br(b $\rightarrow$ charmonium).

Chapter 7

Systematic Uncertainties

This chapter outlines the sources of systematic uncertainty for $Br(b \rightarrow D\bar{D}X)$. The main method used to estimate the systematic uncertainties is described in section 7.1. The statistical uncertainty inherent in the estimated systematic uncertainties is discussed in section 7.2. Details about the various sources of systematic uncertainty are described in the remainder of the chapter. The systematic uncertainties for $Br(b \rightarrow D\bar{D}X)$ for each year of data taking and for the combined years are summarized in tables 7.1 and 7.2.

7.1 Determination of systematic uncertainties

The main method for estimating the systematic uncertainties involves weighting jets in the MC in order to effectively change the value of a particular physics input (e.g. mean lifetime of B_s meson) by its one standard deviation uncertainty. For the lifetime example, the weight that a jet receives is determined by the proper lifetime of a B_s meson in the jet (weight = 1.0 if there is no B_s meson). The values of the normalized exponential functions (with the original and new B_s lifetimes) at that

Source	Value	$\sigma_{Br(b\to D\bar{D}X)}$ (%)				Sign of $\frac{\Delta Br(b\to D\bar{D}X)}{\Delta Source}$
		1993	1994	1995	Combined	
d_0 modelling	$\pm 1.5\%$	$^{+3.2}_{-4.5}$	$^{+4.5}_{-5.6}$	$^{+3.0}_{-3.0}$	N/A	N/A
σ_{d_0} modelling	$\pm 0.5\%$	± 0.6	± 0.8	± 0.8	N/A	N/A
ϵ_{track}	see text	± 0.3	± 0.3	± 0.3	N/A	N/A
$< x_E >$	0.7151 ± 0.0025	± 0.0	± 0.0	± 0.0	± 0.0	N/A
$< N_{ch} >_{frag}$	12.46 ± 0.32	± 5.9	± 5.7	± 7.8	± 6.2	+
$< x_{b\to D} >$	see text	± 0.7	± 0.3	± 1.0	± 0.5	N/A
τ_{B^0}	(1.542 ± 0.016)ps	± 1.1	± 0.5	± 1.5	± 0.9	−
τ_{B^+}	(1.674 ± 0.018)ps	$^{+1.3}_{-1.2}$	$^{+0.6}_{-0.4}$	$^{+1.7}_{-1.6}$	± 1.0	−
τ_{B_s}	(1.461 ± 0.057)ps	$^{+0.8}_{-0.7}$	$^{+0.4}_{-0.3}$	± 1.4	$^{+0.7}_{-0.6}$	−
τ_{Λ_b}	(1.208 ± 0.051)ps	$^{+1.1}_{-1.0}$	$^{+0.8}_{-0.7}$	$^{+1.4}_{-1.3}$	$^{+1.0}_{-0.9}$	−
τ_{D^+}	(1.051 ± 0.013)ps	± 0.2	± 0.1	± 0.2	± 0.1	−
τ_{D^0}	(0.412 ± 0.003)ps	± 0.3	± 0.3	± 0.3	± 0.3	−
$\tau_{D_s^+}$	(0.490 ± 0.009)ps	± 0.1	± 0.2	± 0.5	± 0.3	−
$\tau_{\Lambda_c^+}$	(0.200 ± 0.005)ps	± 0.2	± 0.1	± 0.2	± 0.2	−
f_{Λ_b}	$(10.5 \pm 2.0)\%$	± 1.7	± 1.4	$^{+2.7}_{-2.5}$	± 1.7	+
f_{B_s}	$(9.2 \pm 2.4)\%$	∓ 0.3	± 0.3	$^{+1.2}_{-1.0}$	$^{+0.4}_{-0.3}$	−
$g \to b\bar{b}$	$(2.54\pm0.50)\times10^{-3}$	± 0.0	± 0.1	∓ 0.2	± 0.0	N/A
$g \to c\bar{c}$	$(2.99\pm0.39)\times10^{-2}$	± 0.4	$^{+0.2}_{-0.3}$	± 0.0	± 0.2	+

Table 7.1: Summary of systematic errors for Br(b $\to$ D$\bar{\text{D}}$X) for 1994 (part 1). The continuation of the summary, including the total correlated and uncorrelated uncertainties, is found in table 7.2. The definitions and explanations of all the sources of uncertainty are contained in sections 7.3 and 7.4. The column containing the signs of $\frac{\Delta Br(b\to D\bar{D}X)}{\Delta Source}$ can be combined with $\sigma_{Br(b\to D\bar{D}X)}$ to update Br(b $\to$ D$\bar{\text{D}}$X) if measurements of the sources of systematic uncertainty are updated. For example, if the central value of τ_{Λ_b} is measured to be 0.010 ps longer, then the central value for Br(b $\to$ D$\bar{\text{D}}$X) decreases (because $\frac{\Delta Br(b\to D\bar{D}X)}{\Delta Source}$ is negative) by 0.9(0.010/0.051)%.

Source	Value	$\sigma_{Br(b\to D\bar{D}X)}$ (%) 1993	1994	1995	Combined	Sign of $\frac{\Delta Br(b\to D\bar{D}X)}{\Delta Source}$
$< n_{ch} >_{D^+}$	2.38 ± 0.06	$^{+0.4}_{-0.6}$	$^{+0.5}_{-0.7}$	$^{+0.9}_{-1.3}$	$^{+0.6}_{-0.8}$	−
$< n_{ch} >_{D^0}$	2.56 ± 0.05	$^{+1.4}_{-1.8}$	$^{+0.7}_{-1.1}$	$^{+0.9}_{-1.4}$	$^{+0.9}_{-1.3}$	−
$< n_{ch} >_{D_s^+}$	2.69 ± 0.33	$^{-1.3}_{+1.2}$	$^{+3.2}_{-2.9}$	$^{-0.5}_{+1.4}$	$^{+1.3}_{-1.0}$	−
$< n_{ch} >_{\Lambda_c^+}$	2.7 ± 0.5	$^{+0.8}_{-1.2}$	$^{+1.3}_{-1.1}$	$^{+1.0}_{-0.3}$	$^{+1.1}_{-0.9}$	−
$< n_{\pi^0} >_{D^+}$	1.18 ± 0.33	$^{+0.2}_{-1.5}$	$^{-1.6}_{+0.8}$	$^{+6.7}_{-4.5}$	$^{+0.7}_{-0.9}$	+
$< n_{\pi^0} >_{D^0}$	1.31 ± 0.27	$^{+6.4}_{-3.8}$	$^{+4.5}_{-1.7}$	$^{+11.0}_{-7.8}$	$^{+6.4}_{-3.5}$	+
$< n_{\pi^0} >_{D_s^+}$	2.0 ± 1.4	$^{+0.7}_{-1.3}$	$^{+0.1}_{-1.1}$	$^{+7.4}_{-2.3}$	$^{+1.8}_{-1.4}$	+
$Br(D^+ \to \bar{K}^0 X)$	$(61.2 \pm 7.8)\%$	$^{+1.1}_{-0.9}$	$^{+1.3}_{-1.2}$	$^{+0.5}_{-0.7}$	$^{+1.1}_{-1.0}$	+
$Br(D^0 \to \bar{K}^0 X)$	$(45.5 \pm 5.9)\%$	± 1.5	± 1.6	± 0.2	± 1.3	+
$Br(D_s^+ \to \bar{K}^0 X)$	$(39^{+28}_{-27})\%$	± 0.6	± 0.7	± 6.0	± 1.9	−
$Br(\Lambda_c^+ \to \bar{\Lambda} X)$	$(35 \pm 11)\%$	± 0.9	$^{+0.1}_{-0.2}$	$^{+0.4}_{-0.3}$	± 0.4	+
$< n_{ch} >_b$	4.97 ± 0.07	$^{+0.9}_{-0.8}$	± 0.8	± 0.3	± 0.7	−
$f_{D^+}(1c)$	$(23.3 \pm 2.9)\%$	± 1.7	± 1.1	$^{+1.9}_{-1.7}$	$^{+1.3}_{-1.4}$	−
$f_{D^+}(2c)$	$(17.0 \pm 4.9)\%$	$^{+1.4}_{-1.2}$	± 1.2	$^{-5.4}_{+5.4}$	$^{-0.2}_{+0.3}$	−
$f_{\Lambda_c^+}(1c)$	$(10.0 \pm 2.9)\%$	$^{+3.2}_{-3.3}$	± 1.7	$^{+2.9}_{-3.1}$	$^{+2.3}_{-2.4}$	+
$f_{\Lambda_c^+}(2c)$	$(7.4 \pm 2.9)\%$	$^{-0.1}_{+0.7}$	$^{+2.6}_{-2.2}$	± 1.5	$^{+1.7}_{-1.3}$	+
ϵ_g	$\pm 10\%$	± 0.4	± 0.4	± 0.4	± 0.4	+
ϵ_c	$\pm 10\%$	± 2.0	± 2.0	± 2.0	± 2.0	+
ϵ_{uds}	$\pm 10\%$	± 0.8	± 0.8	± 0.8	± 0.8	+
Br(b→ no charm)	$(0.7 \pm 2.1)\%$	$^{+3.0}_{-1.0}$	$^{+3.0}_{-1.0}$	$^{+3.0}_{-1.0}$	$^{+3.0}_{-1.0}$	+
Br(b→ charmonium)	$(2.4 \pm 0.3)\%$	± 0.3	± 0.3	± 0.3	± 0.3	+
Correlated total					$^{+10.4}_{-9.0}$	
Uncorrelated total					$^{+2.4}_{-2.9}$	

Table 7.2: Summary of systematic errors for Br(b → DD̄X) for 1994 (part 2). The calculation of the total of the uncorrelated systematic (detector) uncertainties is explained in section 7.3.4. The correlated systematic uncertainties are due to particle physics modelling. The caption in table 7.1 explains how the column containing the signs of $\frac{\Delta Br(b\to D\bar{D}X)}{\Delta Source}$ can be used to update Br(b → DD̄X).

particular proper lifetime are then calculated. The weight that the jet is assigned is just the ratio of these values. The fit to determine $Br(b \rightarrow D\bar{D}X)$ is then redone with the weighted MC PDFs. The difference between the original $Br(b \rightarrow D\bar{D}X)$ (determined using unweighted MC PDFs) and the new $Br(b \rightarrow D\bar{D}X)$ represents the one standard deviation uncertainty from the physics input that is varied by the weighting procedure. Unless stated otherwise, this method is used to determine all the systematic uncertainties that arise from particle physics modelling.

7.2 Statistical uncertainty in estimates of systematic uncertainty

The method used in this analysis to determine the systematic uncertainty is quite reliable as long as the weighting procedure does not introduce significant amounts of statistical "noise" into the PDFs. Significant amounts of statistical noise can lead to a poor estimate of the systematic uncertainty due to a physics input. For example, if the weighting procedure randomly weights events *without* changing the underlying parent distributions for the PDFs (histograms) then the systematic uncertainty (and its estimate) should be zero. The randomly weighted PDFs will in general yield a different value for $Br(b \rightarrow D\bar{D}X)$; the difference between the values obtained with the unweighted and weighted PDFs will depend on the amount of noise introduced by the weighting procedure. Noise is also introduced into estimates of "real" systematic uncertainties. One can visualize this problem by considering the possible values of $Br(b \rightarrow D\bar{D}X)$ obtained after weighting. The distribution of possible $Br(b \rightarrow D\bar{D}X)$ values is gaussian (see figure 7.1). The mean and width of the gaussian depend on the weights applied to the MC. If little statistical noise is introduced then the

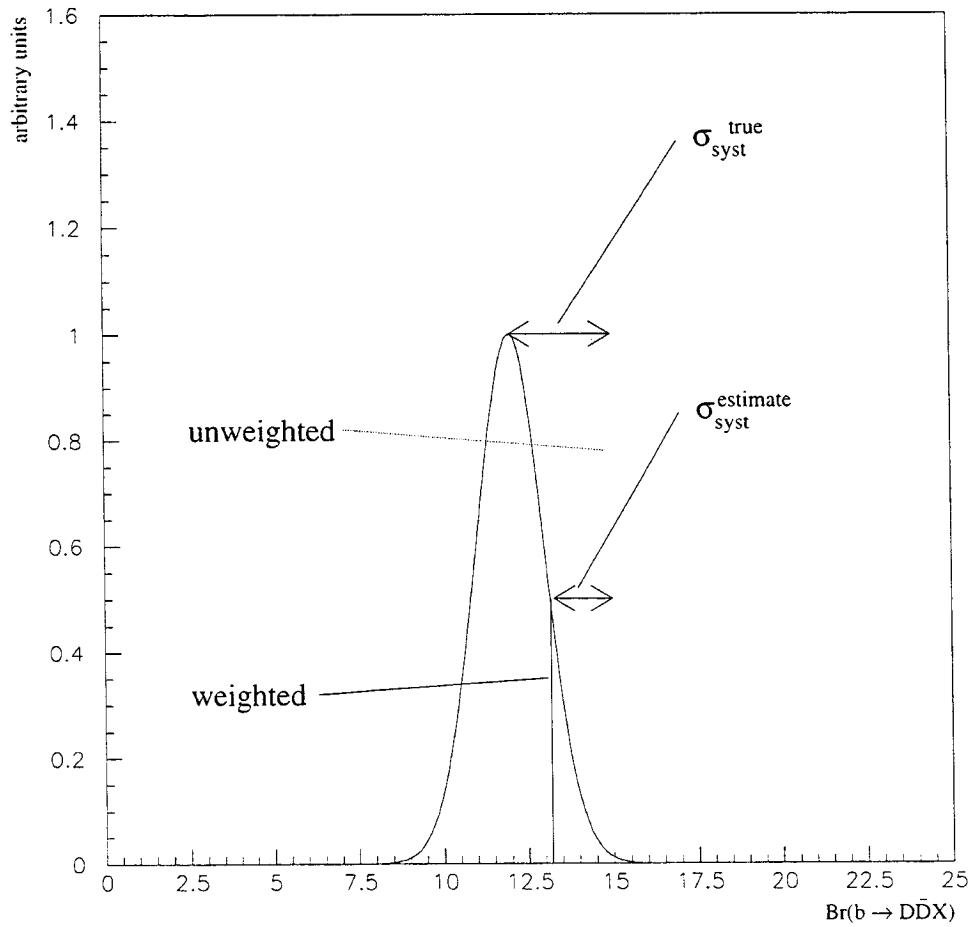

Figure 7.1: Visualization of statistical noise in systematic error estimates. The dashed vertical grey line represents the value of Br(b $\rightarrow$ D$\bar{\text{D}}$X) obtained from the fit with the unweighted MC. The black line vertical line represents the value of Br(b $\rightarrow$ D$\bar{\text{D}}$X) after weighting the MC. The gaussian represents the noise inherent in the weighting procedure.

gaussian is very narrow, but if there is significant statistical noise, the gaussian can be significantly wider. The method used here to determine the systematic uncertainty randomly samples one value from this gaussian.

In some weighting procedures, little statistical noise is introduced, so there is

no cause for concern. In general, weighting procedures that use weights close to 1.0 ($0.8 <$ weight < 1.2) yield reliable (*i.e.* relatively precise) results. In cases where the weights are larger (*e.g.* poorly measured inclusive branching ratios like $< n_{\pi^0} >_{D^0}$), the estimates of the associated systematic uncertainties are less reliable.

Unfortunately, some of the estimates of systematic uncertainties in this analysis are larger than estimated in MC studies (*e.g.* the uncertainty due to $< n_{\pi^0} >_{D^0}$). With infinite MC statistics, the potential problem of noise in the estimates of the systematic uncertainties would be solved. However, due to the computationally intensive nature of heavy flavour hadronic simulation, the MC statistics are limited. More precise measurements of some of the inclusive properties of b and D hadron decays would also help to reduce some of the systematic uncertainties in this analysis.

7.3 Detector modelling

7.3.1 d_0 modelling

One of the most important sources of systematic uncertainty in this analysis is modelling of the track impact parameter resolution. As already mentioned in section 5.2, the resolution functions for S are determined by fitting an analytical expression to selected backward tracks. The same set of resolution functions is applied to both data and MC to generate the $-\ln(P_j)$ distributions. Using the same set of resolution functions assumes that the impact parameter resolution is the same in the data and the MC. The MC has been tuned to make the d_0 distributions of backwards SI-$r\phi$=SI-z=2 tracks in the MC as similar as possible to the same distributions in data. The tuning was performed by scaling the difference between the measured d_0 and the true d_0 in MC by a constant. The methods used to tune the d_0 resolution

are described in section 5.3. As described in that section, the uncertainty in the d_0 resolution for the tracks used in this analysis is $\pm 1.5\%$.

The uncertainty due to mis-modelling d_0 in the MC is determined by re-processing the MC with the d_0 scale factors varied by ± 0.015, then re-doing the $-\ln(P_j)$ fits. The differences between the $Br(b \rightarrow D\bar{D}X)$ central value and $Br(b \rightarrow D\bar{D}X)$ values with different d_0 scale factors represent the systematic uncertainty. In case there are any correlations between the best d_0 scale factors for the different momentum bins, the scale factors for all momentum bins were varied at the same time, in the same direction, when the MC was re-processed. This uncertainty is assumed to be uncorrelated from year-to-year.

7.3.2 σ_{d_0} modelling

In addition to the d_0 modelling uncertainty, another source of uncertainty for $Br(b \rightarrow D\bar{D}X)$ that is related to the impact parameter of tracks is the mis-modelling of the impact parameter uncertainty, σ_{d_0}. Section 5.3 describes the tuning of σ_{d_0} and the uncertainty in the best scale values for σ_{d_0}. The uncertainty due to mis-modelling σ_{d_0} is determined by re-doing the analysis with the σ_{d_0} scale factors varied by $\pm 0.5\%$.

7.3.3 Track selection efficiency

It is important that the track selection efficiency, ϵ_{track}, is the same in the data and the Monte Carlo. Different track selection efficiencies may result in systematic differences between the MC and the data joint probability distributions. The sensitivity to ϵ_{track} mis-modelling is reduced by binning the $-\ln(P_j)$ distributions by track multiplicity. Some sensitivity does remain though.

The most significant cut for ϵ_{track} is the cut on the number of SI hits associated with a track. As previously mentioned, this analysis uses only tracks with two SI-$r\phi$ hits and two Si-z hits. The fraction of this class of tracks in the data is different from the fraction in the MC. Fortunately, it is relatively straightforward to correct ϵ_{track} differences between the data and the MC because the fraction of tracks in the MC that have two SI-$r\phi$ and two Si-z hits is larger than the fraction in the data (see table 7.3).

year	MC (%)	Data (%)	Δ (%)
1993	44.31±0.02	43.62±0.10	-0.69±0.10
1994	47.59±0.02	46.52±0.06	-1.07±0.06
1995	56.21±0.06	54.64±0.12	-1.57±0.13

Table 7.3: Fractions of tracks passing selection cuts (excluding silicon vertex detector hit requirement) that have two SI-$r\phi$ and two Si-z hits.

Tracks with two SI-$r\phi$ and two SI-z hits can be randomly dropped from the calculation of $-\ln(P_j)$ in the MC so that the track selection efficiencies are the same in the data and the MC. MC studies show that randomly dropping tracks introduces a large amount of statistical "noise" into the MC PDFs. The value of Br(b $\rightarrow$ D$\bar{\text{D}}$X) that is measured varies significantly depending on which tracks are randomly dropped. As a result, the process of dropping tracks and determining Br(b $\rightarrow$ D$\bar{\text{D}}$X) is repeated 20 times with different random number seeds in order to obtain a better estimate of the corrected Br(b $\rightarrow$ D$\bar{\text{D}}$X) and its associated uncertainty. The corrected Br(b $\rightarrow$ D$\bar{\text{D}}$X) is the mean of the distribution of Br(b $\rightarrow$ D$\bar{\text{D}}$X) values obtained after MC track selection efficiencies are corrected. The uncertainty of the correction is the uncertainty of the mean of the distribution. This uncertainty can be made arbitrarily small with more repetitions of the process; however, the

magnitude of the uncertainty after 20 trials is already negligibly small (0.3%) compared to the total uncertainty of Br(b $\rightarrow$ D$\bar{\text{D}}$X). Another small uncertainty in the correction that is due to finite MC and data statistics (that limit knowledge of the exact track selection efficiences) is negligibly small.

7.3.4 Combination of detector systematic uncertainties

For each year of data taking, the systematic uncertainties due to detector modelling are combined in quadrature with the statistical uncertainties when the weighted mean for Br(b $\rightarrow$ D$\bar{\text{D}}$X) is calculated. In order to separate the total uncorrelated uncertainty, σ_{uncorr}, into the contributions from the statistical and detector systematic uncertainties, the total statistical uncertainty, σ_{stat}, is given by

$$\sigma_{stat} = \left(\sum_i \frac{1}{\sigma^2_{stat_i}} \right)^{-1/2}, \tag{7.1}$$

where σ_{stat_i} are the statistical uncertainties for each year of data taking, and the total uncertainty due to detector modelling, σ_{det}, is given by

$$\sigma_{det} = \sqrt{\sigma^2_{uncorr} - \sigma^2_{stat}}. \tag{7.2}$$

7.4 Particle physics modelling

7.4.1 b quark fragmentation

One of the most interesting potential sources of uncertainty in the analysis is due to uncertainty of the energy spectrum of the weakly decaying b hadrons produced in Z^0 decays. This energy spectrum is dependent on the modelling of the b quark

energy spectrum after the parton shower/fragmentation (see section 4.2.1). The shape of the energy spectrum (and hence the mean energy carried by b hadrons, $< x_{\mathrm{E}} >$) affects the $-\ln(P_j)$ distributions. Several experiments have measured $< x_{\mathrm{E}} >$ using various methods [77, 78, 95]. The combined result for $< x_{\mathrm{E}} >$ is 0.7151 ± 0.0025 [76]. The Bowler fragmentation model [75] is currently the model that fits the data the best; for this reason, the central value for $\mathrm{Br}(\mathrm{b} \rightarrow \mathrm{D\bar{D}X})$ is obtained with this model. To assess the uncertainty in $\mathrm{Br}(\mathrm{b} \rightarrow \mathrm{D\bar{D}X})$ due to uncertainty from b fragmentation, jets in the simulation were weighted so that $< x_{\mathrm{E}} >$ was varied by its one standard deviation uncertainty assuming the Bowler, Lund [96], and Kartvelishvili [97] fragmentation models. Unlike many previous LEP heavy flavour analyses, the Peterson [74] and Collins-Spiller [98] fragmentation models are not considered as they are strongly disfavoured in the most recent b fragmentation results. The largest positive and negative differences between the central value of $\mathrm{Br}(\mathrm{b} \rightarrow \mathrm{D\bar{D}X})$ and the branching ratios obtained using $< x_{\mathrm{E}} > \pm\sigma_{<x_{\mathrm{E}}>}$ with the different fragmentation models were significant ($\pm 3.0\%$ for 1994); however, the mean charged particle multiplicity from fragmentation, $< N_{ch} >_{frag}$, changes when $< x_E >$ is changed by the weighting procedure ($< N_{ch} >_{frag}$ and $< x_E >$ are anti-correlated). As a result, the change in $\mathrm{Br}(\mathrm{b} \rightarrow \mathrm{D\bar{D}X})$ is due to both $< x_E >$ and $< N_{ch} >_{frag}$. The contribution of each is untangled by comparing the effect of changing $< N_{ch} >_{frag}$ in isolation. The following section describes how this is done. After this is done, the systematic uncertainty due to $< x_E >$ is consistent with $\pm 0.0\%$.

7.4.2 Multiplicity of charged particles from fragmentation

The mean multiplicity of charged particles that are produced during fragmentation in $Z^0 \rightarrow b\bar{b}$ events, $< N_{ch} >_{frag}$, affects the $-\ln(P_j)$ distributions. The more fragmentation charged particles that are present, the smaller $-\ln(P_j)$ tends to be. As mentioned in the previous section, $< N_{ch} >_{frag}$ is anti-correlated to $< x_E >$ because, as the b hadron energy increases, the amount of energy available to produce fragmentation tracks is reduced. When $< x_E >$ is changed by weighting, the fitted value for Br(b $\rightarrow$ D$\bar{\text{D}}$X) changes because of changes in $< x_E >$ and $< N_{ch} >_{frag}$. By determining the uncertainty due to $< N_{ch} >_{frag}$ alone, the contribution from $< x_E >$ to changes in Br(b $\rightarrow$ D$\bar{\text{D}}$X) can be determined. When $< x_E >$ changes, the change in $< N_{ch} >_{frag}$ changes Br(b $\rightarrow$ D$\bar{\text{D}}$X) in the same direction (positive or negative).

In order to determine the systematic uncertainty due to $< N_{ch} >_{frag}$ independently of $< x_E >$, $< N_{ch} >_{frag}$ is varied by randomly dropping fragmentation tracks. The mean multiplicity of charged particles from fragmentation in $Z^0 \rightarrow b\bar{b}$ events was determined by comparing experimental values of the average charged particle multiplicity in $Z^0 \rightarrow b\bar{b}$ decays, $< n_{ch} >_{b\bar{b}}$ [99,100], and the average charged particle multiplicity of b hadron decays, $< n_{ch} >_b$ (including the charged decay products of K_s and Λ) [23]. Combining these measurements gives $< N_{ch} >_{frag} = 12.46 \pm 0.32$ so the relative uncertainty for $< N_{ch} >_{frag}$ is $\pm 2.5\%$. To determine the effect of this uncertainty on Br(b $\rightarrow$ D$\bar{\text{D}}$X), 2.5% of fragmentation tracks were randomly dropped from the calculation of $-\ln(P_j)$ for MC jets. The difference between Br(b $\rightarrow$ D$\bar{\text{D}}$X) before and after dropping fragmentation tracks represented the systematic uncertainty. The process of randomly dropping tracks was repeated 20 times to obtain a more precise estimate of the systematic uncertainty by comparing the mean of the

$Br(b \rightarrow D\bar{D}X)$ values after dropping fragmentation tracks to $Br(b \rightarrow D\bar{D}X)$ before. The estimated systematic uncertainty due to $< N_{ch} >_{frag}$ is $\pm 5.7\%$ for 1994.

The effect on $Br(b \rightarrow D\bar{D}X)$ of varying $< N_{ch} >_{frag}$ by $\pm 2.5\%$ ($\Delta Br(b \rightarrow D\bar{D}X) = 5.7\%$ for 1994) was compared to the change in $Br(b \rightarrow D\bar{D}X)$ when $< x_E >$ was varied by its uncertainty ($\Delta Br(b \rightarrow D\bar{D}X) = 3.0\%$ for 1994). When $< x_E >$ was varied by its uncertainty, $< N_{ch} >_{frag}$ changed by $\pm 1.6\%$. From this, the uncertainty in $Br(b \rightarrow D\bar{D}X)$ that is actually due to $< x_E >$ is estimated to be $[3.0 - (\frac{1.6}{2.5} \times 5.7)]\% = -0.6\%$ for 1994. For this reason, $\Delta Br(b \rightarrow D\bar{D}X)$ due to changing $< x_E >$ can be attributed entirely to the associated change in $< N_{ch} >_{frag}$.

A study of the change in the d_0 of tracks from b and D hadron decays as a function of $< x_E >$ shows that d_0 changes very little so $-\ln(P_j)$ (and hence $Br(b \rightarrow D\bar{D}X)$) should change very little as well. The impact parameters of tracks from b and D decays do not change significantly when $< x_E >$ is changed because the increase(decrease) in the decay lengths of the weakly decaying hadrons is offset to first order by the decrease(increase) of the angles between the tracks and the jet axis.

7.4.3 Momentum spectrum of D hadrons in b hadron decays

The separation between the decay points of D hadrons and their parent b hadrons is affected by the momentum spectrum of the D hadrons in the rest frame of the b, $< x_{b \rightarrow D} >$. The D momentum in the b rest frame is small compared to the momentum of the b in the lab frame but it is still an important consideration for this analysis. CLEO has made precise measurements of the momentum spectra of $D^{(*)}$ hadrons in B meson decays [101]. Those results are applied to the admixture of b hadrons produced in Z^0 decays. Although the older $< x_{b \rightarrow D} >$ data [102] were well parameterized by a Peterson fragmentation function, the newer, more

precise data are not well described by the same function. The newer data are better parameterized by a gaussian. Figure 7.2 shows the most recent CLEO $< x_{b\to D} >$ data fitted by both a gaussian function and a Peterson fragmentation function.

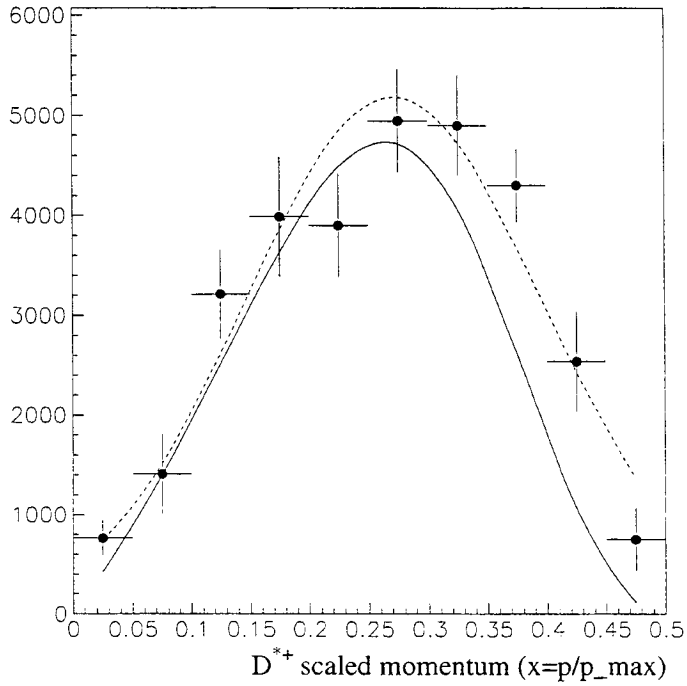

Figure 7.2: The most recent CLEO $< x_{b\to D} >$ data fitted by both a gaussian (dashed line) and a Peterson fragmentation function (solid line). The χ^2/d.o.f. for the fit with the gaussian is 12.2/7, while the χ^2/d.o.f. for the fit with the Peterson fragmentation function 43.9/8. Clearly, the data are better parameterized by a gaussian function.

The uncertainty in Br(b $\to$ D$\bar{\text{D}}$X) due to the uncertainty of $< x_{b\to D} >$ is determined by repeating the analysis many times with different MC $< x_{b\to D} >$ spectra that are compatible with the CLEO data. The different spectra are generated by a weighting procedure similar to the one described in section 7.1. The different $x_{b\to D}$ spectra are gaussians whose parameters are determined by randomly varying the gaussian parameters that best describe the CLEO $< x_{b\to D} >$ data by their uncer-

tainties. The correlation between the best fit parameters is taken into account when the parameters are randomly varied. The width of the distribution of $Br(b \to D\bar{D}X)$ values obtained with the different D momentum spectra determines the systematic uncertainty due to this source.

7.4.4 Charm and beauty hadron lifetimes

The shapes of the joint probability distributions of jets are largely determined by the decay lengths of the hadrons within them. This is the reason why the joint probability variable is used to separate double charm from single charm b decays. Consequently, it is important that the hadron lifetimes assumed in the Monte Carlo are correct. To assess the systematic uncertainty due to uncertainties in the b and D lifetimes, the lifetimes of the b and D hadrons are independently varied by their experimental uncertainties quoted in [23]. As the lifetimes of the D hadrons are known to better precision than the lifetimes of the b hadrons, the τ_{D_i} contributions to the systematic uncertainty of $Br(b \to D\bar{D}X)$ are smaller than the contributions from τ_{b_i}.

7.4.5 Fractions of b hadron species

Varying the fractions of the different b hadrons produced in $Z^0 \to b\bar{b}$ decays changes the joint probability distributions predicted by the Monte Carlo because of the different b hadron lifetimes. The fractions of different b hadrons have been measured by various LEP experiments and these results have been combined by the LEP Heavy Flavour Working Group [103]. The measurements of the different fractions are correlated. These correlations are accounted for in the calculation of the $Br(b \to D\bar{D}X)$ systematic uncertainties. In this analysis, the fractions f_{B^0} and f_{B^+} are assumed to

be equal and $f_{B^0} + f_{B^+} + f_{B_s} + f_{\Lambda_b} = 1$; these assumption are made also by the LEP Heavy Flavour Working Group. Even if the first assumption is not valid, it will not significantly affect this analysis since the lifetimes of the B^0 and B^+ mesons are very similar.

7.4.6 Gluon splitting to $b\bar{b}$ or $c\bar{c}$ pairs

In a small fraction of Z^0 decays, a hard gluon is radiated which fragments to a $b\bar{b}$ or a $c\bar{c}$ pair. The presence of these decays in selected jets affects the joint probability distributions because of the long lifetimes of the hadrons containing b or c quarks. Gluon splitting to $b\bar{b}$ or $c\bar{c}$ in light quark events can also change the efficiency to mis-tag light quark jets as b-jets. The rate of $g \to b\bar{b}$ and $g \to c\bar{c}$ at $\sqrt{s} = m_{Z^0}$ has been measured at LEP [103] and SLC [104]. For this analysis, the $g \to b\bar{b}$ and $g \to c\bar{c}$ rates are varied in the Monte Carlo by changing the weights of events. The variation in Br(b $\to$ D$\bar{\text{D}}$X) due to changing the $g \to b\bar{b}$ and $g \to c\bar{c}$ rates by their experimental uncertainties is taken as the systematic uncertainty. The thrust > 0.85 cut greatly reduces this background, so the resulting systematic uncertainty for Br(b $\to$ D$\bar{\text{D}}$X) is very small.

7.4.7 Charged particle multiplicity of D decays

The mean numbers of charged particles produced when different D hadrons decay were varied to determine their contributions to the systematic uncertainty in this analysis. The Mark III collaboration has published values for the mean number of charged particles produced per decay, $< n_{ch} >_D$, for D^+, D^0 and D_s^+ [105]. To estimate the magnitude of this systematic uncertainty, the central value of $< n_{ch} >_D$ for each D meson species was varied in the MC by the uncertainty quoted by MARK III

by weighting the MC. The mean charged particle multiplicity of charm baryon decays was varied by ± 0.5 about the JETSET prediction. The weighting was performed using a method similar to one used in previous OPAL heavy flavour analyses (e.g. R_b analysis [106]). In this method, weights are calculated for D decays with different n_{ch} by assuming that the D charged particle multiplicity distributions approximate Poisson distributions[1]. The weight is calculated using

$$w_D(n_{ch}) = \frac{P(n', < n' >_{new})}{P(n', < n' >_{old})} \tag{7.3}$$

where $P(n', < n' >_{new})$ is the probability for a Poisson distribution with mean $< n' >_{new}$ to have a value n'. The subscript "*old*" refers to the unweighted MC. Due to the fact that the n_{ch} distributions do not actually follow Poisson distributions, $< n' >_{new}$ is not simply equal to $< n' >_{old} \pm \sigma_{<n'>_{old}}$. The value for $< n' >_{new}$ that changes $< n_{ch} >_{\mathrm{D}}$ by the correct amount was determined by an iterative process. The weighting of the MC is done in a way that maintains the relative fractions of D_i in the MC; the uncertainty due to changing the D_i fractions is considered separately (see section 7.4.11). Care was also taken when weighting the MC to avoid changing BR(D$\rightarrow \bar{\mathrm{K}}^0$X) in the MC. This was done by calculating weights for jets with and without D$\rightarrow \bar{\mathrm{K}}^0$X decays separately.

7.4.8 Neutral pion multiplicity of D decays

Mark III has measured the neutral pion multiplicity of D^+, D^0 and D_s^+ decays [105]. Changing $< n_{\pi^0} >_{\mathrm{D}}$ without changing $< n_{ch} >_{\mathrm{D}}$ or Br(D$\rightarrow \bar{\mathrm{K}}^0$X) in the MC effectively changes the transverse momentum spectrum of tracks from D decays. This

[1] For neutral D hadrons a Poisson distribution is assumed for $\frac{n_{ch}}{2}$. For charged D hadrons a Poisson distribution is assumed for $\frac{n_{ch}-1}{2}$.

affects the d_0 of the tracks and hence will affect $-\ln(P_j)$. The effect on Br(b $\rightarrow$ D$\bar{\text{D}}$X) from changing $< n_{\pi^0} >_{\text{D}}$ for each of D^+, D^0 and D_s^+ was determined by weighting jets depending on the number of π^0s produced in D decays. The weighting was done in such a way as to vary $< n_{\pi^0_{D_i}} >$ by the one standard deviation uncertainty quoted by Mark III, without changing $< n_{ch} >_{\text{D}}$ or Br(D$\rightarrow \bar{\text{K}}^0$X).

7.4.9 Neutral kaon production in D decays

For D mesons, Br(D$\rightarrow \bar{\text{K}}^0$X) has been measured by MARK III [105]. The production of Λ in Λ_c^+ decays has been measured by several experiments; the average branching ratio is calculated in reference [23]. The uncertainty of Br(D$\rightarrow \bar{\text{K}}^0$X) results in a systematic uncertainty for this analysis as the multiplicity of charged particles originating at the D vertex changes if Br(D$\rightarrow \bar{\text{K}}^0$X) changes. This is because the charged particle multiplicity in D decays measured by MARK III includes charged particles from K_S^0 decays. Changing Br(D$\rightarrow \bar{\text{K}}^0$X) while keeping $< n_{ch} >_{\text{D}}$ constant changes the number of charged particles that actually originate at the point of the D decay, $n_{D_{vtx}}$. With $< n_{ch} >_{\text{D}}$ held constant, Br(D$\rightarrow \bar{\text{K}}^0$X) and $n_{D_{vtx}}$ are anti-correlated. Charged particles from K_S^0 decays tend not to pass the track selection cuts as they usually originate far from the interaction point, so do not produce hits in the silicon vertex detector. Changing the mean value for $n_{D_{vtx}}$ changes the $-\ln(P_j)$ distributions.

7.4.10 Charged particle multiplicity of b decays

The average number of charged particles produced per b hadron decay, $< n_{ch} >_{\text{b}}$, is an important systematic uncertainty to consider as the number of selected tracks from b or D decays in a jet directly influences $-\ln(P_j)$ for the jet. The dependence

of $Br(b \rightarrow D\bar{D}X)$ on $< n_{ch} >_b$ is reduced by binning the $-\ln(P_j)$ distributions by track multiplicity, but there still exists a systematic uncertainty due to $< n_{ch} >_b$. The systematic uncertainty of $Br(b \rightarrow D\bar{D}X)$ due to the uncertainty of $< n_{ch} >_b$ is determined by a method identical to the method used for $< n_{ch} >_D$. As described in section 7.4.7, the MC is weighted assuming Poisson distributions for the charged particle multiplicities of each of the different b hadrons.

7.4.11 Fractions of D hadrons in single and double charm b decays

Two of the most important systematic uncertainties to consider in this analysis are the fractions of different D hadrons in single charm, $f_{D_i}(1c)$, and double charm, $f_{D_i}(2c)$, b decays. These fractions are equal to the total number of a specific D hadron produced in single or double charm b decays divided by the total number of D hadrons produced in single or double charm b decays. The different D hadron species have quite different lifetimes: the ratio of $\tau_{D^+} : \tau_{D_s^+} : \tau_{D^0} : \tau_{\Lambda_c^+}$ is approximately 2.5 : 1.2 : 1 : 0.5. The joint probability variable depends strongly on the lifetimes of hadrons decaying in the jet, so altering the fractions of the different species can produce significant effects. As the D^+ and Λ_c^+ possess the longest and shortest D lifetimes respectively, they will be the two D hadrons considered in this section. The production of different D hadrons in b decays has been measured by several LEP experiments [107], [108], [109]. These measurements have also been used to calculate n_c. The combination of these results [23] can be used to constrain $f_{D_i}(1c)$ and $f_{D_i}(2c)$ ($D_i = D^+$ or Λ_c^+). The production rate[2] of a specific D hadron, D_i, per

[2]It is important to note that despite using the notation $Br(b \rightarrow D_iX)$, the production rates are not the same as the branching ratios. This somewhat confusing notation has been adopted by the Particle Data Group so this document will stay consistent with the PDG. The production rates take into consideration the possibility that two D hadrons of the same type (after one is charge con-

b decay can be expressed in terms of $f_{D_i}(1c)$, $f_{D_i}(2c)$, and the single and double charm branching ratios as follows:

$$\mathrm{Br}(b \rightarrow D_i X) = \mathrm{Br}_{1c} f_{D_i}(1c) + 2\mathrm{Br}_{2c} f_{D_i}(2c). \tag{7.4}$$

This gives one equation with $f_{D_i}(1c)$ and $f_{D_i}(2c)$ as unknowns (if one assumes a wide range of possible values for Br_{1c} and Br_{2c}). *A priori* one does not know the relationship between $f_{D_i}(1c)$ and $f_{D_i}(2c)$. It is possible though, to assume a range of possible values for $f_{D_i}(1c)$ - $f_{D_i}(2c) = \Delta_i$ and then determine the uncertainty of $f_{D_i}(1c)$ and $f_{D_i}(2c)$ introduced by the uncertainty of Δ_i. In the case of a $b \rightarrow c\bar{c}s$ decay, it is expected that the $\bar{c}$ quark produced in the virtual W decay will usually hadronize with its associated s quark to produce a $D_s^{(*)(*)-}$. A conservative range of values for the Δ_i is from 0 to $f_{D_i}(2c)$. In the case where $\Delta_i = 0$, one assumes that the $\bar{c}$ quark is just as likely to hadronize to a particular D_i as the sole c quark in single charm b decays. This is an extreme case that is not likely to occur as the $\bar{c}$ will tend to produce more $D_s^{(*)(*)-}$. If one assumes that the $\bar{c}$ quark hadronizes completely independently of the c quark and always produces a $D_s^{(*)(*)+}$ then $\frac{1}{2} f_{D_i}(1c) = f_{D_i}(2c)$ or $\Delta_i = f_{D_i}(2c)$. This results in a range of $0 < \Delta_i < f_{D_i}(1c)/2$ that should cover the range of reasonable Δ_i values. One can then substitute $f_{D_i}(1c) - \Delta_i$ for $f_{D_i}(2c)$ in equation 7.4 to get a range of possible $f_{D_i}(1c)$ values. Or, one can substitute $f_{D_i}(2c) + \Delta_i$ for $f_{D_i}(1c)$ in equation 7.4 to get a range of possible $f_{D_i}(2c)$ values.

To determine the full range of possible values of $f_{D_i}(1c)$ and $f_{D_i}(2c)$ one must also consider the uncertainty of $\mathrm{Br}(b \rightarrow D_i X)$ and the possible ranges of Br_{1c} and Br_{2c} (conservatively set at $\pm$ 10% and anti-correlated). At first glance this seems somewhat circular as Br_{2c} is ultimately what is measured in this analysis. However,

jugated) can be produced in one b decay. The production rate can also be thought of as the average multiplicity of D_i in b decays (e.g. $\mathrm{Br}(b \rightarrow D^+ X) = (N_{D^+ \text{ in b decays}} + N_{D^- \text{ in b decays}})/N_{\text{b decays}}$).

fraction	central value (%)	error from σ_{Δ_i} (%)	error from $\sigma_{Br(b\to D_iX)}$ (%)	error from $\sigma_{Br_{1c}}$, $\sigma_{Br_{2c}}$ (%)	total error (%)
$f_{D^+}(1c)$	23.3	±1.7	±2.1	±1.0	±2.9
$f_{D^+}(2c)$	17.0	±4.5	±1.7	±1.0	±4.9
$f_{\Lambda_c^+}(1c)$	10.0	±0.7	±2.8	±0.4	±2.9
$f_{\Lambda_c^+}(2c)$	7.4	±2.0	±2.1	±0.4	±2.9

Table 7.4: Values and uncertainties for f_{D_i}. The uncertainty from $\sigma_{Br(b\to D_iX)}$ is significant for each of the f_{D_i}. The uncertainty resulting from σ_{Δ_i} is the dominant error for $f_{D^+}(2c)$.

the weak dependence of $f_{D_i}(1c)$ and $f_{D_i}(2c)$ on Br_{1c} and Br_{2c} makes this circularity negligible. The contributions of all these uncertainties to the uncertainties of the various f_{D_i} are shown in table 7.4.

Having determined the uncertainties of the different f_{D_i}, the effect of these uncertainties on the measured Br_{2c} is determined. This is done by weighting the MC and determining the shift of the measured Br_{2c} as a function of f_{D_i}.

7.4.12 Background fractions

The backgrounds in the measurement of Br(b $\to$ D$\bar{\text{D}}$X) are defined as jets with neither single nor double "open" charm b decays (b$\to$ charmonium is a double "hidden" charm decay). The single charm b decay fraction is not considered a background as it is determined in the fit. The backgrounds are divided into the following categories: gluon jets in $Z^0 \to b\bar{b}$ events (f_g), light quark background (f_{uds}), charm quark background (f_c), b $\to$ no charm decays, and b $\to$ charmonium decays. In this analysis, the fractions of backgrounds assumed to be present in the data are fixed. These fractions depend on the relative abundances of the backgrounds before cuts are made and on the selection efficiencies after cuts are made. The

relative abundance of these processes has been determined by previous experimental measurements. The selection efficiencies and their uncertainties are determined by Monte Carlo studies.

The fraction of light and c quark backgrounds present before b-tagging is very well known due to the precise measurements of R_b and R_c [23]. For this analysis, the uncertainty in $\mathrm{Br}(\mathrm{b} \to \mathrm{D}\bar{\mathrm{D}}\mathrm{X})$ due to the uncertainty of these fractions is negligible. The c and *uds* selection efficiencies in b-tagging are not as well known though. Previous OPAL Monte Carlo studies have estimated the uncertainty in the c and *uds* selection efficiencies with the LEP2 b-tagger to be $\pm 10\%$ [110]. The b-tagging efficiencies for c and *uds* jets are separately varied by $\pm 10\%$ to assess their contributions to the systematic uncertainty in $\mathrm{Br}(\mathrm{b} \to \mathrm{D}\bar{\mathrm{D}}\mathrm{X})$. The fraction of $\mathrm{b} \to$ charmonium decays has been measured by many experiments; combining these measurements gives $\mathrm{Br}(\mathrm{b} \to \text{charmonium}) = (2.4 \pm 0.3)\%$ [23]. This branching ratio is varied by its uncertainty to assess its contribution to the systematic uncertainty of $\mathrm{Br}(\mathrm{b} \to \mathrm{D}\bar{\mathrm{D}}\mathrm{X})$. Finally, the experimental value for $\mathrm{Br}(\mathrm{b} \to \text{no charm})$ is $0.7 \pm 2.1\%$ [23]. By weighting jets, this branching ratio is varied in the Monte Carlo and the fits are re-done to determine the systematic uncertainty of $\mathrm{Br}(\mathrm{b} \to \mathrm{D}\bar{\mathrm{D}}\mathrm{X})$ due to the uncertainty in $\mathrm{Br}(\mathrm{b} \to \text{no charm})$.

Chapter 8

Discussion

8.1 Comparison to previous measurements

Using an inclusive method very similar to the one used in this thesis, DELPHI obtained $\mathrm{Br}(\mathrm{b} \to \mathrm{D}\bar{\mathrm{D}}\mathrm{X}) = (13.6 \pm 3.0(stat.) \pm 3.0(syst.))\%$ [37]. SLD obtained $\mathrm{Br}(\mathrm{b} \to \mathrm{D}\bar{\mathrm{D}}\mathrm{X}) = (17.9 \pm 1.4(stat.) \pm 3.3(syst.))\%$ [61] using a significantly different inclusive method that reconstructed secondary vertices. As the analysis performed for this thesis followed a procedure very similar to the one used by DELPHI, but obtained a systematic uncertainty due to particle physics modelling that is far larger, $(^{+10.4}_{-9.0}\%)$, some remarks are in order.

The impact parameter resolution of the DELPHI detector is $21\mu\mathrm{m} \oplus 59/p(\sin\theta)^{\frac{3}{2}}$ μm, where p is in GeV/c [111]. The impact parameter resolution of the OPAL detector for tracks with transverse momentum, p_T, between 0.15 GeV/c and 20 GeV/c is approximately $23\mu\mathrm{m} + 87/p_T$ μm. This means that the d_0 resolution of the DELPHI detector is approximately 25% better than OPAL's for the tracks of interest. The similar d_0 resolution of the two detectors is reflected by the fact that the statistical uncertainties of this result ($\pm$3.2%) and the DELPHI result ($\pm$3.0%)

are quite similar; however, the magnitude of the systematic uncertainties are very different.

Several significant sources of systematic uncertainty that are investigated in this analysis were not assigned uncertainties in the DELPHI analysis. These sources of uncertainty include the

- neutral pion multiplicity in D hadron decays,
- multiplicity of charged particles from fragmentation in $Z^0 \rightarrow b\bar{b}$ decays,
- D hadron lifetimes,
- multiplicity of charged particles from D_s and Λ_c decays,
- inclusive branching ratios of D_s to neutral kaons and Λ_c to Λ, and
- fraction of Λ_c hadrons in double charm b hadron decays.

Many of these sources of systematic uncertainty were found to be significant in this analysis.

8.2 Uncertainty due to $< N_{ch} >_{frag}$

The source of the largest systematic uncertainty in this analysis is $< N_{ch} >_{frag}$. This was not expected because the discriminating variable, $-\ln(P_j)$, is more sensitive to the multiplicity of tracks from b and D hadron decays than to the multiplicity of tracks from the primary vertex. Furthermore, the $-\ln(P_j)$ distributions for different track multiplicities are treated separately.

It turns out, however, that the measurement of $Br(b \rightarrow D\bar{D}X)$ is quite sensitive to $< N_{ch} >_{frag}$. To demonstrate the effect, a small fraction of tracks can be dropped

from the calculation of the joint probabilities of jets. When this occurs, the track multiplicity of some jets decreases by one and moves those jets into a track multiplicity bin with a lower average $-\ln(P_j)$. The typical change in the mean value of $-\ln(P_j)$ from one track multiplicity bin to the next lowest track multiplicity bin is -0.5. If a track from a b or D hadron decay is dropped, the mean change in $-\ln(P_j)$ is -0.92. If a fragmentation track is dropped, the mean change in $-\ln(P_j)$ is +0.26. As a result, if a b or D track is dropped, the jet tends to have $-\ln(P_j)$ that is 0.42 lower than the average $-\ln(P_j)$ for its new track multiplicity bin. When a fragmentation track is dropped, the jet tends to have $-\ln(P_j)$ that is 0.76 greater than the average $-\ln(P_j)$ for its new bin. Consequently, a jet which has a fragmentation track dropped is more unlike the jets in its new bin than a jet which has had a b or D track dropped. This makes the measurement of $\mathrm{Br}(\mathrm{b} \rightarrow \mathrm{D}\bar{\mathrm{D}}\mathrm{X})$ more sensitive to systematic changes in $< N_{ch} >_{frag}$ than changes in $< n_{ch} >_b$. In conjunction with this, the relative uncertainty of $< n_{ch} >_b$ is about 1/2 of the relative uncertainty for $< N_{ch} >_{frag}$.

As a check, a MC study was performed to determine if the overall sensitivity to systematic effects is reduced if the $-\ln(P_j)$ distributions are not binned by track multiplicity (unbinned). The pseudo-data and MC samples used in this study were identical to those used in the MC studies that were performed to optimize the binned analysis. The total systematic uncertainty in the unbinned MC study was $^{+8.2}_{-8.4}\%$ while the total systematic uncertainty in the binned MC study was $^{+7.9}_{-8.1}\%$.

Chapter 9

Conclusions

9.1 $\mathrm{Br}(\mathrm{b} \to \mathrm{D}\bar{\mathrm{D}}\mathrm{X})$ Measurement

The branching ratio $\mathrm{Br}(\mathrm{b} \to \mathrm{D}\bar{\mathrm{D}}\mathrm{X})$ has been measured using an inclusive joint probability method with data collected by the OPAL detector at LEP. The result

$$\mathrm{Br}(\mathrm{b} \to \mathrm{D}\bar{\mathrm{D}}\mathrm{X}) = (10.0 \pm 3.2(stat.)^{+2.4}_{-2.9}(syst.\ det.)^{+10.4}_{-9.0}(syst.\ phys.))\%$$

is consistent with the average of the two previous inclusive measurements of $\mathrm{Br}(\mathrm{b} \to \mathrm{D}\bar{\mathrm{D}}\mathrm{X})$: $(16.1 \pm 2.7)\%$. These two measurements were made by the SLD [61] and DELPHI collaborations [37].

9.2 n_c Measurement

Using this measurement of $\mathrm{Br}(\mathrm{b} \to \mathrm{D}\bar{\mathrm{D}}\mathrm{X})$, the average number of charm quarks produced per beauty quark decay, n_c, is calculated to be $1.12^{+0.11}_{-0.10}$. This value is consistent with the world average value at the Z^0 of 1.166 ± 0.033 quoted by the

Particle Data Group [23] (this average does not include the SLD Br($b \to D\bar{D}X$) or n_c results mentioned previously as the SLD analysis has not been published yet). The main measurements contributing to this average are the inclusive measurement by DELPHI and several exclusive analyses that fully reconstruct weakly decaying D hadrons in b jets/hemispheres (OPAL [58], DELPHI [59], ALEPH [60]). In principle, inclusive measurements have an advantage that a larger sample of events can be used to determine n_c; the exclusive analyses reconstruct the various D hadrons in experimentally clean, but statistically limited decay modes (e.g. $Br(D^0 \to K^-\pi^+) = (3.80\pm0.09)\%$). The uncertainty of exclusive measurements is dominated by uncertainties in the branching ratios of the decay modes that are used to reconstruct the D hadrons. Inclusive analyses are not sensitive to specific exclusive branching ratios; however, they are quite sensitive to the modelling of the detector resolution and the modelling of the inclusive properties of b and D hadron decays, and b hadron production. This analysis' precision is currently limited by knowledge of some of these inclusive properties. When more precise measurements of these properties are made, the total uncertainty of this analysis will be reduced. The central value and its uncertainty may be updated in the future by referring to the information in tables 7.1 and 7.2 (see caption for table 7.1).

9.3 Comparison to theory

The measurements of n_c and Br($b \to D\bar{D}X$) obtained in this analysis are consistent with theoretical calculations [38]. As the uncertainties of this analysis' determinations of Br($b \to D\bar{D}X$) and n_c are large, it is not possible to come to any detailed conclusions about any of the assumptions that go into the theoretical calculations. Figure 9.1 shows that the predicted value for n_c is sensitive to the ratio of the charm

and beauty quark masses, m_c/m_b, but is quite insensitive to the renormalization scale, μ, for the calculation of n_c. If future n_c measurements are more precise, they might constrain m_c/m_b further. More precise measurements of $\mathrm{Br}(\mathrm{b} \to \ell\nu\mathrm{X})$ are required to constrain μ further.

9.4 Future prospects

After many years of effort, it is clear that it is very difficult to make precise inclusive measurements of $\mathrm{Br}(\mathrm{b} \to \mathrm{D}\bar{\mathrm{D}}\mathrm{X})$ and n_c. Currently, the DELPHI result is the only published result. There is potential for future measurements/improvements of n_c though. Now that the BELLE and BABAR experiments have each collected data from over 100 million B meson decays, n_c analyses by these experiments can certainly reduce the statistical uncertainty of $\mathrm{Br}(\mathrm{B} \to \mathrm{D}\bar{\mathrm{D}}\mathrm{X})$ and n_c at the $\Upsilon(4\mathrm{S})$. The uncertainty of n_c and $\mathrm{Br}(\mathrm{b} \to \mathrm{D}\bar{\mathrm{D}}\mathrm{X})$ is currently dominated by systematic uncertainties though. The excellent tracking resolution and vertex reconstruction capabilities of those detectors should also lead to a reduction in the uncertainty due to detector resolution (currently the major source of systematic uncertainty in the DELPHI and SLD measurements).

Uncertainties of the inclusive properties of D hadron decays are still issues for an inclusive measurement like the one performed in this thesis; however, the proposed charm factory at CESR/CLEO could greatly reduce some of these uncertainties in the near future. Many inclusive b physics analyses besides n_c and $\mathrm{Br}(\mathrm{b} \to \mathrm{D}\bar{\mathrm{D}}\mathrm{X})$ are sensitive to uncertainties in the decay properties of D hadrons, so many areas of heavy flavour physics would benefit from a charm factory. As the dominant uncertainties in this analysis are from physics systematics, this analysis' total uncertainty will be reduced appreciably when more precise measurements of inclusive D decays

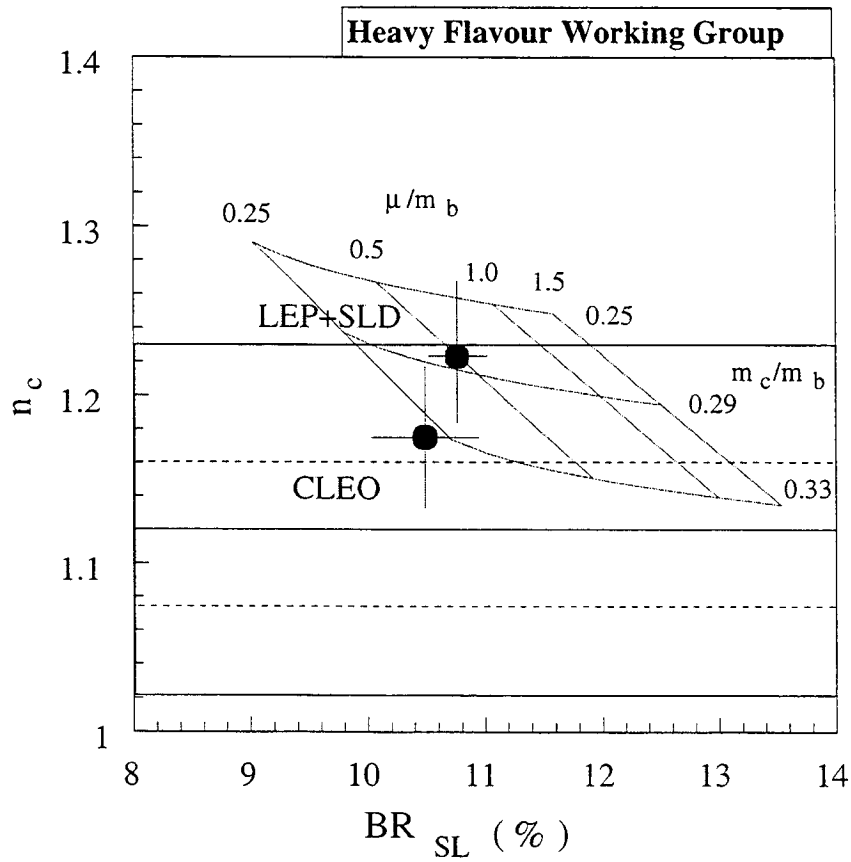

Figure 9.1: Comparison of n_c from this analysis and the average values for n_c and Br(b $\rightarrow \ell\nu$X), to theory. The n_c result from this analysis is not included in the n_c average shown here; this analysis' n_c value (grey band) is shown separately for comparison. The dashed line shows the combined statistical and detector systematic uncertainties for this measurement of n_c. This plot shows the anti-correlation between the predicted values for n_c and Br(b $\rightarrow \ell\nu$X). The calculated values for n_c and Br(b $\rightarrow \ell\nu$X) are from [38]. This plot also shows the n_c and Br(b $\rightarrow \ell\nu$X) results from CLEO data collected at the Υ(4S) resonance. The original version of this plot was taken from [103] but has been updated to include the most recent SLD measurement of n_c [61].

are made.

Appendix A

OPAL coordinate system and track parameters

In the cartesian version of the OPAL coordinate system, the x-axis points horizontally from the centre of the detector to the middle of the LEP ring. The y-axis points vertically upwards from the centre of the detector. The z-axis points in the direction of the electron beam as it passes through the detector. The origin of the coordinate system is located at the geometrical centre of the detector. In the OPAL spherical coordinate system, the polar angle, θ, is measured from the z-axis, and the azimuthal angle, ϕ, is measured in the $x-y$ plane from the x-axis to the y-axis. The OPAL cartesian coordinate system, θ and ϕ are shown in figure A.1.

Five parameters are used to specify the trajectory of a charged particle in the OPAL detector. Figure A.2 illustrates these track parameters. Three parameters are used to describe the track in the $x-y$ (or equivalently $r-\phi$[1]) plane: d_0, ϕ_0 and κ. The impact parameter, d_0, is the separation between the origin and the point on the track that is closest to the the origin in the $x-y$ plane (point of closest

[1]Here r is the perpendicular distance from the beam axis.

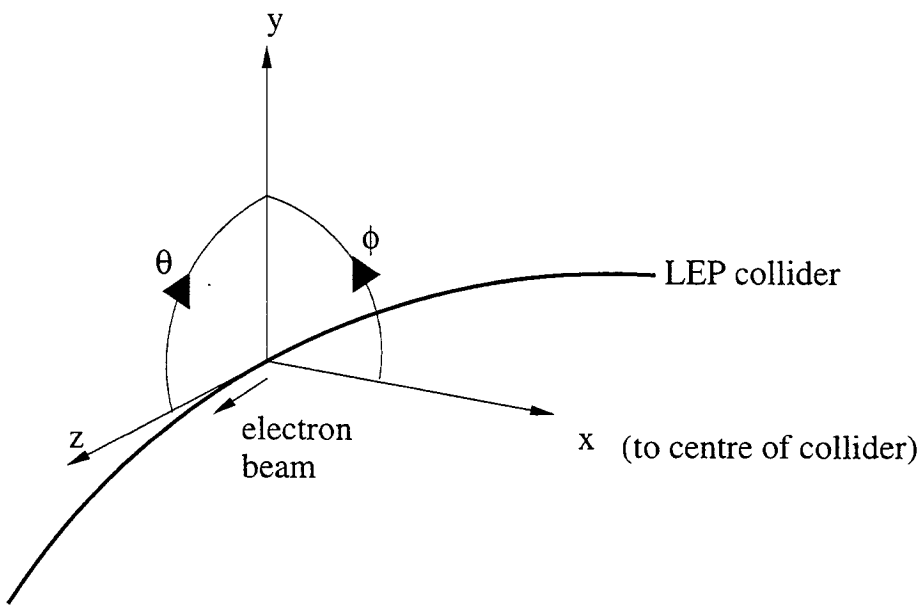

Figure A.1: The OPAL coordinate system. The $x-z$ plane is approximately in the plane of the LEP collider.

approach). The track's azimuthal angle, ϕ_0, is measured at the point of closest approach, between the x-axis and the $x-y$ projection of the momentum vector of the track. The track parameter κ is related to the track's radius of curvature, ρ, by $|\kappa| = 1/2\rho$. The sign of κ is determined by the change in ϕ as the track is followed from the centre of the detector outwards. The sign of κ is positive if ϕ increases; the sign is negative otherwise.

Two parameters are used to describe the track in the $s-z$ plane (where s follows the projection of the curved track in the $x-y$ plane): λ and z_0. The dip angle, λ, is related to the polar angle, θ, by $\lambda = \pi/2 - \theta$. The parameter z_0 is the z coordinate of the track at the point of closest approach in the $x-y$ plane.

It is important to note that the OPAL track parameter d_0, as it is described here, is measured with respect to the origin of the OPAL coordinate system. The track impact parameter that is used to calculate the joint probability variable that is used

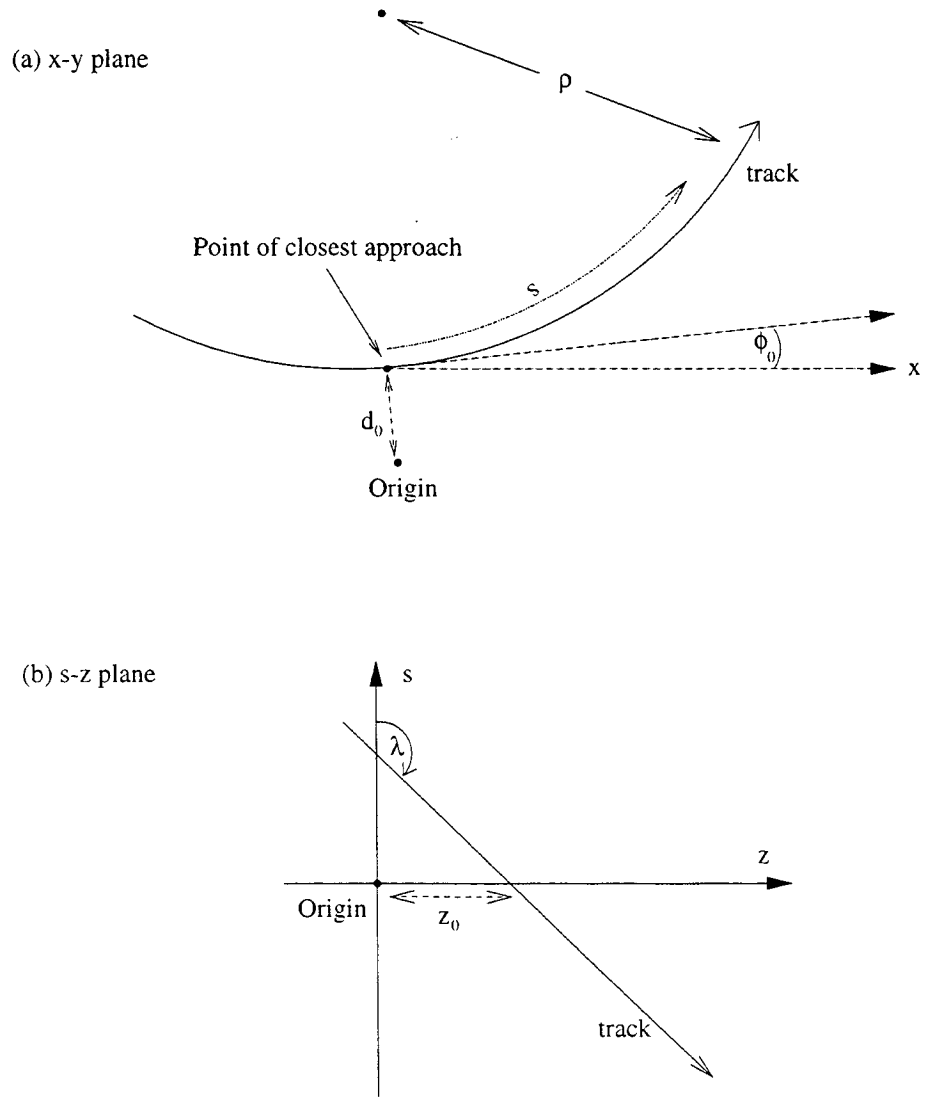

Figure A.2: Definition of track parameters in OPAL. Tracks are shown in (a) the $x-y$ plane and (b) the $s-z$ plane. The track parameters are described in the text.

in this analysis is measured with respect to the interaction point (as estimated by the primary vertex) in the $x - y$ plane. Unfortunately, the impact parameter with respect to the primary vertex is also referred to as d_0. Throughout the rest of the thesis, d_0 refers to the impact parameter with respect to the primary vertex.

Bibliography

[1] G. Zweig, An SU3 Model for Strong Interaction Symmetry and Its Breaking, CERN preprint 8182/TH 401, 1964.

[2] G. Zweig, An SU3 Model for Strong Interaction Symmetry and Its Breaking: II, CERN preprint 8419/TH 412, 1964.

[3] M. Gell-Mann, Phys. Lett. **8**, 214 (1964).

[4] G. Johnson, *Strange Beauty: Murray Gell-Mann and the Revolution in 20th Century Physics* (Random House, New York, 2000).

[5] E. D. Bloom *et al.*, Phys. Rev. Lett. **23**, 930 (1969).

[6] M. Breidenbach *et al.*, Phys. Rev. Lett. **23**, 935 (1969).

[7] J. E. Augustin *et al.*, Phys. Rev. Lett. **33**, 1406 (1974).

[8] J. J. Aubert *et al.*, Phys. Rev. Lett. **33**, 1404 (1974).

[9] S. W. Herb *et al.*, Phys. Rev. Lett. **39**, 252 (1977).

[10] CDF Collaboration, F. Abe *et al.*, Phys. Rev. Lett. **74**, 2626 (1995), hep-ex/9503002.

[11] D0 Collaboration, S. Abachi *et al.*, Phys. Rev. Lett. **74**, 2632 (1995), hep-ex/9503003.

[12] S. L. Glashow, Nucl. Phys. **22**, 579 (1961).

[13] A. Salam, Elementary Particle Theory: Relativistic Groups and Analyticity (8^{th} Nobel Symposium), 1968, edited by N. Svartholm, Amlqvist and Wiksell, Stockholm.

[14] S. Weinberg, Phys. Rev. Lett. **19**, 1264 (1967).

[15] D. J. Gross and F. Wilczek, Phys. Rev. **D8**, 3633 (1973).

[16] S. Weinberg, Phys. Rev. Lett. **31**, 494 (1973).

[17] CDF Collaboration, T. Affolder *et al.*, Phys. Rev. Lett. **84**, 835 (2000), hep-ex/9909027.

[18] L3 Collaboration, P. Achard *et al.*, Phys. Lett. **B517**, 75 (2001), hep-ex/0107015.

[19] The LEP Collaborations (ALEPH, DELPHI, L3, OPAL), Phys. Lett. **B276**, 247 (1992).

[20] DELPHI Collaboration, P. Abreu *et al.*, Phys. Lett. **B274**, 230 (1992).

[21] Super-Kamiokande Collaboration, Y. Fukuda *et al.*, Phys. Rev. Lett. **81**, 1562 (1998), hep-ex/9807003.

[22] SNO Collaboration, Q. R. Ahmad *et al.*, Phys. Rev. Lett. **87**, 071301 (2001), nucl-ex/0106015.

[23] Particle Data Group, K. Hagiwara *et al.*, Phys. Rev. **D66**, 010001 (2002).

[24] P. W. Higgs, Phys. Rev. Lett. **13**, 508 (1964).

[25] P. W. Higgs, Phys. Rev. **145**, 1156 (1966).

[26] G. S. Guralnik, C. R. Hagen, and T. W. B. Kibble, Phys. Rev. Lett. **13**, 585 (1964).

[27] F. Englert and R. Brout, Phys. Rev. Lett. **13**, 321 (1964).

[28] LEP Higgs Working Group for Higgs boson searches, (2001), hep-ex/0107029.

[29] N. Cabibbo, Phys. Rev. Lett. **10**, 531 (1963).

[30] M. Kobayashi and T. Maskawa, Prog. Theor. Phys. **49**, 652 (1973).

[31] LEP Electroweak Working Group, web site, 2002, available online at http://lepewwg.web.cern.ch/.

[32] TOPAZ, K. Miyabayashi *et al.*, Phys. Lett. **B347**, 171 (1995).

[33] BELLE Collaboration, K. Abe *et al.*, Phys. Rev. Lett. **87**, 091802 (2001), hep-ex/0107061.

[34] BABAR Collaboration, B. Aubert *et al.*, Phys. Rev. Lett. **87**, 091801 (2001), hep-ex/0107013.

[35] M. Neubert, Adv. Ser. Direct. High Energy Phys. **15**, 239 (1998), hep-ph/9702375.

[36] G. Barker, in *Proceedings of the 30th International Conference on High Energy Physics*, edited by C. Lim and T. Yamanaka, Singapore, 2001, World Scientific.

[37] DELPHI Collaboration, P. Abreu *et al.*, Phys. Lett. **B426**, 193 (1998).

[38] M. Neubert and C. T. Sachrajda, Nucl. Phys. **B483**, 339 (1997).

[39] CLEO Collaboration, S. Henderson *et al.*, Phys. Rev. **D45**, 2212 (1992).

[40] OPAL Collaboration, G. Abbiendi *et al.*, Eur. Phys. J. **C13**, 225 (2000).

[41] L3 Collaboration, M. Acciarri *et al.*, Eur. Phys. J. **C13**, 47 (2000).

[42] DELPHI Collaboration, P. Abreu *et al.*, Z. Phys. J. **C66**, 323 (1995).

[43] ALEPH Collaboration, A. Heister *et al.*, Eur. Phys. J. **C22**, 613 (2002).

[44] Particle Data Group, D. E. Groom *et al.*, Eur. Phys. J. **C15**, 642 (2000).

[45] I. Bigi *et al.*, Phys. Lett. **B323**, 408 (1994).

[46] G. Altarelli and S. Petrarca, Phys. Lett. **B261**, 303 (1991).

[47] A. L. Kagan and J. Rathsman, (1997), hep-ph/9701300.

[48] P. S. Drell, (1997), hep-ex/9711020.

[49] ALEPH Collaboration, R. Barate *et al.*, Phys. Lett. **B429**, 169 (1998).

[50] DELPHI Collaboration, M. Battaglia and P. Kluit, DELPHI 97-80 CONF 66, 1997.

[51] CLEO Collaboration, CLEO CONF 98-17, 1998.

[52] Belle, K. Abe *et al.*, Phys. Lett. **B511**, 151 (2001), hep-ex/0103042.

[53] E. Bagan, P. Ball, V. M. Braun, and P. Gosdzinsky, Nucl. Phys **B432**, 3 (1994).

[54] E. Bagan, P. Ball, B. Fiol, and P. Gosdzinsky, Phys. Lett. **B351**, 546 (1995).

[55] E. Bagan, P. Ball, V. M. Braun, and P. Gosdzinsky, Phys. Lett. **B342**, 362 (1995).

[56] E. Bagan, P. Ball, V. M. Braun, and P. Gosdzinsky, Phys. Lett. **B374**, 363 (1996).

[57] K. Honscheid, in *Proceedings of the International b20 Symposium*, Chicago, 1997.

[58] OPAL Collaboration, G. Alexander *et al.*, Z. Phys. **C72**, 1 (1996).

[59] DELPHI Collaboration, P. Abreu *et al.*, Eur. Phys. J. **C12**, 225 (2000).

[60] ALEPH Collaboration, D. Buskulic *et al.*, Phys. Lett. **B388**, 648 (1996).

[61] SLD Collaboration, A. S. Chou, (2002), hep-ex/0205050.

[62] T. Fowler, J. C. Freze, K. D. Grier, K. D. Metzmacher, and L. Sermeus, Presented at 1989 Particle Accelerator Conf., Chicago, IL, Mar 20-23, 1989.

[63] H. Burkhardt and R. Kleiss, Prepared for 4th European Particle Accelerator Conference (EPAC 94), London, England, 27 Jun - 1 Jul 1994.

[64] S. Myers, The LEP Collider from Design to Approval and Commissioning, Excerpts from The John Adams Memorial Lecture delivered at CERN. Available online at http://sl-div.web.cern.ch/sl-div/history/lep_doc.html, 1990.

[65] OPAL Collaboration, K. Ahmet *et al.*, Nucl. Instrum. Meth. **A305**, 275 (1991).

[66] P. Billoir, Nucl. Instr. Meth. **A225**, 352 (1984).

[67] V. Gibson, OPAL SI Primer, web site, 2002, available online at http://opalinfo.cern.ch/opal/manuals/si/pro/si.html.

[68] OPAL Collaboration, P. P. Allport *et al.*, Nucl. Instrum. Meth. **A324**, 34 (1993).

[69] OPAL Collaboration, P. P. Allport *et al.*, Nucl. Instrum. Meth. **A346**, 476 (1994).

[70] M. Hauschild, The OPAL Jet Chamber, web site, 2002, available online at http://opalinfo.cern.ch/opal/group/cj/plots.html.

[71] T. Sjostrand, Comput. Phys. Commun. **82**, 74 (1994).

[72] OPAL Collaboration, J. Allison *et al.*, Nucl. Instrum. Meth. **A317**, 47 (1992).

[73] R. Brun *et al.*, GEANT3 User's Guide, CERN Report DD/EE/84-1, 1984.

[74] C. Peterson, D. Schlatter, I. Schmitt, and P. M. Zerwas, Phys. Rev. **D27**, 105 (1983).

[75] M. G. Bowler, Zeit. Phys. **C11**, 169 (1981).

[76] K. Harder, Measurement of the b-quark fragmentation function and of the $B\bar{B}$ energy correlation in $Z^0 \to b\bar{b}$ decay, in *31st International Conference on High Energy Physics, Amsterdam*, 2002.

[77] SLD Collaboration, K. Abe *et al.*, Phys. Rev. **D65**, 092006 (2002), hep-ex/0202031.

[78] ALEPH Collaboration, A. Heister *et al.*, Phys. Lett. **B512**, 30 (2001), hep-ex/0106051.

[79] B. Andersson, G. Gustafson, G. Ingelman, and T. Sjostrand, Phys. Rept. **97**, 31 (1983).

[80] R. Hemingway, An OPAL tune of JETSET using Z^0 data, OPAL Technical Note TN279, 1995.

[81] C. Darling *et al.*, OPAL updates to JETSET 7.4 decay tables, OPAL Technical Note TN322, 1995.

[82] OPAL Collaboration, G. Alexander *et al.*, Z. Phys. **C69**, 543 (1996).

[83] D. Glenzinski, A. Hocker, and M. Oreglia, Optimization of the impact parameter joint probability b-tagger for OPAL using 3d silicon information, OPAL Technical Note TN522, 1997.

[84] N. Brown and W. J. Stirling, Phys. Lett. **B252**, 657 (1990).

[85] S. Bethke, Z. Kunszt, D. E. Soper, and W. J. Stirling, Nucl. Phys. **B370**, 310 (1992).

[86] S. Catani, Y. L. Dokshitzer, M. Olsson, G. Turnock, and B. R. Webber, Phys. Lett. **B269**, 432 (1991).

[87] N. Brown and W. J. Stirling, Z. Phys. **C53**, 629 (1992).

[88] S. Yamashita and I. Nakamura, A New B-tagging Tool for LEP 2, OPAL Technical Note TN576, 1998.

[89] S. Yamashita and I. Nakamura, LB160: Upgraded B-tagging for LEP 2, OPAL Technical Note TN578, 1998.

[90] R. Batley, R. Hawkings, M. Hildreth, and T. Junk, ODSIZL 2.11, DST-Level Tracking Adjustments and Refit with Silicon Hits, OPAL Technical Note TN520, 1997.

[91] F. James and M. Roos, Comput. Phys. Commun. **10**, 343 (1975).

[92] OPAL Collaboration, K. Ackerstaff *et al.*, Z. Phys. **C74**, 1 (1997).

[93] F. James and M. Roos, Phys. Rev. **D44**, 299 (1991).

[94] OPAL, G. Abbiendi *et al.*, Eur. Phys. J. **C8**, 217 (1999), hep-ex/9810002.

[95] OPAL Collaboration, G. Abbiendi *et al.*, *Inclusive analysis of the b quark fragmentation function in Z decays at LEP*, 2002, submitted to Eur. Phys. J. C. CERN-EP/2002-051.

[96] B. Andersson, G. Gustafson, and B. Soderberg, Z. Phys. **C20**, 317 (1983).

[97] V. G. Kartvelishvili, A. K. Likhoded, and V. A. Petrov, Phys. Lett. **B78**, 615 (1978).

[98] P. D. B. Collins and T. P. Spiller, J. Phys. **G11**, 1289 (1985).

[99] A. De Angelis, Talk given at 24th International Symposium on Multiparticle Dynamics, Salerno, Italy, 12-19 Sep 1994.

[100] OPAL Collaboration, R. Akers *et al.*, Phys. Lett. **B352**, 176 (1995).

[101] CLEO Collaboration, L. Gibbons *et al.*, Phys. Rev. **D56**, 3783 (1997), hep-ex/9703006.

[102] CLEO Collaboration, D. Bortoletto *et al.*, Phys. Rev. **D45**, 21 (1992).

[103] ALEPH, CDF, DELPHI, L3, OPAL, SLD Collaborations, Combined results on b-hadron production rates and decay properties, CERN-EP/2001-050, 2001.

[104] SLD Collaboration, K. Abe *et al.*, Phys. Lett. **B507**, 61 (2001), hep-ex/0102002.

[105] MARK-III Collaboration, D. Coffman *et al.*, Phys. Lett. **B263**, 135 (1991).

[106] R. Batley, Light quark systematics in R_b analysis, OPAL Technical Note TN453, 1997.

[107] OPAL Collaboration, G. Alexander *et al.*, Z. Phys. **C72**, 1 (1996).

[108] DELPHI Collaboration, P. Abreu *et al.*, Eur. Phys. J. **C12**, 225 (2000).

[109] ALEPH Collaboration, D. Buskulic *et al.*, Phys. Lett. **B388**, 648 (1996).

[110] OPAL Collaboration, G. Abbiendi *et al.*, Phys. Lett. **B520**, 1 (2001), hep-ex/0108031.

[111] G. Borisov and C. Mariotti, Nucl. Instrum. Meth. **A372**, 181 (1996).